In Situ Electrical Sensing of Microfiltration Events in Complex Media

Matthieu Sagot

RÉPUBLIQUE FRANÇAISE
Liberté Égalité Fraternité

Université de Toulouse

Doctorat de l'Université de Toulouse

préparé à Toulouse INP

Détection Électrique In-Situ des Événements de Microfiltration dans des Milieux Complexes

Thèse présentée et soutenue, le 19 mars 2024 par

Matthieu SAGOT

École doctorale
SDM - SCIENCES DE LA MATIERE - Toulouse

Spécialité
Physique

Unité de recherche
LAAS - Laboratoire d'Analyse et d'Architecture des Systèmes

Thèse dirigée par
Christophe VIEU et Hervé AUBERT

Composition du jury
Mme Nathalie RAVEU, Présidente, Toulouse INP
M. Stephan SYLVEST KELLER, Rapporteur, Technical University of Denmark
Mme Severine LE GAC, Rapporteure, University of Twente
M. Thomas LAURELL, Examinateur, Lund University
M. Angelo ACCARDO, Examinateur, Delft University of Technology
Mme Aline CERF, Examinatrice, SmartCatch
M. Christophe VIEU, Directeur de thèse, Institut National des Sciences Appliquées de Toulouse
M. Hervé AUBERT, Co-directeur de thèse, Toulouse INP

Membres invités
M. Zacchari BEN MERIEM, SmartCatch
M. Bastien VENZAC, LAAS CNRS
M. David BOURRIER, LAAS CNRS

Acknowledgement

We would like to acknowledge the strong implications of the technical services of the LAAS-CNRS.

Xavier Dollat designed and fabricated the device holder presented in chapter 2.

The fabrication processes were developed in strong collaboration with David Bourrier.

Aurélie Lecestre and Adrian Laborde provided useful insights along the silicon process development (see chapter 3) for respectively the RIE plasma etching and photolithography steps.

Bastien Venzac developed the Print Pause Print 3D printing process presented in chapter 3 and integrated the first prototype.

Fabrice Mathieu designed and fabricated the multiplexer presented in chapter 3

Finally, we would like to thank all the members of both the I2C (Characterization) and TEAM (Clean room) services for their day-to-day contributions to the project.

Abstract

Microfiltration is a well-documented scientific and technological domain that still requires research when targeting the specific and accurate filtration of rare elements inside a complex medium. Indeed, innovative solutions for sample filtering of complex media may hold the key to multiple health-related and environmental issues and applications. Blood is a good example of a complex medium: it contains a large quantity and variety of cells and proteins and exhibits a viscosity three to eight times greater than water and non-Newtonian behavior when flowing.

Clinical applications of blood filtration require processing large volume of blood either because of the scarcity of the targeted elements (in the case of circulating tumor cell capture, clinical relevance starts at 5 CTCs/mL of blood) or because the whole circulating blood needs to be expurgated from some adverse entities (such as cell aggregates or circulating microparticles in stroke and cardiovascular diseases). Finally, the biological nature of the targeted elements may introduce variability in the targeted element size and shape, therefore bringing fluidic challenges for their retrieval within such media. Blood filtration is a process which is central in hemodialysis, cardiovascular disease monitoring, and liquid biopsy applications based on the selective capture of Circulating Tumor Cells (CTCs), among other clinical contexts.

For such applications, micro and nanofabrication using methods and techniques used today in advanced semi-conductor industry, brings the ability to control with great accuracy the size of the filtering pores with respect to the size of the targeted elements that require filtration. This level of accuracy in the fabrication process opens the opportunity to retain only the targeted element driving the biological information in the case of a diagnosis application or driving the pathogenicity in the case of therapeutic applications without impairing the composition of the eluted blood.

However, because a large volume of blood is processed and due to the presence of millions of white blood cells (WBC) and billions of red blood cells (RBC) per milliliter of blood, such advanced microfabricated filters are subjected to clogging due to the unwanted accumulation of material unavoidably retained among time. This drawback appeals to the development of an in-situ method capable of sensing the cell density at the surface of these filters during use, to monitor their saturation in order to clean their surface or to proceed to their replacement by fresh ones.

In this context, we propose clean room microfabricated devices capable of fulfilling these requirements. The produced sensing devices combine a filtering membrane with an in situ cellular electrical detection method through interdigitated microelectrodes and impedance spectroscopy measurements. Despite using micron-scale filtering pores and microfabricated devices, we propose a specific design that enables blood filtration at a high flow rate (11.5 mL/min), which is much larger than usual microfluidic

devices. Finally, we demonstrate that stable electrical measurements can be performed in whole blood at high flow rates to monitor the saturation of the filter by retained cells.

Moreover, the fine analysis of the captured cells, usually entrusted to remote laboratories, could be transferred at the patient's bedside along the sample processing if an in-situ analysis and real-time phenotyping of the collected cells through their electrical signature could be demonstrated. This aspect will be addressed through the conception and fabrication of dedicated filtering devices, thus broadening the application field of electrical sensing on a filtering membrane within a microfluidic chip.

The research at the core of this PhD thesis has been implemented at LAAS-CNRS, an academic research laboratory of CNRS organization hosting a state-of-the-art clean room facility. The project was developed in close collaboration with a young company developing solutions for liquid biopsy applications: SmartCatch.

Resumé

La microfiltration constitue un domaine scientifique et technologique bien documenté, mais qui nécessite encore des recherches approfondies lorsqu'il s'agit de cibler la filtration spécifique et précise d'éléments rares au sein d'un milieu complexe. En effet, des solutions innovantes pour le filtrage d'échantillons dans des milieux complexes pourraient être la clé de multiples problématiques liées à la santé et à l'environnement. Le sang est un exemple concret de milieu complexe : il contient une quantité importante et variée de cellules et de protéines, présentant une viscosité trois à huit fois supérieure à celle de l'eau, ainsi qu'un comportement non newtonien en écoulement.

Les applications cliniques de la filtration sanguine nécessitent le traitement de grands volumes de sang, soit en raison de la rareté des éléments ciblés (dans le cas de la capture des cellules tumorales circulantes, la pertinence clinique commence à 5 CTC/mL de sang), soit parce que l'ensemble du sang circulant doit être purgé d'entités indésirables (telles que des agrégats cellulaires ou des microparticules circulantes dans les maladies cardiovasculaires et les accidents vasculaires cérébraux). Enfin, la nature biologique des éléments ciblés peut introduire une variabilité dans leur taille et leur forme, posant ainsi des défis fluidiques pour leur récupération au sein de tels milieux. La filtration sanguine est un processus central dans l'hémodialyse, la surveillance des maladies cardiovasculaires et les applications de biopsie liquide basées sur la capture sélective des cellules tumorales circulantes (CTC), entre autres contextes cliniques.

Pour de telles applications, la micro et nano fabrication utilisant des méthodes et des techniques de précision de l'industrie des semi-conducteurs offre la possibilité de contrôler avec une grande précision la taille des pores de filtration par rapport à la taille des éléments ciblés nécessitant une filtration. Ce niveau de précision dans le processus de fabrication ouvre la voie à la rétention exclusive de l'élément ciblé, conduisant à l'information biologique dans le cas d'une application diagnostique, ou à la pathogénicité dans le cas d'applications thérapeutiques, sans altérer la composition du sang élué.

Cependant, en raison du traitement d'un grand volume de sang et de la présence de millions de globules blancs et de milliards de globules rouges par millilitre de sang, de tels filtres microfabriqués sont sujets à l'obstruction due à l'accumulation de matériau retenue au fil du temps. Ce désavantage incite au développement d'une méthode in-situ capable de détecter la densité cellulaire à la surface de ces filtres pendant leur utilisation, afin de surveiller leur saturation en vue de nettoyer leur surface ou de procéder à leur remplacement par d'autres filtres.

Dans ce contexte, nous proposons des dispositifs microfabriqués en salle blanche capables de répondre à ces exigences. Les dispositifs de détection produits combinent une membrane de filtration avec une méthode de détection cellulaire électrique in-situ à

travers des microélectrodes interdigités et des mesures de spectroscopie d'impédance. Malgré l'utilisation de pores de filtration à l'échelle du micron et de dispositifs microfabriqués, nous proposons un design spécifique permettant la filtration sanguine à un débit élevé (11,5 mL/min), bien supérieur à celui des dispositifs microfluidique habituels. Enfin, nous démontrons que des mesures électriques stables peuvent être réalisées dans du sang entier à des débits élevés pour surveiller la saturation du filtre par les cellules retenues.

De plus, l'analyse fine des cellules capturées, habituellement confiée à des laboratoires externes, pourrait être transférée au chevet du patient tout au long du traitement des échantillons, si une analyse in-situ et une phénotypisation en temps réel des cellules collectées par leur signature électrique pouvait être démontrée. Cet aspect sera abordé à travers la conception et la fabrication de dispositifs de filtration dédiés, élargissant ainsi le champ d'application de la détection électrique sur une membrane de filtration au sein d'une puce microfluidique.

La recherche au cœur de cette thèse de doctorat a été mise en œuvre au LAAS-CNRS, un laboratoire de recherche académique de l'organisation CNRS hébergeant une salle blanche. Le projet a été développé en étroite collaboration avec une jeune entreprise développant des solutions pour les applications de biopsie liquide : SmartCatch.

Table of Contents

Acknowledgement i
Abstract ii
Resumé iv

1 From Capturing Biological Elements in a Complex Biofluid to *in-situ* Detection and Analysis 1
1.1 General Introduction 1
1.2 Medical Applications 2
1.3 Benefit for Liquid Biopsy: Diagnosis, Prognosis, and Treatment . . . 3
1.4 SmartCatch: Capture of CTCs 5
1.4.1 S-Station 6
1.4.2 S-Pheresis 7
1.5 Electrical Detection and Analysis of Biological Cells 8
1.5.1 Benefit for liquid biopsy applications 8
1.5.2 Analytic introduction to dielectric properties and dispersion phenomena 9
1.5.3 Impedance Spectroscopy 15
1.5.4 Cell Detection Principle 22
1.5.5 Differentiation Principle 24
1.5.6 FEM Simulations 25
1.6 Thesis Objectives 26

2 Fabrication of a Whole Blood Filtration Device with an *in-situ* Electrical Detection of Cell Retention 29
2.1 Integration of Electrodes on Filtering Devices for Cell Density Detection 29
2.1.1 General Structure of the Detection System 29
2.1.2 Electrode Geometries 30
2.2 Micro-fabrication Process 36
2.2.1 Choice of Materials 36
2.2.2 Micro-Fabrication Techniques 38
2.2.3 Micro-Fabrication Process 46
2.2.4 Characterization of the Fabrication Process 47
2.3 Experimental Characterization of Microfabricated Devices 52
2.3.1 Experimental Platform 52

2.3.2 Experimental Protocol . . . 54
2.3.3 Biological Model . . . 55
2.3.4 Cell Capture Characterization . . . 57
2.3.5 Electrical Characterization of in-situ Cell Capture . . . 62
2.3.6 Analytical Description of the Equivalent Circuit Model . . . 72
2.3.7 Electrical Insights in the Capture Kinetics . . . 75
2.4 Conclusion and Perspectives . . . 78
2.4.1 Fabrication Process . . . 78
2.4.2 Towards Real Time Single Capture Event Detection . . . 79
2.4.3 Usability for Liquid Biopsy . . . 79

3 Towards *in-situ* Single-Cell Analysis and Phenotyping 81
3.1 Device for *in-situ* Electrical Sensing Combined with Imaging Characterization . . . 81
3.1.1 General Structure of the Analytical Device . . . 81
3.1.2 Geometry of Electrodes . . . 83
3.1.3 Device Integration . . . 85
3.2 Micro-Fabrication Process . . . 85
3.2.1 Silicon Process . . . 85
3.2.2 Glass Process . . . 92
3.3 Device Integration: ICHIP . . . 100
3.3.1 Stereolithography and Print Pause Print (PPP) Process . . . 100
3.3.2 ICHIP Fabrication . . . 100
3.3.3 Silanization Protocol of the Glass Coverslips for 3D Integration 103
3.3.4 Characterization of the 3D Integration . . . 103
3.3.5 Electrical Integration . . . 107
3.4 Experimental Platform and Automation . . . 112
3.4.1 Platform Description . . . 112
3.4.2 Experimental Protocol . . . 113
3.4.3 Python Automation . . . 114
3.5 Experimental Characterization of Microfabricated Silicon Devices . . . 115
3.5.1 Real-Time Cell Capture Observation . . . 115
3.5.2 In-Situ Cell Culture . . . 118
3.5.3 Electrical Characterization of Fabricated Devices . . . 120
3.6 Analytical Elements and Simulations . . . 125
3.6.1 Cut-off Frequency . . . 125
3.6.2 Device Sensitivity . . . 126
3.6.3 Parasitic Capacitance . . . 128
3.7 Conclusion and Perspectives . . . 129
3.7.1 Fabrication Process . . . 129
3.7.2 Integration Technique . . . 130
3.7.3 Electrical Developments and Automation . . . 131
3.7.4 Perspectives . . . 131

4 General Conclusion **133**

Bibliography **137**

Nickel-Based Devices Fabrication Process **145**

Silicon-Based Devices Fabrication Process **149**

Glass-Based Devices Fabrication Process **153**

Silanization Process **155**

Scientific Production **157**
.1 Publications 157
.2 Conferences 157

1 From Capturing Biological Elements in a Complex Biofluid to *in-situ* Detection and Analysis

1.1 General Introduction

The process of sample filtration from complex media is a current technological challenge. However, innovative solutions for sample filtering of complex media may hold the key to many health-related and environmental issues. Complex biological media are characterized by a large density of particles, in which the particle size and type may vary within the sample and possibly from sample to sample. Therefore, the retrieval of targeted elements within such media brings many challenges which mainly derive from the high density of elements within these media.

Filtration systems have a wide range of applications in different fields such as wastewater treatment systems, food and pharmaceutical industry, domestic and healthcare.

Indeed, ecological concerns keep rising following research breakthroughs on water contaminants emanating from industrial activities and mass consumption. For instance, the breakdown of large plastic pollutants in seas, leading to micro and nano plastic formation and contamination (<5mm) which may then interact with living organisms of the marine ecosystems and spread to other ecosystems, including humans through polluted drinking water [1, 2]. Recent research on microplastics demonstrated the presence of microplastics in human whole blood and evaluated it at a concentration of 1.6 µg/mL [3]. The presence of microplastics in the human body is now well established, it can be linked to punctual acts such as surgery or ingestion along everyday life [4] and, although the genotoxic potential of microplastics in human peripheral blood lymphocytes is well known [5], sampling and characterization methods are still in development [6] due to the complexity of both particles (in size and heterogeneity) and their environment (body fluids, organ tissues...). These methods require further improvements to provide biologists with a wide and representative range of in-vivo collected microplastics among a variety of populations to assess their cytotoxicity but also their impact on long term health issues [7]. On a close topic,

the recent discovery of the adverse impact of per- and poly-fluoroalkyl substances (PFAS) commonly used in the industry for packaging, fabrics ... and their spreading through rivers and groundwater, and have been tied to health-related issues following drinking water pollution [8–10].

On the other hand, filtration systems are already well implanted in healthcare applications through dialysis systems. However, the rising interest in liquid biopsy for pathology study through the retrieval of indicators, called biomarkers, of said pathology is bringing challenges due to the complexity of the samples from which these biomarkers must be retrieved. This aspect of filtration will be discussed in upcoming chapters.

Filtration systems are therefore still the subject of intense research activities and, with the use of clean-room microfabrication techniques, may be enhanced in their accuracy and functionalities. However, such developments must be well-though in order not to contribute to and exacerbate the original issue: *Primum non nocere*[1].

1.2 Medical Applications

Blood is a biological fluid of very high interest for many clinical applications due to the presence of a large variety of diseases linked circulating biomarkers that can be the target of medical diagnosis strategystrategies [11–13], but also for removing specific undesirable elements from the circulating blood [14, 15]. Blood filtration is therefore a process central in hemodialysis [16], cardiovascular diseases monitoring [17], but also in liquid biopsy applications based on the selective capture of Circulating Tumor Cells (CTCs), among other clinical contexts [18].

More generally, whatever the final clinical purpose of blood filtration, different constraints need to be considered for designing the sifting system. Blood is a complex medium containing a huge quantity and variety of cells and proteins exhibiting a viscosity 3 to 8 times greater than water and exhibiting non-Newtonian behavior when flowing [19]. Large volume of blood needs to be processed either because of the scarcity of the targeted elements (for example in the case of CTC capture, clinical relevance starts at around 5 CTCs/mL of blood) or because the whole circulating blood needs to be expurgated from some adverse entities (such as for example cell aggregates or circulating microparticles in stroke and cardiovascular diseasesdisease [15]). The pore size of the sifting elements needs to be controlled with high accuracy to retain only the targeted element driving the biological information in the case of a diagnosis application or driving the pathogenicity in the case of therapeutic applications without impairing the composition of the eluted blood. However, because a large volume of blood is processed and due to the presence of millions of white blood cells (WBC) and billions of red blood cells (RBC) per milliliter of blood, the filters

[1] first, do no harm

are subjected to clogging due to the unwanted accumulation of material unavoidably retained among time. This drawback appeals in-situ method capable of sensing during use, the cell density at the surface of these filters to monitor their saturation to clean their surface or to proceed to their replacement by fresh ones.

1.3 Benefit for Liquid Biopsy: Diagnosis, Prognosis, and Treatment

Liquid biopsy is a non-invasive technique based on the detection and analysis of tumor biomarkers, such as circulating tumor DNA (ctDNA), circulating tumor cells (CTCs) and microRNAs, in blood or other body fluids (see figure 1.1). Liquid biopsy offers several advantages over tissue biopsy:

Non-invasivity: Liquid biopsy requires no tissue sampling, making the procedure less invasive, less painful, and less risky for the patient. It can be performed using a simple blood or urine sample, making sample collection easier and less costly.

Repeatability: liquid biopsy can be performed several times over time, unlike tissue biopsy, which can only be performed once. This makes it possible to monitor tumor evolution by providing information on the evolution of tumor markers and the emergence of new resistant mutations, and thus potentially adapt treatment accordingly. Patients at high risk of recurrence or development of new tumor lesions would also benefit from such monitoring.

Sensitivity: liquid biopsy can detect gene mutations and specific tumor markers at very low levels, even before solid lesions develop, and which could therefore not be detected by tissue biopsy.

Versatility: liquid biopsy can be used to detect and analyze different types of tumor biomarkers, such as circulating tumor DNA (ctDNA), circulating tumor cells (CTCs), microRNAs, proteins and metabolites. This comprehensive analysis would make it possible to account for the genetic heterogeneity of the disease, and thus tailor treatments.

While tissue biopsy remains the gold standard for both cancer diagnosis and treatment, liquid biopsy is emerging as a complementary technique. It has already demonstrated its usefulness in many areas, including early detection of cancer (diagnosis), monitoring of treatment efficacy and detection of drug resistance (prognosis) and its adoption for routine clinical use is discussed [21].

Clinically, CTCs allow for a detection of asymptomatic early-stage tumors before traditional Computed-Tomography Scan (CT scan) detection. At another stage of development of the pathology, they can also provide a strong insight for minimal residual disease, as well as on biological mechanisms of tumor progression and drug resistance [22–25]. Finally, a large interest of the community is turned towards

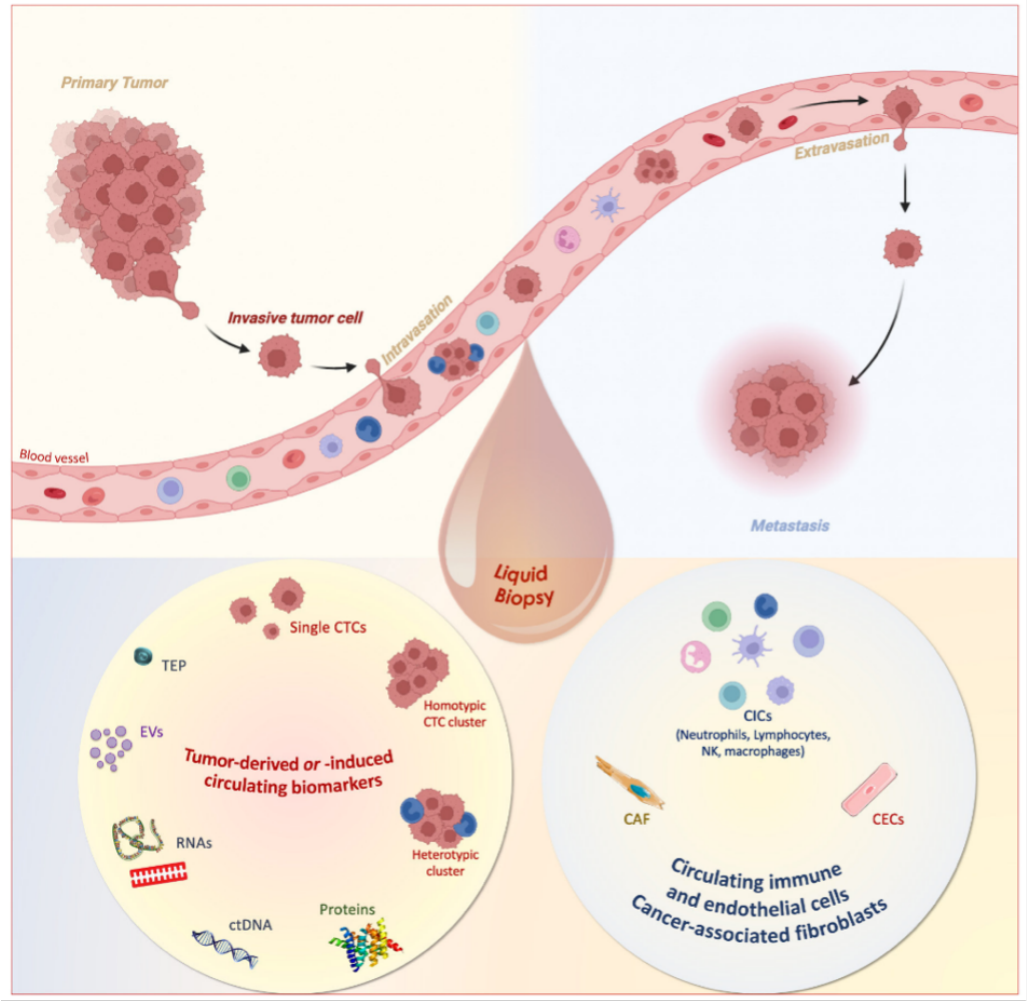

Figure 1.1: Tumor-derived or tumor-induced circulating biomarkers and circulating immune and endothelial cells as liquid biopsy for precision medicine. In a non-invasive sample, complementary circulating biomarkers can be isolated from the blood, counted and characterized. In the plasma or serum, extracellular vesicles (EVs), proteins, circulating cell-free tumor nucleic acids (circulating tumor DNA (ctDNA), non-coding and messenger RNAs), tumor-educated platelets (TEPs) can be found. In the cellular fraction, circulating tumor cells (CTCs; single, homotypic and heterotypic microemboli), circulating immune cells (CICs) and circulating endothelial cells (CECs) as well as cancer-associated fibroblasts (CAF) can be detected. NK stands for Natural Killer [20].

large blood sample processing for both diagnosis and CTC removal by assistance of hemodialysis or leukapheresis modified techniques, as a potential post-surgery cancer therapies [26–29].

Research is currently underway to extend the use of the liquid biopsy principle to treatment. It is known that certain tumor biomarkers, such as circulating tumor cells, are at the root of the phenomenon of disease propagation via metastasis. The idea is therefore to periodically extract these biomarkers emitted by a cancerous tumor from the bloodstream by apheresis-type filtration, to slow or even block its spread to other organs.

Liquid biopsy, while promising for its apparent ease of clinical implementation (blood sampling, urine collection...), faces difficulties linked to the complexity of samples in which tumor biomarkers can be found in trace amounts among millions of other biological elements present. Similarly, each tumor biomarker is subject to biological variability (size dispersion, phenotype, gene expression) and can also interact strongly with its microenvironment to avoid immune system detection. Thus, liquid biopsy is faced with the challenge of extracting information, both from the biological variability of biomarkers and from the complexity of the environments from which they must be extracted.

1.4 SmartCatch: Capture of CTCs

It is against this backdrop that a project to develop microdevices for liquid biopsy, more specifically for the capture of CTCs, has been running since 2012 within the Systems Architecture and Analysis Laboratory (LAAS-CNRS) under the direction of Aline Cerf, CNRS research fellow. The SmartCatch start-up, created in 2016, is the fruit of the technology transfer of this project following several years of research with promising results. It was founded by 4 associates who are Aline Cerf, the aforementioned project leader, Christophe Vieu, professor at the Institut National des Sciences Appliquées de Toulouse (INSA) and researcher at LAAS-CNRS, Bernard Malavaud, urological surgeon at the Institut Universitaire du Cancer de Toulouse (IUCT) and Sylvain Sanson, urological surgeon at the Uropôle de Montauban. The start-up is currently based at the Centre Pierre Potier, a business incubator dedicated to biotechnologies, and its staff consists of the Administration team, as well as three departments: Research and Innovation, Product Development and Quality and Marketing.

The heart of the innovation lies in the design of a cell trap in the form of a micrometric sieve which, thanks to its design, enables specific isolation of CTCs in a single step from whole blood. Tumor cells are isolated on the basis of physical criteria (size, deformability) under gentle fluidic conditions that preserve their viability and the integrity of the biological information they contain. Accuracy and reliability of

information are important criteria, but SmartCatch also focuses on the criteria of speed and ease of access to quantitative capture information. With this in mind, products are designed to enable optimal capture of CTCs, but also to ensure that these devices could be connected and able to return capture enumeration information to the oncologist in real time. SmartCatch is developing a range of compact, portable products for use in consulting rooms and routine clinical practice. The start-up's aim is to democratize liquid biopsy, so that it can become the essential medical procedure for diagnosis, follow-up and personalized care in medical oncology.

The technological base developed by the start-up is the Micro Device for Capturing Circulating Tumor Cells, based on the principle of blood microfiltration, and whose design is the fruit of 7 years' research. In the remainder of this manuscript, we refer to this device as the S-MDC. The S-MDC can be embedded on two types of fluidic platforms to perform cell capture, which constitutes two product lines:

1.4.1 S-Station

The portable benchtop device for automated isolation of CTCs from blood samples without pretreatment, in a single step and in just a few minutes. Isolated CTCs are viable with low levels of contamination, compatible with single-cell DNA/RNA sequencing technologies. This product will be marketed to pharmaceutical and academic laboratories for the search for therapeutic targets, for studies on drug resistance or cellular heterogeneity, or as a companion kit for new treatments such as immunotherapy.

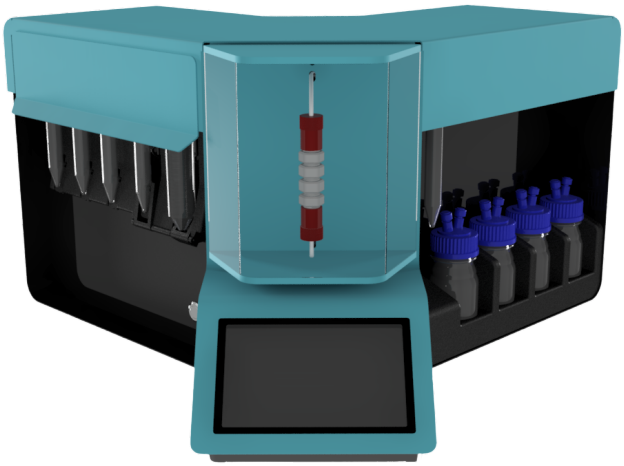

Figure 1.2: Representation of the Station prototype with, on its left and right the reagents (tubes and bottles). In the center are placed the capture devices within 3D printed holders which are connected to the fluidic system. below the processing area is the tactile panel allowing for control and real time follow up of the sample processing.

1.4.2 S-Pheresis

The extravascular apheresis CTC isolation system for continuous collection of CTCs directly from a peripheral vein at the patient's bedside. The system filters blood via an S-MDC device, then reinjects it into the vein. In this way, it samples a much larger volume of blood. This product, integrated into current hospital sampling systems, will be used at the patient's bedside, as part of a clinical routine for therapeutic monitoring and treatment purposes (see figure 1.3).

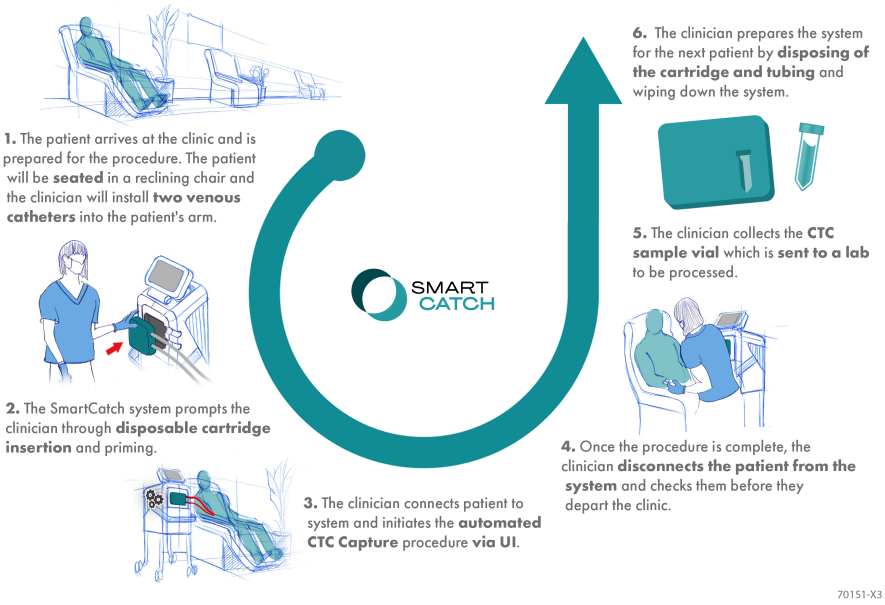

Figure 1.3: Pheresis clinical workflow for the retrieval of Circulating Tumor Cells from patient's organisms.

It is in the context of the development of SmartCatch technology that this CIFRE thesis project is being carried out, in collaboration between SmartCatch and the ELiA (Engineering for Life Applications) team at LAAS-CNRS.

1.5 Electrical Detection and Analysis of Biological Cells

To further extend the usability of microfabricated devices for liquid biopsy, the integration of electrical sensing capability to the filtering membranes is the core of this work. We will herein present the usability of such addition for liquid biopsy and more specifically for cellular characterization within complex samples. The electrical behavior of biological samples will be discussed through analytical tools combined with conventional equivalent electrical circuit model, thus paving the way for conceptualization of two kinds of sensing membrane which will be presented respectively in the following chapters of this manuscript. Future experiments on fabricated devices will also refer to the current chapter as the ground for electrical characterization and result interpretation. Finally, FEM simulations will be used to confirm the analytical developments together with modeling the undesirable effects.

1.5.1 Benefit for liquid biopsy applications

The liquid biopsy is usually compared to the solid biopsy, which is still, as of today, the gold standard for cancer diagnosis. Although the liquid biopsy can offer several advantages, it currently only provides a way for sample collection and rare elements retrieval. Sample analysis is therefore deported as it is commonly done with tissue biopsy samples.

Capture techniques based on the affinity in between an antibody and antigen are said to be selective in the way that they only target the elements displaying at their surface the selected antigen or in the case of protein biomarkers the antigen itself. However, their specificity limits their universality because it relies on strong biological a priori which could be resumed by saying that the only biomarkers of interest for a given pathology are those presenting the selected antigen. In the real life, it is well known that biomarkers of interest can be heterogeneous, can suffer from phenotypic evolution during disease progression, or also genetically mutate and therefore all the biomarkers of interest will never be collected by an affinity technique using a single capture antibody. Moreover, biomarker capture through immunoaffinity is usually either performed through expensive cytometry machines or on specifically designed and functionalized substrates, thus further limiting sample analysis.

As discussed previously, the mechanical filtering mechanism intends to fill this gap by capturing a broad range of biomarkers with potential mutations, thus allowing a better understanding of the heterogeneous tumoral environment. This method is also limited by the sample analysis post capture. Indeed, sample handling needs to be done by qualified biologists using specific equipment with potential sample denaturation. This step requires both resources such as advanced lab equipment

which may not be available in some countries and may be time-consuming (a few days to weeks) when some cancers are fast-spreading and require immediate medication.

We aim to address this challenge through the integration of sensing electrodes on the membrane for in-situ characterizing the biological occupation of the membrane. This first step will pave the way for in-situ characterization of the biological samples.

Indeed, as it will be discussed in the upcoming sections, cells present a typical electrical signature which changes in between cell types and can be detected through impedance spectroscopy. These signatures may therefore be used to characterize in-situ the phenotype of the captured cells which could be useful in the case of CTCs based liquid biopsy.

1.5.2 Analytic introduction to dielectric properties and dispersion phenomena

Simplified biological description

The eukaryotic cells are composed of numerous organelles and, in contrast to prokaryotic cells, have a compartmentalized nucleus enveloped by a nuclear membrane (see figure 1.4). The diameter of eukaryotic cells varies from 10 µm to 100 µm. A cell is constituted of a plasma membrane that separates the intra- and extracellular environments. The contents of the cell, known as the cytoplasm, are 80% water, mineral salts and organelles that carry out the cell's functions. The cell nucleus contains the genetic information contained in deoxyribonucleic acid (DNA) molecules. Among the organelles with important roles, the mitochondria store and produce energy necessary for cell function, while the Golgi apparatus together with the endoplasmic reticulum store and secrete proteins, and lysosomes are involved in cell digestion. The plasma membrane consists of a phospholipid lipid bilayer 5 nm thick. Transmembrane proteins cross the lipid bilayer, and some form narrow channels for the circulation of water, ions, or specific molecules.

This complex architecture and the perpetual biological activities linked with metabolism, gene expression, protein traffic, adhesion, cell division, migration, exchange of molecules with the extracellular medium among other cell mechanisms, involve the displacement of many electrical charges rendering the modeling of the electrical properties of a cell particularly tricky. However, operating a drastic simplification of the biological system, it turned out interesting to describe a living cell as a quasi-spherical element composed of a lossy dielectric material. Following this reduction scheme, the analysis of dielectric dispersion within a medium containing cell has proved to be a preferred experimental means in this field.

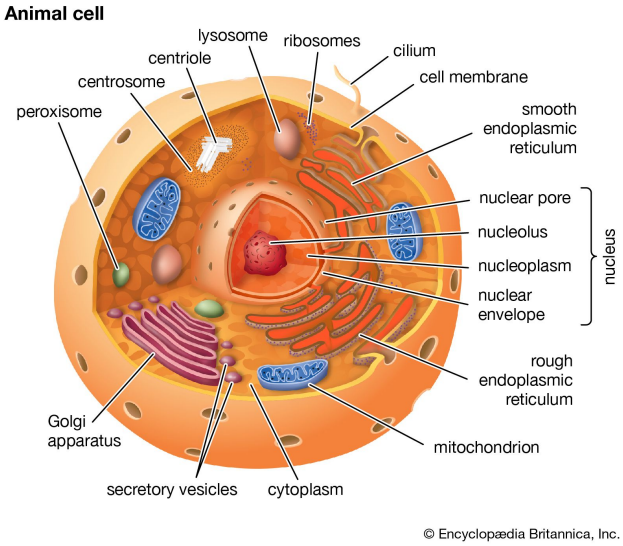

Figure 1.4: Cutaway drawing of a eukaryotic cell from Encyclopædia Britannica [30].

Electrical dispersion of biological cells

The history of electrical characterization and modeling of biological material was summarized by Foster and Schwan [31] in their review of the field in 1989.

Key historical events can be reported here. Indeed, the understanding before World War I is that scientists recognized that a tissue conducts electricity, that its resistance varies with frequency and that the mechanism for electrical conduction is the movement of ions. It is in between world wars that Fricke, Curtis and Cole entered the field among others and developed advanced instrumentation for the measurement of conductivity and permittivity over a wide frequency range, thus contributing to understand the beta dispersion band for cell suspension [32]. World War II stimulated the development of microwave technology which were soon adapted for dielectric studies on biological material. Rajewsky and Schwan [33] reported in 1948 the complex permittivity data on blood up to 1 GHz, thus discovering the existence of new dispersion regions. Herman Schwan pioneered the study of the dielectric spectrum over a wide frequency range, and in particular characterized cell suspensions and biological tissues. He identified the main α, β and γ dispersions describing the frequency dependence of the dielectric properties of biological tissues and cell suspensions. These types of dispersion are displayed in figure 1.5:

- **Dispersion** α occurs at low frequencies down to a few kilohertz. When an electric field is applied, ionic diffusion takes place at the surface of the plasma membrane. The plasma membrane exhibits a capacitive behavior that prevents the electric current from reaching the intracellular medium;

- **Dispersion** β occurs in the frequency range of 250kHz to 20MHz. This dispersion is mainly due to the polarization of the plasma membrane. This dispersion is related to Maxwell-Wagner relaxation at the cell membrane interface. Maxwell-

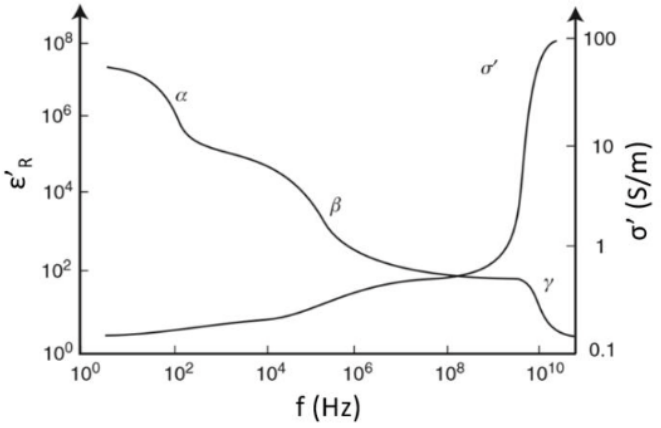

Figure 1.5: Response of cell suspension as a function of the frequency of applied electrical excitation. Evolution of the real part of relative permittivity (ϵ_r) and conductivity (σ) as a function of frequency and highlighting of dispersions α, β, γ. Representation from a review by G. Martisen and S. Grimnes [34]

Wagner relaxation is linked to interface polarization typical of heterogeneous dielectric media. At these frequencies, the plasma membrane no longer behaves like an insulator, and electric current can flow through it into the intracellular medium;

- **Dispersion** γ occurs in the microwave frequency range (1 GHz to 300 GHz). This dispersion is due to the presence of water in the cells. The dipolar orientation of water molecules relaxes at 20 GHz. At these frequencies, the plasma membrane is electrically transparent, giving access to the intracellular medium.

These dispersions were reported analytically by K. R. Foster and H. P. Schwan [31] who described the relaxation theory by which the frequency dependence of the dielectric parameters is accounted for through the Debye equation [35] for a single relaxation region:

$$\epsilon^* = \epsilon_\infty + \frac{\epsilon_s - \epsilon_\infty}{1 + j\omega\tau} \tag{1.1}$$

where ϵ_∞ is the permittivity at high frequencies ($\omega\tau >> 1$), ϵ_s denotes the permittivity at low frequencies ($\omega\tau << 1$) and τ [s] the dielectric relaxation time. The magnitude $\Delta\epsilon$ of the dispersion is then given by $\epsilon_s - \epsilon_\infty$. The Cole-Cole equation introduces the distribution parameter α to empirically account for the broadening of dispersion regions of complex biological materials. W. D. Hurt [36] modeled in 1985 the dielectric spectrum by adding the static ionic conductivity term σ_i into the summation of n Cole-Cole dispersion, as follows:

$$\epsilon^*(\omega) = \epsilon_\infty + \sum_n \frac{\Delta\epsilon}{1 + (j\omega\tau_n)^{1-\alpha_n}} + \frac{\sigma_i}{j\omega\epsilon_0} \tag{1.2}$$

Parameters used to predict the dispersion of blood with the above-mentioned

equation were reported by S. Gabriel & al. [37] in 1996 and are the result of a fitting process over experimental data. The frequency behavior of ϵ^* for whole blood is depicted in figure 1.6. We can see that, compared to a suspension of cells as shown in figure 1.5, whole blood dispersion is not the same, hence, cell differentiation based on their electrical dispersion will also need to consider the dispersion of the cell environment (whole blood).

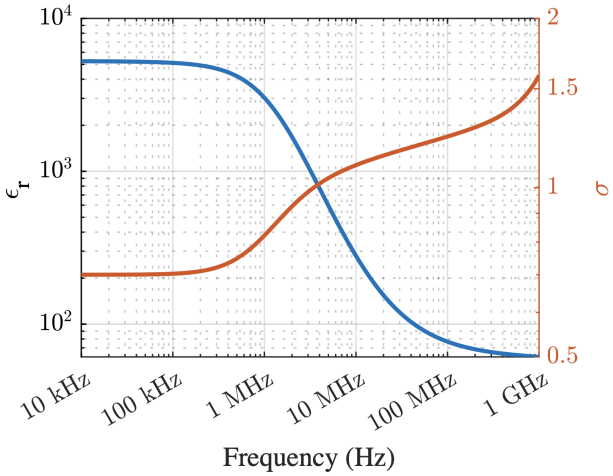

Figure 1.6: Blood dispersion (relative permittivity ϵ_r and conductivity σ) following the behavior of ϵ^* with parameters reported by S.Gabriel & al [37].

Electrical modeling and characterization of cells

Since the application of our sensor is turned towards the detection of cancer cells, it is interesting to look at the biological characteristics of these cells compared to healthy cells. Moreover, and as it will be discussed in upcoming chapters, cancer cells are often used as models to mimic circulating tumor cells during the first development phases of technological prototypes.

Indeed, as shown on figure 1.7, cancer cells differ from healthy cells by a series of morphological properties among which the membrane roughness together with the overall cell size and shape are the most impacting on the electrical standpoint.

The cell plasma membrane of cancerous cells is not smooth but includes both small and large cell surface features such as microvilli, folds, and ruffles. Cancer cells thus exhibit larger membrane surface areas in comparison to idealized smooth spheres of a similar volume such as non-cancer cells. The folding factor of the membrane was therefore introduced for the first time in 1994 by Wang & al. [39] to account for the excess amount of total surface area of an actual cell compared to a smooth cell with the same volume. Gascoyne & al. [40] who pioneered the study of dielectric properties of cells through electrokinetic technics, considered a membrane's folding factor, ϕ, as a parameter in the characterization of electrical behavior of cancer cells, in order to determine the excess amount of total surface area of an actual cell compared to a

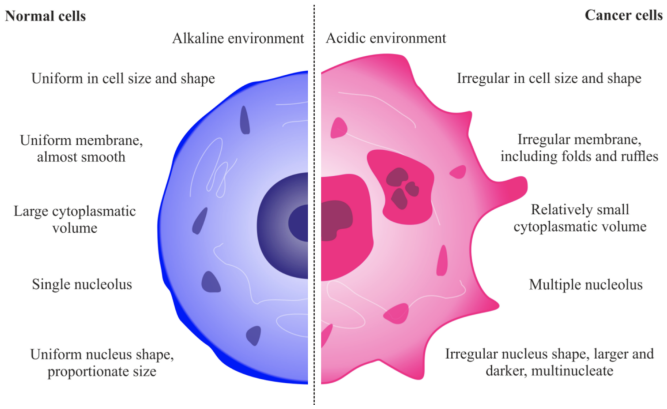

Figure 1.7: General comparison of healthy cells versus cancer cells [38].

smooth cell with the same volume as shown in figure 1.8. The surface morphological parameter M follows a visual scoring system:

$$M = \frac{F + P + R}{3} \tag{1.3}$$

with cell flattening (spreading) on the surface of the culture flask (F), cell elongation or the presence of long dendritic projections (P), and cell membrane roughening associated with ruffles, folds and microvilli that contributed to specificity of the cell surface and margins. On this scale, M=1 corresponds to a smooth, round cell with no spreading or surface projections while M=3 corresponds to a highly flattened cell with extensive projections and striking surface roughness. The membrane folding factor ϕ is expressed as:

$$\phi = A(3V\sqrt{4\pi})^{-\frac{2}{3}} \tag{1.4}$$

with the plasma membrane area, A and a cell volume V.

The alignment of the points among very different cell types popularized the notion of a cell dielectric phenotype such as Rϕ with R the cell radius and ϕ the folding factor of the membrane.

figure 1.9 shows for example a visual summary of the DEP response of NCI-60 cancer cells panel[2] and normal blood cells expressed in terms of the reciprocal cell dielectric phenotype. These results demonstrate a significant dielectric difference between healthy blood cells and cancer cells.

Electrokinetic methods allowed a precise characterization of the dielectric properties of cells, demonstrating the utility of electrical analysis for direct phenotyping through the differentiation of cell types [43]. Multishell models accounting for the

[2]The NCI-60 cancer cell line panel is a group of 60 human cancer cell lines used by the National Cancer Institute (NCI) for the screening of compounds to detect potential anticancer activity [42].

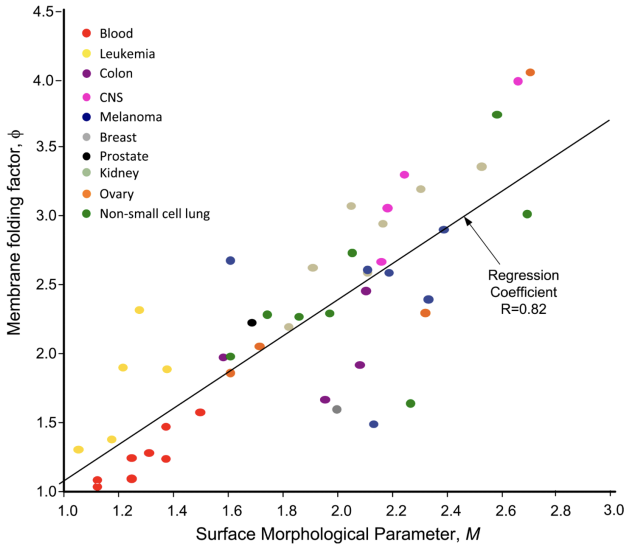

Figure 1.8: Relationship between the membrane folding factors of the NCI-60 cell panel as measured by DEP-FFF in cell suspension and the cell exterior morphologies in culture just prior to harvest as judged by visual estimates of the combination of spreading, elongation, and surface roughness. Blood cell types are plotted based on DEP derived folding factors with estimates of their morphological scores based on micrographs in the literature [40].

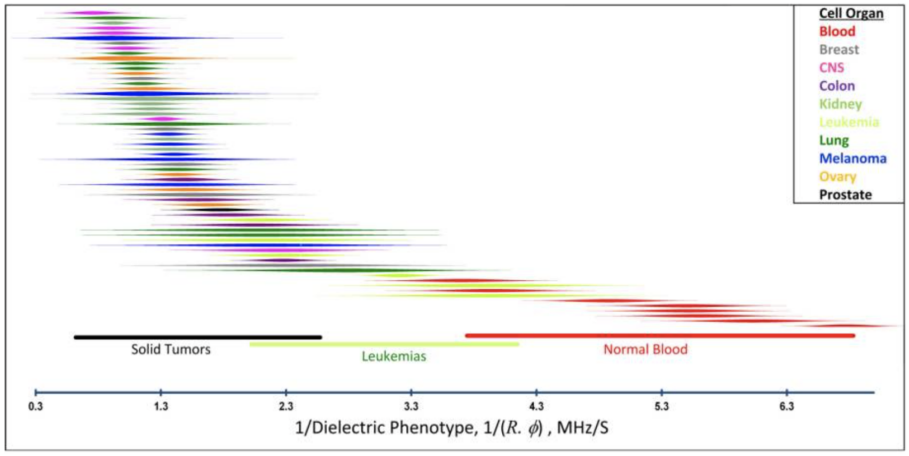

Figure 1.9: DEP responses of cancer and normal blood cells expressed in terms of the reciprocal cell dielectric phenotype (1/Rϕ). Each line shows the distribution of crossover frequencies among cells of a single cell type. Cell types are color-coded by organ of origin [41].

biological complexity of cells (membranes, cytoplasm and organelles, see figure 1.10) where developed following Fricke first demonstration of the stratified sphere models in 1954 [44]. These models enable to calculate the effective complex permittivity of biological cells based on the dielectric properties of each shell representing biological membranes (dielectric) or electrolytes (conductive) layers. Moreover, through curve fitting of experimental data, multishell models allows for the interpretation of the dispersive signal by quantifying each layer with dielectric properties.

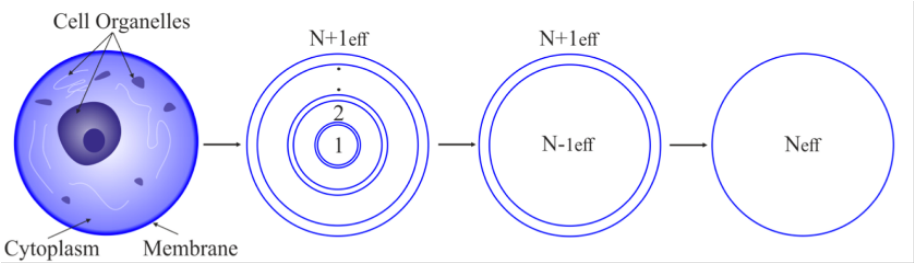

Figure 1.10: Schematic approach of multishell model for calculation of effective complex permittivity of a biological cell with N shells that represents its organelles and sequential simplifications for obtaining one equivalent homogeneous cell.

Through these models, a large database on dielectric properties of specific membrane capacitance and cytoplasmic conductivity has been established and was compiled by Turcan & al. [38]. This data may be further used to discriminate cell types based on the measured electrical dispersion.

As an example, B-Lymphocytes specific membrane capacitance ranges from 9.9 to 14 $\mu F.m^{-2}$ with a cytoplasmic conductivity of 0.65 $S.m^{-1}$ whereas prostate cancer cells PC3 used in this work exhibit a membrane capacitance of 22.4 ± 3.7 $\mu F.m^{-2}$ and a cytoplasmic conductivity of 0.47 ± 0.09 $S.m^{-1}$.

Hence, based on the previous work presented above, and through impedance spectroscopy technique, this work aims at detecting biological cells and differentiate healthy cells from cancerous ones based on their electrical dispersion.

1.5.3 Impedance Spectroscopy

As discussed previously, kinetics techniques such as electrorotation or dielectrophoresis are used to evaluate the electrical properties of different cell types. However, for a precise characterization, such techniques require a stable environment without fluidic turbulence together with an optical characterization and their implementation is not currently possible inside whole circulating blood.

However, impedance spectroscopy can operate on its own. Its working principle is based on the application of a small, frequency-dependent, time-harmonic voltage $V(\omega)$ and the recording of the resulting time-harmonic current $I(\omega)$. The application of Ohm's law then determines the complex electrical impedance $Z(\omega)$ as:

$$Z(\omega) = \frac{V(\omega)}{I(\omega)} = Z_{RE} + iZ_{IM} \tag{1.5}$$

with Z_{RE} and Z_{IM} the real and imaginary part of the impedance. Therefore, Z_{RE} relates to the resistive part of the system whereas Z_{IM} to the capacitive or inductive part. Then, the impedance components can be referred to as the magnitude or modulus $|Z(\omega)|$ and phase of the signal $\theta(\omega)$ through the two following equations:

$$|Z(\omega)| = \sqrt{Z_{RE}^2 + Z_{IM}^2} \tag{1.6}$$

$$\theta(\omega) = \arctan(\frac{Z_{RE}}{Z_{IM}}) \tag{1.7}$$

Impedance spectroscopy is a general measurement method allowing probing a component or a system of multiple components at once and evaluate its response to a stimulus within a frequency range. Applied to biological samples, it therefore allows rendering the complexity of the electrical dispersion of a sample as shown on figure 1.11, while allowing high-rate measurements at a specific frequency for rapid detection systems.

Figure 1.11 shows a typical impedance spectrum together with the equivalent electrical circuit model used for impedance interpretation. Equivalent circuits, which will be discussed in the upcoming section, are at the core of impedance measurements and allow, through the analogy with electrical circuit components and curve fitting, to quantify multiple elements within the system and interpret the impedance spectra with an underlying drastic simplification of the real cell, as explained before.

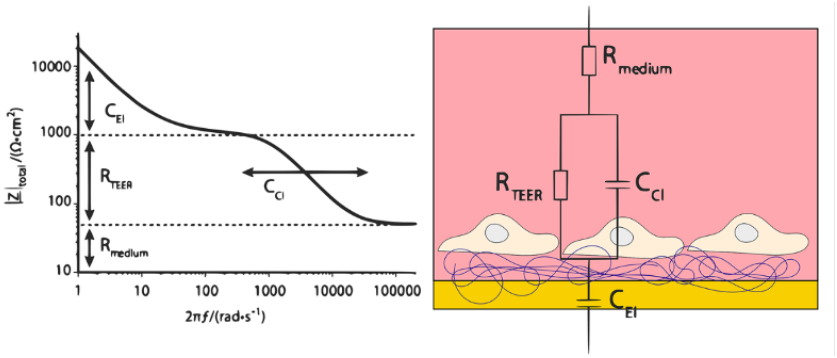

Figure 1.11: Equivalent circuit and typical impedance spectrum of cells in 2D composed of a transepithelial electrical resistance R_{TEER} in parallel with a capacitance induced by the cell layer C_{CL} and R_{MEDIUM} and C_{EL} respectively the medium resistance and the interfacial (electrode electrolyte) capacitance. The arrows on the impedance spectra (left) represent the impact of each electrical component on said spectra [45].

Impedance spectroscopy is well implanted within biological applications, in

particular for the study and follow-up of 2D [45–47] and emerging 3D [48] cell cultures. From already developed equivalent electrical circuits presented above and guidelines for impedance sensor design [49] together with strong databases of cell dielectric parameters, we therefore turned towards this characterization method for implementing an in-situ detection and analysis system on a filtering membrane.

Equivalent Electrical Circuit modeling

Schwan [50] reported in 1957 the first description of an equivalent electrical circuit used to model a single or multiple relaxation through conventional electrical components, such as resistors and capacitors as shown on figure 1.12.

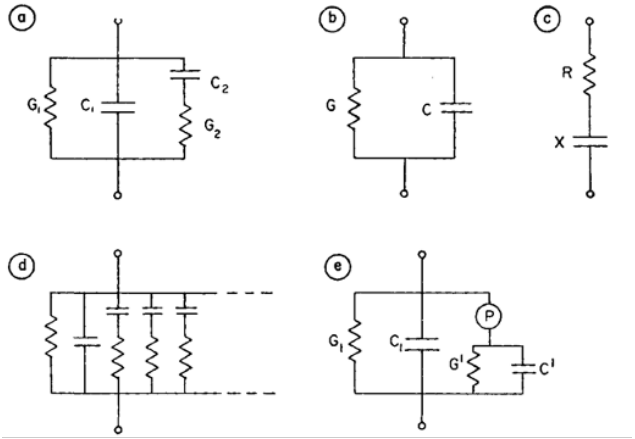

Figure 1.12: (a) Circuit simulating a single relaxation behavior; (b) equivalent parallel circuit; (c) equivalent series circuit; (d) and (e) circuits simulating relaxation behavior with several time constants.

Following these first applications of electrical circuit analogy for simulation, Foster and Schwan [31] reported in 1989 an equivalent electrical circuit to model the biological components of the cell: its membrane and cytoplasm as shown on figure 1.13. These models were then extended later to multishell models, attributing analogous electrical components to each layer to combine them in a single equation. When applied to biological elements, these equivalent circuits become useful for simulation and data interpretation by breaking down a complex impedance signal in a multitude of elements. On the other hand, one has to be careful when choosing an equivalent electrical circuit model as to not overfit the impedance data. In such case, fitted component values would not be tied to the biological analogy (membrane, cytoplasm, ...) anymore.

Finally, once the impedance data is well correlated by an equivalent circuit to the biology, components can be added to consider the impact of the sensor itself on measurements. This part will be discussed in the upcoming section through the introduction of a capacitor to model ionic double-layer effects or parasitic substrate effects and a resistor to model the resistance of access tracks, contact pads and

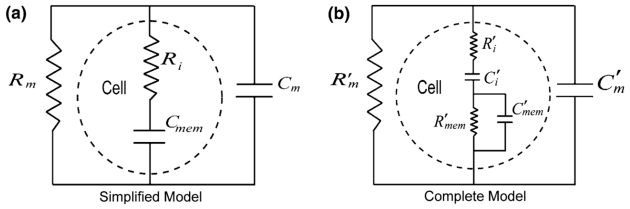

Figure 1.13: (a) Foster and Schwan's simplified circuit model for a single cell in suspension. The cell is modeled as a resistor R_i (cytoplasm) and a capacitor C_{mem} (membrane) in series. (b) Complete electrical circuit model for a single-shelled particle in suspension. The particle is modeled as a resistor R'_i and a capacitor C'_i in series (cytoplasm) in combination with a resistor R'_{mem} and a shunt capacitor C'_{mem} (membrane) [51].

electrodes.

Therefore, the electrical circuit analogy allows evaluating, through a single impedance equation, many effects of different natures, to quantify these effects and investigate their evolution. These models can then be simulated for each component individually or as a whole for sensor optimization.

Geometrical Description of Coplanar Electrodes

Although the electrical dielectric properties and the electrical circuit components were discussed in the previous section, geometrical information is still needed to solve the equations for multiple equivalent components and model the complete electrical circuit. However, the coplanar orientation of the electrodes brings complexity to these calculations which will be addressed in this section.

Indeed, for two parallel electrodes of equal surface A (m^2) and at a distance D (m) of each other's, the resistance R (Ω) is related to the solution conductivity σ_{sol} (S/m) by the following equation:

$$R = \frac{1}{\sigma_{sol}}\kappa \tag{1.8}$$

in which κ (m^{-1}) defines a geometrical constant which is described in the ideal case assuming a uniform current-line distribution perpendicular to the electrodes by:

$$\kappa = \frac{D}{A} \tag{1.9}$$

However, to find an analytical solution in the case of coplanar electrodes, conformal mapping techniques are used. This method consists of a change of coordinates, as shown on figure 1.14.

Through the conformal mapping from the (x,y) plane to the (u,v) plane, the

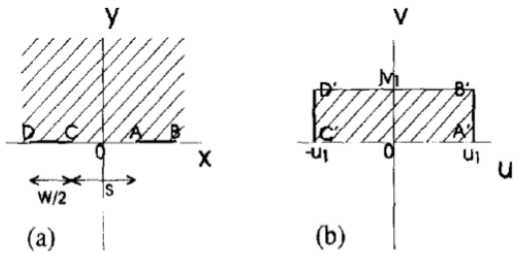

Figure 1.14: (a) Representation of the two-finger structure in the (x, y) plane and (b) after conformal mapping in the (u, v) plane [52].

resistance per unit of length R_1 can be written as:

$$R_1 = \frac{2u_1}{\sigma_{sol} v_1} \tag{1.10}$$

Following integral calculations, this resistance can be expressed as follows:

$$R_1 = \frac{2}{\sigma_{sol}} \frac{K(k)}{K(\sqrt{1-k^2})} \tag{1.11}$$

where $K(k)$ is the complete elliptic integral of the first kind defined as:

$$K(k) = \int_0^1 \frac{dt}{\sqrt{(1-t^2)(1-k^2t^2)}} \tag{1.12}$$

For two finger electrodes, k can be approximated by:

$$k = \frac{s}{s+w} \tag{1.13}$$

For more than two fingers, the periodicity of the structure requires another definition:

$$k = \cos(\nu \frac{\pi}{2}) \tag{1.14}$$

Finally, the cell constant κ depends on the number of digits N, their length L and, through the metalization ratio ν, on their width W and spacing S. It is given as follows:

$$\kappa = \frac{2}{(N-1)L} \frac{K(k)}{K(\sqrt{1-k^2})} \tag{1.15}$$

This cell constant reflects the form factor of the coplanar electrodes, interdigitated

or not. It is used to evaluate either the inter-electrode capacitance or resistance, depending on inter-electrode media type (conductive or dielectric). Indeed, following the development of a cell constant reflecting the form factor of the electrodes, we can derive the expression of both capacitive and resistive effects in the inter-electrode region:

$$C_{sol} = \frac{\epsilon_0 \epsilon_r(\omega)}{\kappa} \tag{1.16}$$

and

$$R_{sol} = \frac{\kappa}{\sigma_{sol}(\omega)} \tag{1.17}$$

It is interesting to note that the cut-off frequency f_c of such RC model is independent of the geometrical constant κ and relies only on the properties of the medium:

$$f_c = \frac{1}{2\pi \frac{\epsilon_0 \epsilon_r}{\sigma_{sol}}} \tag{1.18}$$

Medium-Electrode interface

One might infer that the combination of metallic electrodes with an electrolytic solution will induce an ideal ohmic contact. However, experimental data show a significant contact impedance induced by the difference in charge carriers: electrons in the metal versus ions in solutions. This contact impedance will be discussed in this section, as it will greatly impact sensors designed in upcoming chapters.

Indeed, to induce electrical current from an electrode into a flow, two solutions are possible. The first possibility is to transfer charges across the interface by oxidation or reduction of the material through electrolytic process. The so-called faradaic effect created can be modeled by a resistor and requires driving voltages larger than the electrochemical window of the electrode's material as to generate electrolytic effects. Although the cycle is symmetrical (oxidation and reduction), since the efficiency of it is not perfect, the electrodes will be gradually damaged. The second possibility consists of generating an alternating electric field in the solution through a capacitive effect, therefore coupling the ions to drift along with the driving electric force. The capacitance effect induced by the interface is well-studied and is now called the double-layer capacitance due to the formation of an ionic double-layer in the vicinity of the electrodes. This ionic layer as shown on figure 1.15 is composed of both a Helmholtz layer and a diffuse Gouy-Chapman layer [53]. The combination of both layer thicknesses is called the Debye length and is, for an electrolytic solution, expressed as:

$$\lambda_D = \sqrt{\frac{\epsilon_0 \epsilon_r k_B T}{\sum_i c_i^0 q_i^2}} [\mathrm{m}] \tag{1.19}$$

where $\epsilon_0\epsilon_r$ denotes the permittivity of the solution, T is the temperature in Kelvins, k_B designates the Boltzmann constant, and c_i^0 and q_i^2 are respectively the concentration (ions/m^3) and charge of ions in the solution. Finally, the induced capacitive effect can be modeled from the Debye length λ_D through a capacitance C_{dl} given as follows:

$$C_{dl} = \frac{\epsilon_0 \epsilon_r S}{\lambda_D} [\mathrm{F}] \tag{1.20}$$

where S is the electrode surface.

The electrodes are coplanar in this work, and the use of a geometrical constant is needed to account for this configuration, as demonstrated in the previous section. However, the ionic double-layer effect is at the interface in between the electrode and the electrolyte. Indeed, the calculated Debye length for a PBS solution was found to be of 0.7nm. We therefore assume that, at this length scale, the electrode and electrolyte are parallel and induce parallel field lines. Hence the equation of a classical parallel plate capacitor can be used to model the interfacial effects.

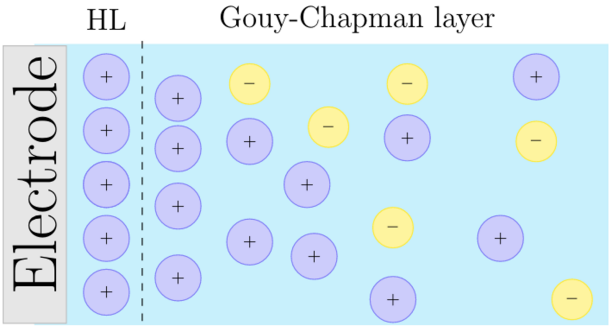

Figure 1.15: Schematic representation of the electrical double-layer combining the Helmholtz layer and the Gouy-Chapman diffusion layer.

In practice, the measured capacitance depends on the frequency, and to account for such behavior, a constant phase element (CPE) is often used during analysis of electrochemical impedance spectroscopy (EIS) instead of a pure capacitor [54]. The Constant Phase Element (CPE) element, first defined by Kenneth S. Cole [55], is therefore used here to model this capacitance as a non-ideal capacitor of impedance Z_{CPE} given by:

$$Z_{CPE} = \frac{1}{Q_0 (i\omega)^n} \tag{1.21}$$

with Q_0 [F s^{n-1} cm^{-2}] is the parameter defining the CPE with n $\in [0, 1]$ denoting

the so-called ideality coefficient and ω [rad s^{-1}] the angular frequency of the time-harmonic regime.

The complex plane impedance plots corresponding to both an ideal capacitor and a CPE model are shown in figure 1.16. In the case of the CPE, the vertical line changes to a line at a constant angle. In this case, the deviation from the ideal case $n = 0.9 = 1 - \alpha/90°$ and $\alpha = 9°$. Finally, Hsu and Mansfeld [56] estimated the averaged double-layer capacitance $\bar{C_{dl}}$ as:

$$\bar{C_{dl}} = Q_0(\omega_c)^{n-1} \tag{1.22}$$

where ω_c is the angular frequency corresponding to the maximum of the imaginary part, i.e. to the maximum of the semicircle on the Nyquist plot of a RC circuit.

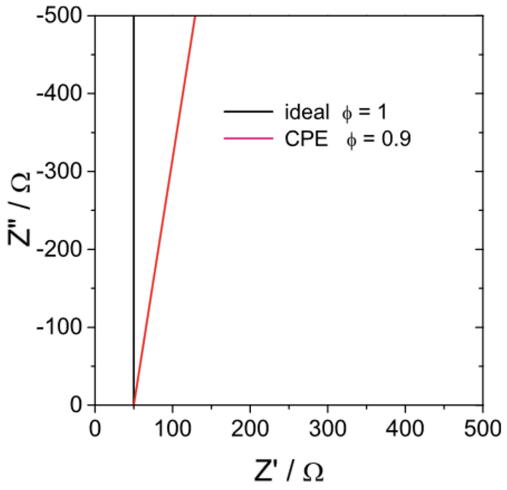

Figure 1.16: Complex plane plots (Nyquist) of an ideal capacitance (black) and CPE (red) for the following parameters: $C_{dl} = 20\mu F$, $n = 0.9$, and $Q_0 = 20\mu F\,s^{-0.1}$. A resistance of $R_s = 50\Omega$ was added for ease of reading. Z' and Z" respectively the real part and the imaginary part of the complex impedance Z [57].

1.5.4 Cell Detection Principle

Based on the shell model previously presented, biological cells can be modeled as a capacitive membrane together with a resistive cytoplasm. Hence, coupling this model with the equivalent electrical circuit of the medium, it is possible to draw the equivalent circuit shown in figure 1.17, representing the medium in presence of cells.

We observe that, based on the equivalent electrical circuit model, the detection can rely on the detection of intracellular components (membrane capacitance or cytoplasmic resistance) or on the modification of the medium elements (through its resistance or capacitance (R'_{sol} or C'_{sol}). This modification is due to the physical replacement of a conductive electrolyte by a dispersive element.

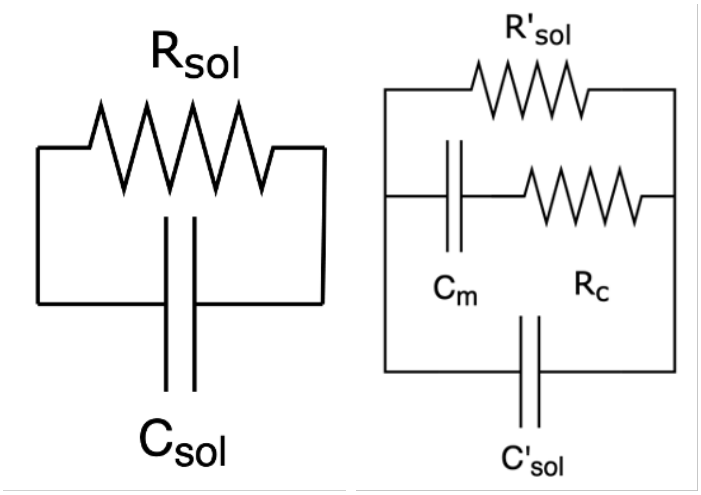

(a) **(b)**

Figure 1.17: (a) Equivalent Electrical Circuit of the medium without cells through a resistance R_{sol} and a capacitance C_{sol} and (b) Equivalent Electrical Circuit of the medium which initial resistance and capacitance potentially changed due to the presence of the cell R'_{sol} and C'_{sol}, together with the addition of two effects: the membrane capacitance C_m and a cytoplasmic resistance R_c.

Cell detection based on the interelectrode resistivity should be done at low frequencies (α or β dispersion). Considering the membrane capacitance acting as a barrier in low frequencies, adding a cell will be the equivalent of replacing the electrolyte conductive media with a dielectric sphere. Its impact on the overall impedance will therefore depend on its size and deformability. Indeed, if the γ dispersion is reached, the cytoplasm will be probed. However, its conductivity is close to that of the medium, hence its detection may be difficult.

The induced medium capacitance modification could also be used for cell detection. However, it needs to be contextualized with the medium in which the cells are in suspension. As discussed previously and shown on figure 1.17, electrolytic medium can be modeled by a resistance in parallel with a capacitance which also induces a cut-off frequency. This cut-off frequency is purely dependent on the medium properties and is not affected by the geometrical dimensions of the sensor.

For a non-dispersive media such as PBS, this cut-off frequency f_c can be calculated (Eq. 1.18) at $f_c = 360$MHz. However, for dispersive media such as whole blood, the cut-off frequency will be dependent on dielectric parameters, themselves dependent of the frequency. Its cut-off frequency is however reached when $\omega = 2\pi f_c(\omega)$ at 378MHz as shown on figure 1.18. Therefore, the sensor will see the resistive regime of the medium up to 360MHz for PBS and 378MHz for blood. The capacitive regime will then be attained above these cut-off frequencies.

As discussed previously, detection methods need to be within the α or β dispersion range, thus below 20MHz. The sensor will therefore be a resistive sensor for our detection application.

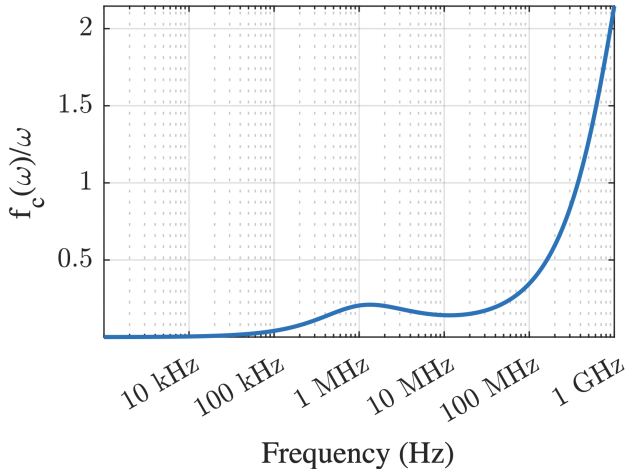

Figure 1.18: Representation of the cut-off frequency of blood attained for $\omega = 2\pi f_c(\omega)$, $\frac{2\pi f_c(\omega)}{\omega} = 1$.

Following the theory developed previously together with the vision of cell detection discussed in this section, a device with integrated electrodes on a filtering membrane for cell density detection will be presented in the chapter 2 of this manuscript.

1.5.5 Differentiation Principle

Previous sections described the concept of multishell cell modeling for interpreting the electrical dispersion and tying the electrical effects to biological properties: membrane folding, organelle density..., therefore demonstrating the potential of impedance spectroscopy for cell differentiation.

Indeed, based on the concept of cell detection, we aim at sensing the electrical dispersion of the trapped cell over a wide range of frequency. Following this acquisition, impedance data can then be interpreted, and cells electrically characterized through a multishell model.

However, measurement band broadening is far from trivial and require a precise optimization to lower the interfacial effects to the lowest frequency possible, at least below 250kHz to properly evaluate the β dispersion. On the other hand, increasing the measurement frequency implies that the sensor will be more sensitive to parasitic capacitances or inductances at high frequencies. Thus, a microfabricated device will be presented in chapter 3, and will be addressed these challenges through an optimization both of the sensing electrodes and the overall sensor structure.

Furthermore, spectroscopic impedance measurements depend on the exact position of the cell between the electrodes and its alignment with the pore, and therefore on the final conformation of the cell trapped within the gap and its possible adhesion to the surface. These mechanisms of cell confinement and/or adhesion to the support change the shape, which is no longer spherical, but also the composition of the

cytoskeleton and therefore affects the dielectric phenotype (see figure 1.8). From one capture event to the next, if the immobilization conformation of the cells is very different, the variation in dielectric constants will be such that small variations induced by the biological phenotype will be hidden, and it will therefore be impossible to distinguish the nature of the different trapped cells. Hence, the coupling with an optical characterization method is required to analyze capture events and see whether the trapping and positioning conformations on the membrane pores are reproducible. We will address this issue in chapter 3 through the development of a 3D printed chip to optically characterize the cell capture mechanism along electrical measurements.

1.5.6 FEM Simulations

With the aim to confirm the analytical description of equivalent circuit elements presented previously, FEM simulations were carried out using COMSOL Multiphysics software. These simulations will not be detailed for the sake of brevity, we will however describe along the manuscript how they were used and for what purpose together with the obtained results. The electrochemical effects at the interface in between the electrode and electrolyte were simulated in the literature by Zhang [58], we thus chose not to simulate this aspect due to its complexity together with the scales involved. Moreover, and as it will be discussed in upcoming chapters 2 and 3, the impact of these interfacial effects may vary from one design to the next, suggesting a dependence on sensor design and probing frequency which cannot be simulated. Design optimization of the double-layer effects were therefore done using analytical models fed with experimental data obtained on similar devices.

However, extensive simulations were carried to try and prevent capacitive interference along with the design of the sensor. Several points were tested such as capacitive coupling in between the connection tracks and the supporting structure. These simulations allowed a precise evaluation of these coupling by considering the fringe field effects and drove the choice of insulating materials and their thicknesses. The electrostatic interface of AC/DC COMSOL Module which was used for simulating capacitive effects relies on the computing of Gauss Theorem for the electric fields using the scalar electric potential as the dependent variable.

The sensor analytical modeling through a geometrical constant was confirmed by simulating the resistance of the sensing electrodes within electrolytic media with the Electric Current interface. This physics interface solves a current conservation equation based on Ohm's law. These simulations allowed to further evaluate the sensitivity of the sensor within an electrolytic media to the presence of cells and their impact on the global impedance through the equivalent electrical circuit model.

Finally, as discussed previously, the sensor combines multiple effects of different natures (resistive, capacitive) and at different scales: from the nanometer for the interfacial effects to the cm for capacitive coupling with the supporting structure.

Hence, simulating the whole structure at once would require fine meshing together with complex Multiphysics and large computing resources. Therefore, analytical models were favored through MATLAB computing, and simulations supplemented these models by simulating localized effects on simplified models.

1.6 Thesis Objectives

The work carried out within the framework of this thesis project is focused on the development of microfabricated devices that can provide information on the capture process and the captured biological elements in real time and within complex fluids. The targeted information is the detection of in situ cell capture on the filtering membrane and the differentiation of captured cell types through their electrical signature. Access to this information in real time would further document the knowledge surrounding the electrical properties of cells while enabling a precise calibration to be established, which will be necessary for the introduction of these devices into a clinical environment.

Real-time cell capture information is the first step towards the ultimate goal of the technology: real-time cell differentiation. This first step would provide information to avoid filter saturation and to adjust the capture time. Subsequently, the enumeration and identification of different cell types would provide useful clinical information for liquid biopsy applications. Access to this information in real time would eliminate the need for additional sample processing and analysis steps, thus facilitating its use in the clinical context.

The objectives of this research work are firstly to design and integrate microelectrodes on a microperforated membrane to enable real-time electrical detection of captured cells, and secondly to adapt the sensing system for the in-situ electrical differentiation of captured cells.

Chapter 1 presented the state of the art and the theory behind the principle of electrical cell detection and differentiation together with electrical modeling techniques.

Chapter 2 will describe the fabrication of a body fluid filtration device for electrical integrated in-situ detection of cell retention along with experimental characterization of these devices. equivalent electrical circuit model will be used to further interpret experimental results and demonstrate the capability of the devices to measure reliable electrical signals accounting for the membrane occupation by trapped cells within complex fluids such as whole blood.

Finally, chapter 3 of this manuscript presents the development of the first prototypes for in-situ analysis of captured cells for cell differentiation based on electrical dispersion measurements. To this end, two fabrication processes will be described and experimentally characterized. Moreover, their integration into an elaborate

experimental platform aims at providing multiple synchronous characterization ways: optical and electrical. The objective of this chapter is to answer two critical underlying questions for *in-situ* cell electrical analysis: (1) does the morphological differences induced by cell trapping are significant? and (2) could these differences mask smaller impedance variations induced by the dielectric phenotypes?

2 Fabrication of a Whole Blood Filtration Device with an *in-situ* Electrical Detection of Cell Retention

2.1 Integration of Electrodes on Filtering Devices for Cell Density Detection

The principle of in-situ electrical detection of biological elements is based on two essential technological elements: the electrosensitive element and the membrane that isolates the elements of interest from the biofluid. As these two aspects are closely related, their design and fabrication are discussed in the following sections.

2.1.1 General Structure of the Detection System

The detection device can be broken down into three sub-systems, each with its own functionality and interactions at the interfaces with the other neighboring subsystems. In a functional approach, the central element is the microperforated membrane with the functionality of filtering the elements of interest and supporting the microelectrodes representing the second subsystem. The purpose of the electrodes is to detect cell density at the surface of the filter. It will therefore interact with the filtering membrane, which is its support, the detection area upstream of the electrodes, which represents the sensitive area of the sensor, and electrically with the structure, the third subsystem. The structure enables the thin membrane to be held in place and handled by giving it mechanical strength.

Figure 2.1 shows the overall device's shape and dimensions. The filtering membrane is placed in its center and is surrounded by fluidic slits. The electrode's contacts are placed on each squared side of the main structure and are accessible on its back side. The normal or "forward" fluid direction which will be used for sample processing in upcoming experiments is shown on the same figure.

The shape of the microdevice is given by the Nickel structure that supports the filtering membrane. The structure is 150 µm thick and has an imprint of 4.4 mm by 6.8

mm. It exhibits circular 200 µm wide fluidic slits surrounding the filtering membrane. These slits allow for a partial filtration of the sample: the flow is distributed through both the surrounding slits and the microperforated membrane, allowing releasing the pressure of the filtering membrane and therefore achieving larger flow rate for sample processing while reducing mechanical stress on captured cells through by limiting the transmembrane pressure. The filtering membrane is centered within the nickel supporting structure and is covering a circular surface of 570 µm radius, displaying 2000 circular pores of 10 µm diameter each, following a staggered distribution with 8 µm and 16 µm spacing respectively vertically and horizontally in between each pore. The electrodes on these devices are interdigitated (IDE) and are composed of two main electrodes with different numbers of parallel fingers. Different electrode designs were considered. Hence, depending on the device, the electrode fingers surround either 60 pores, 1000 pores or 2000 pores of the membrane, thus providing respectively 2, 34 and 86 fingers or also called single coverage, partial coverage or full coverage of the microperforated membrane. The length of each finger varies since the membrane is circular. Each electrode is connected through a 2mm-long track to a contact pad enabling electrical contact and characterization with an external equipment from the device's backside.

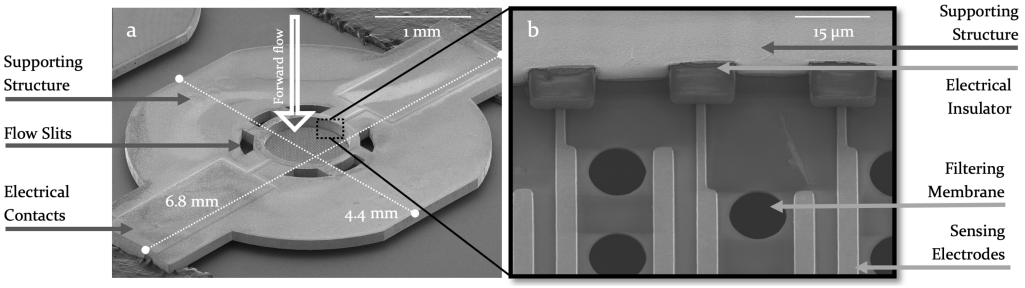

Figure 2.1: Scanning Electron Micrographs of the Cellular Capture and Detection Device. The whole sensing device is shown in (a). (b) is a close-up of the filtering membrane in the central part of the device.

2.1.2 Electrode Geometries

Four electrode geometries were considered: interdigitated electrodes with 3 varying shapes and a hybrid design. The main objective guiding the choice of these geometries is to achieve a homogeneous distribution of the electromagnetic field over the membrane while limiting the number of connection points required for measurement, thereby simplifying integration. A typical example of interdigitated geometry is shown in figure 2.2. The principle consists of connecting several parallel electrodes (called "fingers") by a perpendicular backbone, thus forming an electrode with multiple fingers. The counter-electrode is formed symmetrically with respect to the first and is interleaved so that each electrode finger alternates. Due to this geometry, addressing these electrodes requires only a single contact pad connected to each electrode backbone through access tracks.

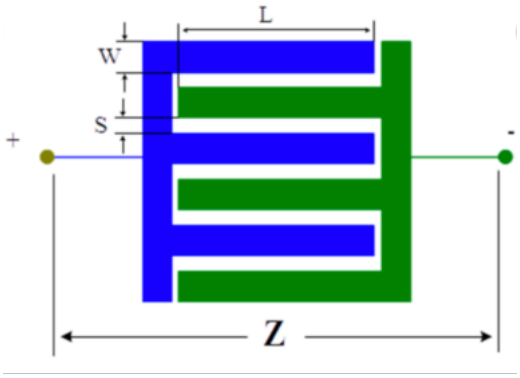

Figure 2.2: Schematic diagram of a pair of interdigitated electrodes, each with 3 fingers of length L, width W and spacing S [49].

In each electrode design shown below, the contact pad is deported at the extremity of the structure to facilitate the electrical integration. As it can be seen on the figure 2.3, lines connecting the contact pads to each sides of the interdigitated electrodes gradually increase in width to reach the width of the pad, in order to limit 90° angles that can lead to line weakness and potential breaks. However, this triangular shape brings a constraint in terms of parasitic capacitance: by increasing the surface area of the lines through their widening, capacitive effect in between the electrode and the nickel structure is increased. Simulations were therefore carried out to adapt the choice and thickness of the insulator (see chapter 1). The triangular feeder line has a length of approximately 2 mm and a final width matching the contact pad dimensions: 1 mm by 780 µm. These dimensions match the tip of small spring loaded pogo pins that will be used to make electrical contacts.

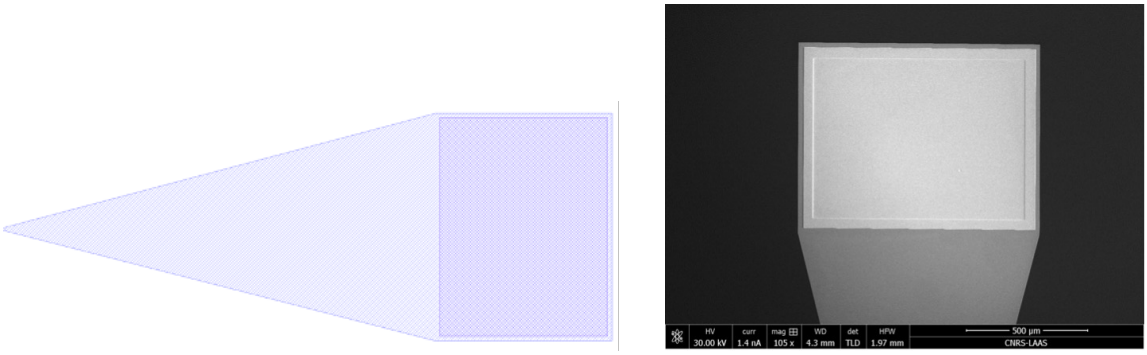

(a) **(b)**

Figure 2.3: (a) Screenshot of the KLayout software showing the design of two masks: a first used to define the electrode access tracks and a second one used for the electrolytic growth of a thick gold layer on top of the access tracks. A triangular access track is used to link the electrodes to deported contact pads to avoid large angles. (b) SEM Micrograph (planar view) exhibiting the triangular connection tracks and the electroplated square via on top of it.

Finally, we chose to explore three different shapes of interdigital electrodes: concentric, rectangular and fractal. It should be noted that, since the structure

surrounding the membrane is circular, the electrode designs will therefore follow this boundary, which means that each design will have a rounded component at its outer boundary. Discussion of the analytical modeling of such elements is presented in upcoming sections. In addition, based on the knowledge of SmartCatch company of cell filtration, the choice was made to use pores with a diameter of 10 µm for the filter membrane, thus setting the minimum space between two detection electrodes surrounding a pore at 14 µm.

Rectangular Design

Rectangular interdigital electrodes are the most common in the literature. They have been used in a variety of applications at the interface with biology, including the detection of sedimentation of various biological elements: blood cells, yeast, bacteria, tumor cells, etc., as well as real-time evaluation of their propagation under culture conditions [49, 59, 60]. More generally, the design is relatively easy to manufacture using standard clean-room microfabrication techniques. In addition, analytical models representing the distribution of the electromagnetic field have been developed, enabling accelerated design while reducing the simulation load [52, 61].

Two rectangular electrode designs are shown in figure 2.4. The first design consists of 16 fingers with a width of 21 µm and a spacing of 14µm. This shows the arrangement of a single line of pores between each pair, with a total of 1,390 pores. The second design has 9 fingers, 29 µm wide and 29 µm apart. This arrangement makes it possible to include two lines of pores between each electrode, increasing the number of pores to 1624.

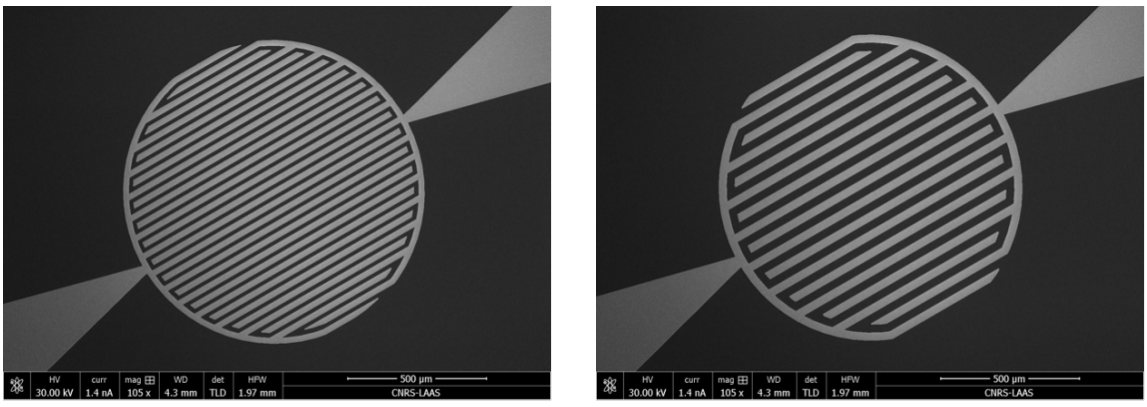

(a) **(b)**

Figure 2.4: SEM micrographs of the fabricated rectangular electrodes designs with (a) 14 µm electrode spacing and (b) 29 µm electrode spacing.

Concentric Design

Concentric electrodes, traditionally used in high-frequency applications to generate resonators, also enable a homogeneous distribution of the electromagnetic field at low frequencies. In the same way as above, one of the circles is connected to a single contact pad forming a first electrode, the remaining circles are also connected to form the second electrode. In this way, the impedance of the system is modeled using a form factor, so the equation is virtually identical to rectangular electrodes. Indeed, with some adaptation to the radial symmetry of the system, the concentric electrodes can easily be modeled as rectangular electrodes. However, the variation in length from one electrode to the next must be taken into account by approximating the average finger length.

Two concentric electrode designs are shown in figure 2.5. The first design consists of 8 fingers with a width of 21 µm and a spacing of 14 µm. This shows the arrangement of a single line of pores between each pair, with a total of 1258 pores. The second design has 5 fingers, 29 µm wide and 29 µm apart. This arrangement makes it possible to include two lines of pores between each electrode, increasing the number of pores to 1588.

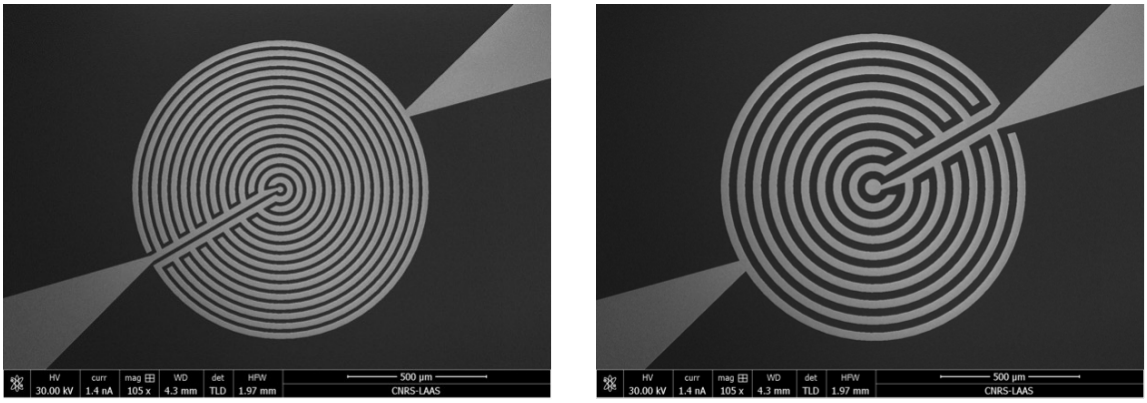

(a) **(b)**

Figure 2.5: SEM micrographs of the fabricated concentric electrodes designs with (a) 14 µm electrode spacing and (b) 29 µm electrode spacing.

Fractal Design

Electrodes based on a fractal design have also been explored. Inspired by electrode designs for super-capacitors, these arrangements maximize capacitive effect [62]. Following the example of these applications, but with a view to resistive detection, the manufacture of this device aims both to increase the number of pores available (1882) and to improve detection sensitivity by means of an entanglement between the sensitive elements and the pores of the membrane.

The fractal electrode design is shown in figure 2.6. The branches of the electrode are inspired by a Koch pattern developed at the very first stage of growth (pre-fractal shape), the formation of which is described by the figure 2.7. A single pattern is called a Koch Island and is repeated until it forms one of the fingers of the interdigitated electrode. The counter-electrode is then formed as a negative of the first, with an enlargement of the empty zones to leave the necessary space for the pores of the membrane. The smallest dimension of the design is the width of the red electrode strands, which measure 4 µm. The spacing between the two electrodes is constant at 14 µm. Due to technological limitations, the fractal pattern is not fully developed in the geometrical sense, and the electrodes are therefore only inspired from a fractal design. However, for ease of reading, this electrode design will be referred to as the fractal design in the upcoming sections.

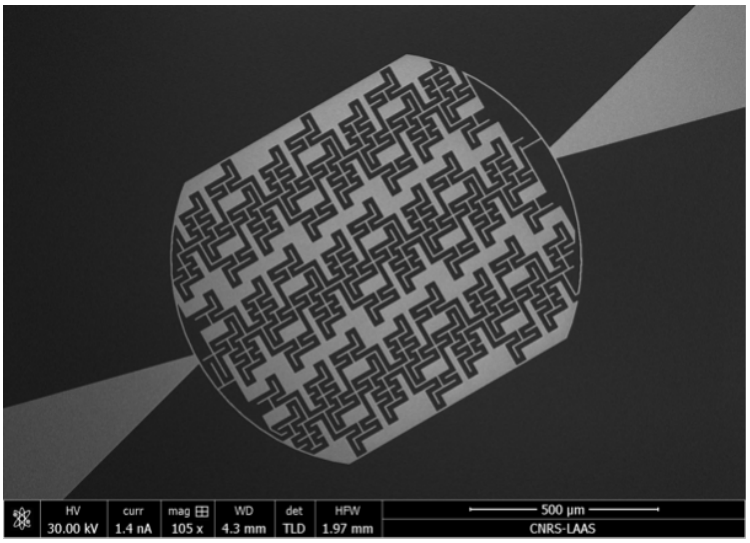

Figure 2.6: SEM micrograph of the fabricated fractal electrodes design.

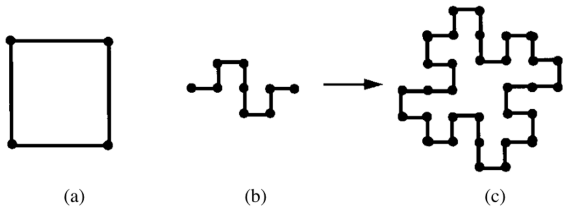

Figure 2.7: Construction of a Koch curve. (a) An initiator, (b) a generator, and (c) the first step of the process which consists of the replacement of each segment composing (a) by the generator (b) [62].

Hybrid Design

Unlike the conventional interdigitated electrodes shown in figure 2.2, where the dimensions are constant from one pair to the next (W, S and L), we propose here a design with various inter-electrodes spacing S. Thus, the fingers are 4 µm wide with a spacing varying between 14 µm and 4 µm. This variation in spacing is visible in figure 2.8 and aims to make the sensor sensitive both in the filtration zones, where the membrane is perforated (14 µm spacing) and also where it is not (4 µm spacing). This second detection zone, although devoid of filtration pores, would make it possible to increase the sensitivity of the sensor by bringing the detection electrodes closer and thus evaluate the effects of adsorption of biological elements (cells, proteins) on the membrane. In order to evaluate the correlation between electrode surface and electrical detection sensitivity, this hybrid design is derived in three different coverage: figure 2.8 shows the full coverage of the membrane by the electrodes, a second design covers only half of the membrane (see figure 2.27) and a third of only a single pore line.

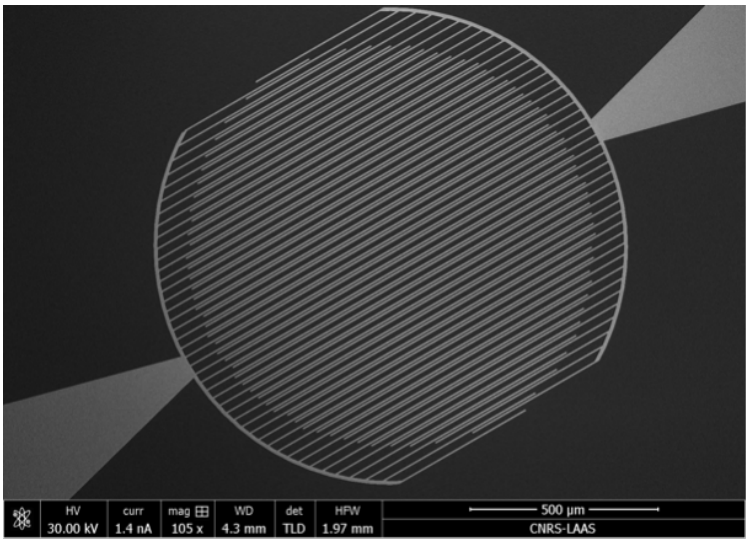

Figure 2.8: SEM micrograph of the fabricated hybrid electrodes design.

2.2 Micro-fabrication Process

The fabrication process reported here was first developed by E. Bou [63] during her PhD in 2020. Designs were then modified to fit the electrical requirements of the present work, and the process was optimized to achieve a higher fabrication yield. The main modifications from the original fabrication process are the change in insulating materials (from polymers to ceramics) which were inducing mechanical stress on breaking tracks when heated together with the use of plasma etching to define the electrodes instead of a classical liftoff process. Designs modifications also improved the fabrication process, such as the introduction of triangular shaped connection tracks making them less brittle.

2.2.1 Choice of Materials

Supporting Structure

Based on our experience of previous filters developments at SmartCatch company, we decided to keep the support part of the membrane in electrolytic nickel. We thought that this gave the filters a mechanical strength that allowed them to be handled easily with pliers without damaging them. This 150 µm thick support section protects the filter membrane, which is not in contact with the operator's tools. Nickel is a conductive metal (conductivity $\sigma = 1.47x10^7$ S/m), so it must be sufficiently insulated from connection tracks and electrical contact pads to avoid short circuits and capacitive interference with the measurement. However, nickel is recognized as a cytotoxic material [64] and technological developments will be needed if long-term biological exposition is considered.

Filtering Membrane

The first requirement is to choose an insulating material to form the filter membrane. This means choosing a dielectric material with a low permittivity so as not to generate large capacitances that may impact the value of the capacitance between microelectrodes printed on its surface. It must also have a low loss factor to mitigate current leakage. The surface of the chosen material must be flat (uniform and without roughness) to obtain sufficient resolution for the photolithography stage defining the microelectrodes and the connection tracks, which are the critical dimensions of our design. Finally, the material chosen must be strong enough to perform its filtering function under hydrodynamic flow. The material must be as unstressed as possible to support the layer of metal on its surface, forming the microelectrodes. Based on these prerequisites, we identified a bilayer of 800 nm silicon oxide (SiO_2) and 600 nm silicon nitride (SiN_x) as a potential candidate to meet our requirements. This SiO_2/SiN_x

bilayer was previously developed at LAAS-CNRS for the fabrication of gas sensors. It has been developed to have a low residual stress, giving it enhanced mechanical properties in terms of stability and resistance to stress. The bilayer developed also has the advantage of high surface uniformity. The total thickness of the layer is 1.4 µm. These materials, which are widely used as insulators in microelectronics, have dielectric properties that are compatible with their use as substrates for integrating electrodes. With low permittivity and loss factor values, they help to minimize the capacitance induced in the integrated microelectrode substrate, which is the filter membrane, and prevent current leakage.

Microelectrodes

With regard to the metal used for manufacturing the microelectrodes, we chose gold because of its high stability against reaction with other materials, resulting for example in low oxidation in the open air or in the presence of a liquid medium, and its resistance to corrosion. It is also a metal with good conductive properties ($\sigma = 4.25x10^7$ S/m). This metal is already used in the development of a variety of implantable biosensors and is widely recognized as one of the most biologically compatible metals (non-cytotoxic) [65, 66]. A thickness of 150 nm was chosen to avoid reactor pollution with thicker layers during plasma etching steps. However, this thickness lowers the volume of interaction between the electric field generated by the coplanar electrodes and the captured elements, thereby increasing the impedance of the system

Insulating layer

Finally, the material chosen to insulate the connection tracks and contact pads of the nickel membrane is a silicon nitride layer (SiN_x). Ceramics are generally good electrical insulators, moreover, and unlike silicon dioxide (SiO_2), SiN_x is resistant to corrosive environment such as water and sodium which are present in physiological buffers. A layer of 1 µm is deposited through chemical vapor deposition (CVD) techniques, however, to avoid the diffusion of gold in silicon due to the high temperature of the Low-Pressure CVD process (750°C), a Plasma Enhanced CVD process is applied, thus limiting the temperature to 300°C. This deposition process creates a uniform and conformal layer which is accurately controlled in thickness.

2.2.2 Micro-Fabrication Techniques

The devices are structured using a micro-fabrication process comprising 18 steps, including 6 photolithography levels. Photolithography consists of all the operations involved in the patterning of a photosensitive resist at the surface of a substrate. The photosensitive resist is deposited on the surface of a substrate in the form of a film of controlled thickness. The resist is then exposed to UV light radiation through a mask made up of opaque and transparent areas to define the pattern to be reproduced on the substrate. Depending on the polarity of the resist (positive or negative), the exposed or unexposed areas are revealed in a chemical bath, forming a designed structured mold on the surface of the wafer. Photolithography is a common technique which is usually followed by design transfer techniques. For the fabrication of devices with integrated electrodes, the techniques used for design include two chemical vapor deposition steps, two physical vapor deposition steps, five dry etching steps, two electrochemical steps and a wet chemical etching step. In the rest of this section, we will describe the operating principle of the main techniques used. Figure 2.14 shows a schematic diagram of these different techniques.

CVD Deposition to Form the Filter Membrane

The SiO_2/SiN_x bilayer is formed on both sides of the silicon substrate. This bilayer will be released at the end of the process (see figure 2.14) which remains a critical step of the fabrication. If this bilayer is excessively mechanically stressed, either by some built-in stress during the deposition process or due to thermal dilatation coefficient mismatch with the supporting substrate, the relaxation of the residual stress during final release can cause a severe membrane deformation out of its plane which may break the supporting electrodes or generate the propagation of cracks between the pores or even disrupt the membrane. The additive technique used to deposit the silicon nitride layer while mitigating stress formation is inspired from MEMS technology and is a chemical vapor deposition (CVD). This technique is carried out at high temperature in the presence of a gaseous phase whose constituents react with the substrate to form a solid film. Initially, a 0.8 µm layer of SiO_2 is formed by thermal oxidation of the silicon substrate in an oven at a temperature of 1070°C. Next, a 0.6 µm layer of SiN_x is deposited at low pressure by LPCVD (Low Pressure Chemical Vapor Deposition), this technique increases the uniformity of the films deposited on the substrates. The SiN_x film is formed at 750°C by the reaction of SiH_4 and NH_3 gases on the substrate. The silicon substrate therefore has a SiO_2/SiN_x bilayer formed prior to the structuring steps carried out by the techniques described below. The SiN_x deposit is not stoichiometric nitride (Si_3N_4). It should be noted that it is the adjustment of the LPCVD process parameters that makes it possible to regulate the nitride content. With the deposition conditions used, the x parameter is 1.15. However, the deposit is highly reproducible, and the same nitride content will be obtained from one run to the next. This deposit

was developed because as-deposited stoichiometric Si_3N_4 thin films exhibits a high residual stress, and the deposit is therefore limited in thickness (120 nm). We chose parameters already established at the LAAS technology center for various MEMS processes, minimizing the residual stress within the SiO_2/SiN_x bilayer that will be released from its support at the end of the technological process.

Physical Vapor Deposition

The Physical Vapor Deposition (PVD) is a physical process for depositing thin layers of metal under high vacuum (see figure 2.9). In our case, it involves thermal evaporation by heating a metal crucible of high purity using electron beam bombardment. The evaporated metal atoms then condense into a solid-state thin film on the surface of the substrate through a process of nucleation and growth, resulting at room temperature in a polycrystalline thin film. A first layer of 50 nm of chromium is deposited to reinforce the interfacial adhesiveness with the substrate. A 100 nm thick layer of gold is then deposited on top. Thus, the 150 nm thick layer comprises 50 nm of chromium and 100 nm of gold. This bilayer will constitute the microelectrodes of the device (see figure 2.14).

Figure 2.9: Deposition chamber of the EVA 600 PVD machine. The crucible is placed in the lower part whereas the wafers are placed on the top half dome. The whole chamber is put under vacuum during the process.

RIE Plasma Etching

The dry etching steps performed are of the reactive ion etching (RIE) type, a subtractive technique is implemented using a plasma which combines physical sputtering by ionic bombardment and chemical reaction with the surface material to be etched. A photolithography step is carried out beforehand to structure a photosensitive resist layer with apertures in the areas of the pattern to be etched. Due to the physical component of the etching process, this type of etching is anisotropic, meaning that the material is etched with quasi-vertical edges due to the acceleration of the plasma generated ions normal to the substrate surface. The chemical reactions taking place simultaneously between surface atoms and neutral radicals generated inside the plasma, create volatile surface species that are easily sputtered by ion bombardment (decrease of the surface binding energy). In this process the correct balance between physical etching and chemical etching needs to be adjusted for generating vertical edges (physical component) and high etching rates (chemical component). The type (nature of atoms) and quantity of gas (residual pressure inside the chamber) used to generate the plasma depends on the material to be etched and enables the adjustment of the chemical component of the etching.

In our case, we use an ICP reactor (Inductive Coupled Plasma) shown in figure 2.10. In this system, the plasma is generated by a powerful radio-frequency magnetic field. This type of reactor allows us to obtain a high density of ions in the plasma, and to control the energy of the ions reacting with the substrate using another polarized radio frequency source. The adjustment of the power of the plasma generator and the polarizing element enables the control of the physical component of the etching through the adjustment of the ion incoming energy.

The photosensitive resist protecting the areas that are not etched is also eroded by the plasma. The etching selectivity of the process is defined by the ratio between the etching rates of the material to be etched and of the resist layer. The selectivity of 1/10 for example indicates that under ICP RIE etching, the resist layer is etched at a speed ten times lower compared to the material to be etched. The etching rate refers as the amount of thickness of any material eroded by a unit of time during the process, a typical unit is nm/s. The knowledge of the selectivity of the etching process and the targeted etching depth makes possible the anticipation of the adequate resist thickness to be used to protect the un-etched regions completely during the whole process. In our case, we use "ECI resist" with the following selectivity values for the process used in this work for etching the SiO_2/SiN_x bilayer: $V_{SiNx}/V_{ECI} = 0.6$ and $V_{SiO2}/V_{ECI} = 0.7$. It is also important to know the etching selectivity with the material supporting the one to be etched, so as not to damage it if it must be kept for the rest of the microfabrication process.

Although the etching rates for each material are defined by calibration experiments, when producing designs for a complex device such as ours, the etching time generally requires an optimization step. The surface to be etched and the layout of the patterns,

for example, also influence the etching rate. Three recipes are used throughout the five dry etching steps: a first one to etch the bilayer membrane (SiO_2/SiN_x), a second one to define the electrodes (Cr/Au) and a last one to define the electrical insulator (SiN_x).

The bilayer membrane (SiO_2/SiN_x) plasma etching uses trifluoromethane (CHF_3, 20 cm^3/min) and argon (Ar, 50 cm^3/min) to etch 0.6 µm silicon nitride and 0.8 µm silicon dioxide successively. We use ECI photoresist with a thickness of 2.4 µm. The plasma etching takes 10 minutes at a sample temperature of 15°C and with a RF power of 90 W to generate the plasma and an ICP power of 300 W with a reactor residual pressure of 7,1 mT.

Definition of the Cr/Au electrodes (50 nm/100 nm) is done with argon (Ar, 30 cm^3/min) at a sample temperature of 20°C for 3 minutes with a RF power of 100 W and an ICP power of 600 W with a reactor residual pressure of 0,67 mT. In that specific case, there is no chemical component in the etching process as Ar atoms are totally inert with respect to the surface material.

Finally, etching of the electrical insulator (SiN_x) uses trifluoromethane (CHF_3, 20 cm^3/min), nitrogen (N2, 10 cm^3/min), argon (Ar, 100 cm^3/min) and dioxygen (O2, 10 cm^3/min). The process step takes 8 min for etching 1 µm at a temperature of 20°C and with a RF power of 35 W and ICP power of 300 W with a reactor residual pressure of 25 mT.

Every etching step is followed by a Laser Endpoint Detection system which working principle is based on laser interferometry shown on figure 2.10. Indeed, the change in layer thickness together with interaction through multiple layers creates interferences and therefore modulates the intensity of the reflected signal as shown on figure 2.11 were the typical curves for the three recipes described above are shown. We can see that the two silicon-based etchings create oscillating patterns which can be further used for etching depth evaluation. However, in our case, the stopping layer is different from the one being etched which therefore creates a recognizable signal behavior, allowing the operator to manually stop the etching process. Indeed, the three etchings steps finish on the silicon substrate, which is not etched by the generated plasma, therefore inducing a signal of a stable intensity which derivative reaches 0.

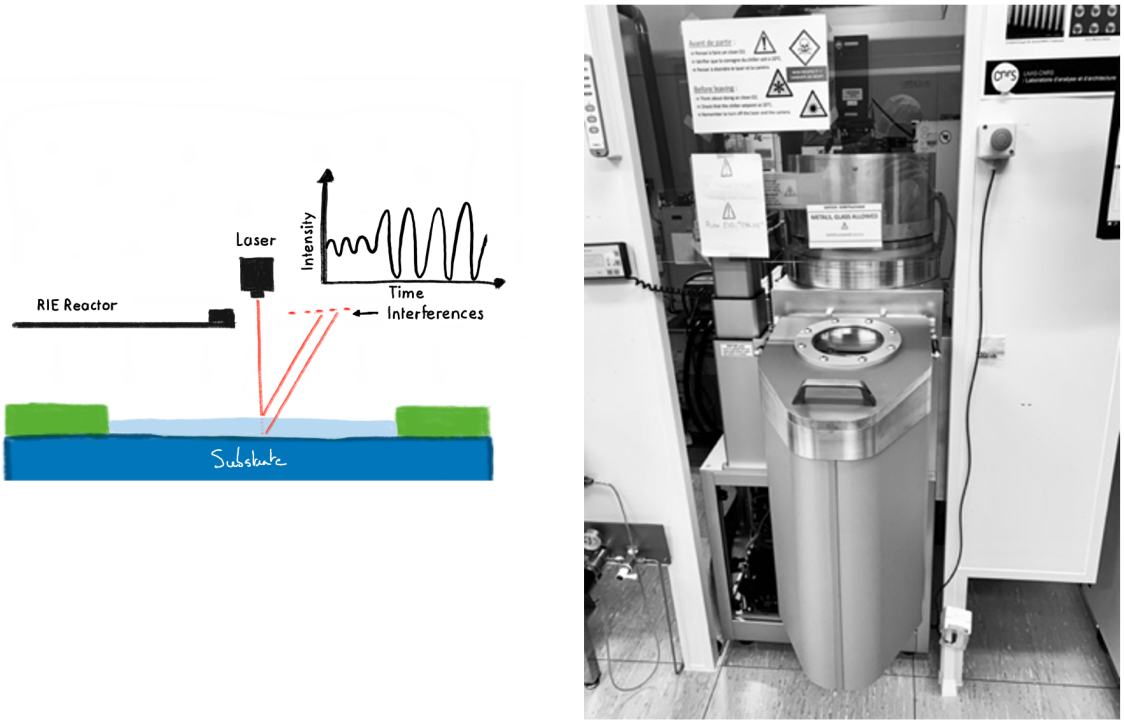

(a) **(b)**

Figure 2.10: (a) Working principle of the Laser Endpoint Detection System allowing live tracking of etching rates and exposed layers. (b) SENTECH SI-500 plasma etching machine. At the front, the load lock with the handle allows the loading of a single wafer at a time. A robotic arm then moves the wafer in and out of the reactor chamber (the cylindrical part). A small viewport on the top of the reactor allows for the use of a Laser Endpoint Detection System (here on top of the cylinder). The temperature of the wafer is controlled during the etching process through a dedicated chiller standing in the back, cooling the sample down to -20°C.

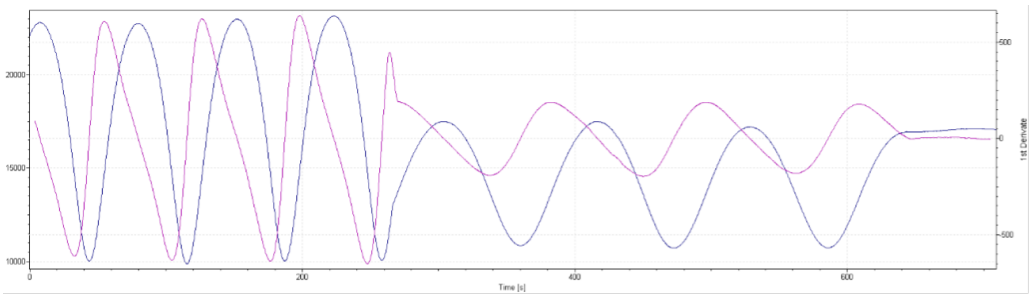

(a)

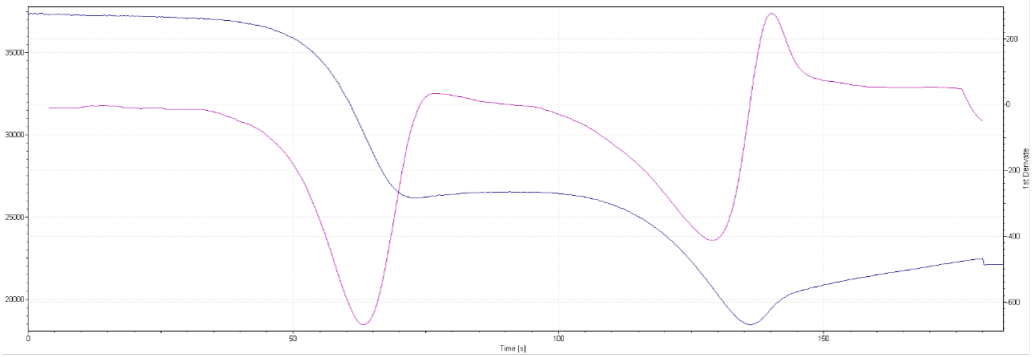

(b)

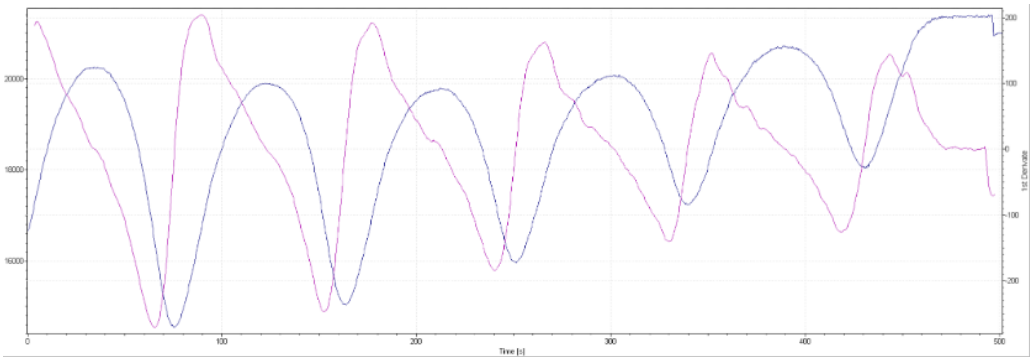

(c)

Figure 2.11: Typical Laser Endpoint Detection Curve obtained while etching (a) SiO_2/SiN_x bilayer, (b) Cr/Au and (c) SiN_x . The blue line shows the intensity of the laser reflection which is modulated by the interference generated by the different layers. Pink link is the first derivative of the blue line. In this example of the bilayer membrane (a), first, SiO_2 is represented by the 4 large oscillations and was etched in 260s, SiN_x exhibits 3 oscillations and was etched in 340s. Finally, silicon is not etched by the current plasma; thus, it does not exhibit oscillations and is detectable through a stable signal. On the other hand, Cr/Au is not oscillating and is etched through two recognizable steps in 150s.

Electroplating

Electrolytic growth is an additive technique involving the growth of a metal film on the surface of a conductive substrate immersed in a conductive ion bath called electrolyte. A metalization step carried out beforehand on the entire wafer produces a metal layer called the seed layer or growth base required for electrolytic growth when the surface to be metalized is insulating. After a photolithography step, metal growth takes place only in the regions where the electrolyte interacts with the conductive seed layer, i.e. in the opened areas of the structured resist layer. The structured resist layer thus acts as a mold for the metal growth over the surface (see figure 2.13). Electrolytic growth enables thick layers to be obtained (as thick as the resist layer), and if the substrate has topographical reliefs, metalization takes place on all the faces in contact with the electrolyte. This last advantage is essential to form electrical connections across a substrate, known as "vias". An anode is immersed in the electrolyte, while the conductive substrate acts as a cathode, attracting metal cations to the conductive regions not protected by resist, after reduction on the surface, the metal atoms form a polycrystalline film by nucleation and growth processes. The growth rate (thickness of the film as a function of time) depends on the current density (A/m^2) and the valence of the ions in the electrolyte. It also depends on the chemistry of the electrolytic bath used and, to a lesser extent, the equipment. The current density impacts the quality of the deposit in terms of roughness, stresses within the deposit and resistivity of the deposited material because it affects the growth mechanism at the surface and therefore the polycrystallinity of the material. In our case, this technique is used to form the robust supporting structure of the devices consisting of a thickness of 150 µm of nickel (see figure 2.14). It is deposited from a nickel sulfamate-based electrolyte using YAMAMOTO equipment (see figure 2.12) with a current density of 40 mA/m^2 for 215 min. This technique is also used for the formation of connection vias linking the front-side connection tracks of the devices to the rear-side contact pads. In this case, 1 µm of gold is deposited from a sulfite-based gold bath at a current density of 2 mA/m^2 for 8 min.

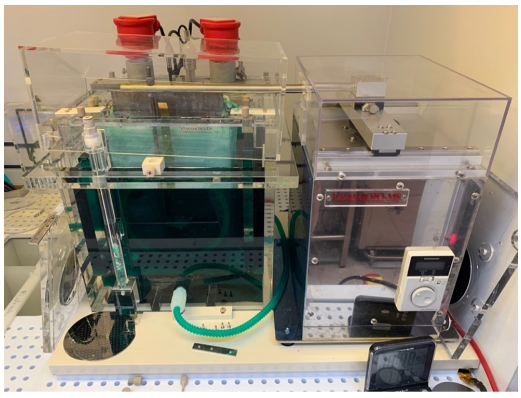

Figure 2.12: Electrolytic bath used for nickel growth (YAMAMOTO MS) on the left side. The right part of the machine is a robotic arm used for solution mixing next to the growth area.

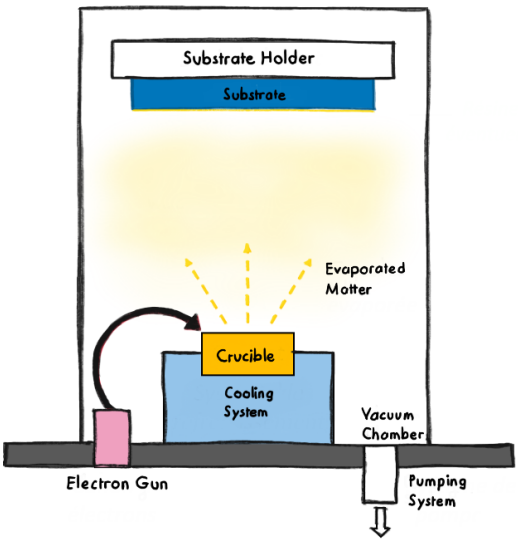

(a) Physical Vapor Deposition (PVD)

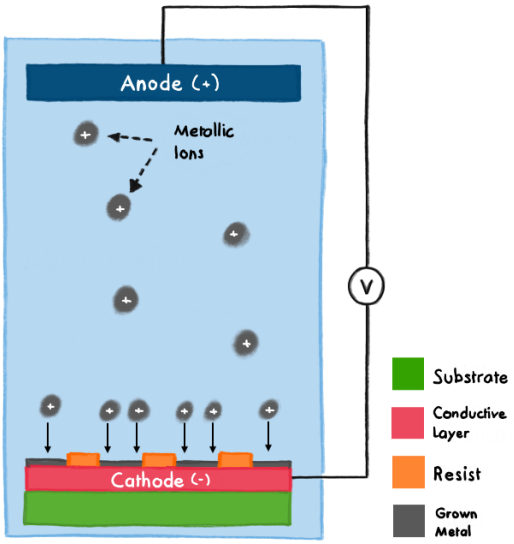

(b) Electroplating

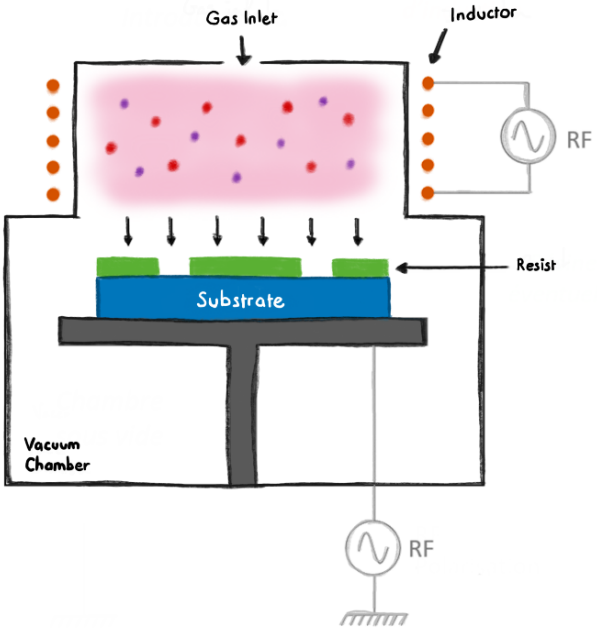

(c) Inductive Coupled Plasma Reactive Ion Etching (ICP RIE)

Figure 2.13: Schematic representations of the different techniques of pattern transfer used in this work. PVD and Electroplating are additive transfer methods, they form a film at the surface while ICP Ion etching is a subtractive technology resulting in surface material etching. PVD and IC-RIE are performed under vacuum, electroplating is performed in an electrolytic bath.

2.2.3 Micro-Fabrication Process

The design is optimized to maximize the number of devices produced from a wafer. The current design comprises 310 devices dispatched on a 4-inch Si (001) wafer. Six mask levels have been designed using Klayout software. The first level (L1) corresponds to the opening of the connection pads on the back of the devices. The electrolytic growth of the second layer (L2) constitutes the vias between the electrical contact pads on the rear face of the devices and the connection tracks and microelectrodes on the front face. The microelectrodes, connection tracks and electrical contact pads are defined on the same third level (L3). The insulation of the connection tracks and contact pads is defined on the fourth level (L4). A fifth level (L5) corresponds to the pores of the filtering membrane centered between the pairs of microelectrodes previously defined and to the lateral openings. Finally, a sixth and last level (L6) forms the nickel support part. It should be noted that the alignment between levels L3 and L5 is particularly critical, as the openings in the filter membrane must be structured in the center of the microelectrodes, with 2 µm between the ends of the openings and the microelectrodes. Each structuring level, corresponding to the six mask levels presented above, requires a photolithography step followed by a pattern transfer technique. The various pattern transfer techniques presented in the previous section are used. Figure 2.14 summarizes the successive steps in the fabrication process, details of which are given in the Appendix.

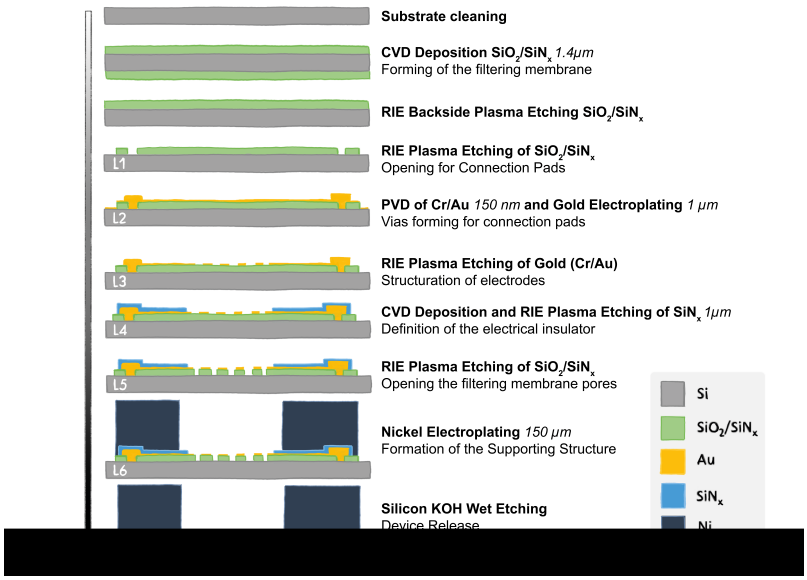

Figure 2.14: Schematic representation of the different steps of the microfabrication process for devices with integrated electrodes. Diagrams are not to scale. The electrolytic deposition of nickel is conformal, i.e. it follows the topography of the substrate on which it is deposited; this feature is not shown in the diagram.

2.2.4 Characterization of the Fabrication Process

The microfabrication process is characterized at each step using mechanical profilometry, optical microscopy, interferometric microscopy, and/or scanning electron microscopy (SEM). The purpose of characterization is to ensure that the structure dimensions meet the design requirement and to verify the surface condition and adhesion among the various layers. The critical steps are closely followed using multiple characterization methods.

Although the CVD deposition process forming the membrane is very reproducible, the thickness of the bilayer is checked at every deposition (usually made in a large batch of 25 wafers) using an ellipsometer.

RIE etching steps are monitored within the controlled environment of the etching reactor, thus exhibiting very little variation from one sample to another. Moreover, the etching process is followed by Laser Endpoint Detection, thus allowing for estimating the thickness etched through interferometric intensity measurement, but also detecting a difference in reflective index in between layers when stopping on another material (for example etching SiO_2/SiN_x and stopping on Si as presented on figure 2.11). This step is controlled post etching using an optical profilometer to evaluate the etched profile and verify that the layer is completely etched through. We can see on figure 2.15, which was measured after the etching of the SiO_2/SiN_x bilayer, that the pores are going through the 1.4µm thick membrane and have a diameter of 10µm.

The electrode definition process is performed by plasma etching. Conventional gold dry etching processes uses chlorine gas. It, however, interacts with the resists, making it harder to remove afterwards. Moreover, the solvent used to remove this resist is commercially labeled NF52 and is a powerful resist stripper containing Tetramethylammonium hydroxide (TMAH) which also etches gold at a lower rate. Letting the wafer longer in this strong solvent was not an option and we thus developed a fully "physical" etching recipe with a neutral gas (Argon). However, this recipe induces gold sputtering in the plasma reactor and redeposition on top and on the sides of the resist. As such, resist development can create so-called flags of gold which stays attached to the wafer and re-depose on the wafer through adsorption as shown on figure 2.16. It is therefore essential to perform resist development in an ultrasonic bath with the wafer upside down so that the golden flags, broken by ultrasounds, do not deposit on the wafer.

Electroplating steps are followed by both a profilometer inspection to characterize the thickness and homogeneity of the growth but also a SEM inspection to evaluate its quality. As it can be seen on figure 2.17, the thickness of the nickel layer forming the supporting structure is ranging from 139µm to 173µm. This inhomogeneity is normal and inevitable when dealing with multiple pattern size: indeed, a smaller usually leads to a faster growth. There is also inhomogeneity at the scale of the wafer which is considered during design steps: keeping a homogeneous distribution of

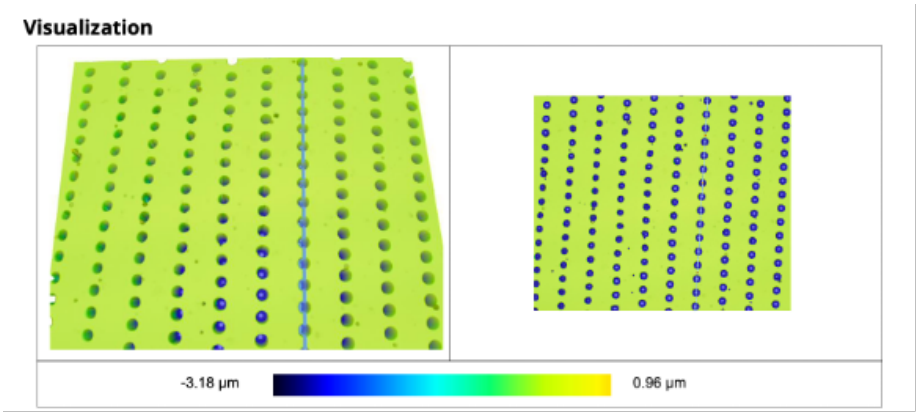

(a)

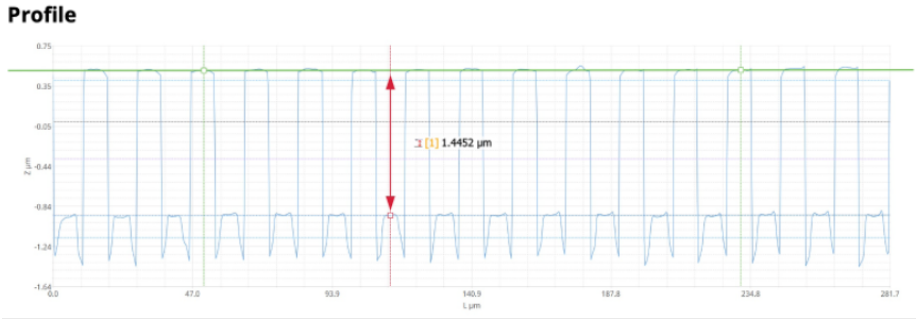

(b)

Figure 2.15: Imaging with an interferometric microscope (SNEOX, Sensofar) of the etched membrane. The membrane has a thickness of 1.4µm and is composed of an optically transparent bilayer (SiO_2/SiN_x). However, interferometric imaging allows use to precisely evaluate the thickness of this layer thanks to the difference in refractive index with the silicon.

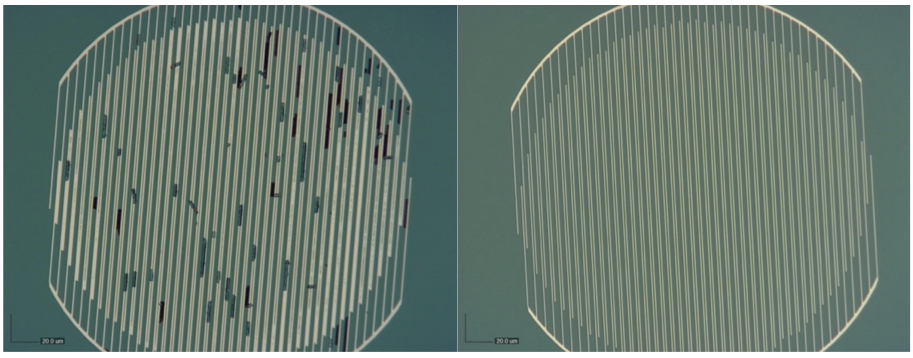

Figure 2.16: Optical Microscopy images of one device after the liftoff process: on the left without ultrasounds and on the right with ultrasounds. Adsorbed flags on the left image cannot be cleaned through conventional rinsing (DI water, ethanol, acetone) nor with O2/Ar Plasma.

designs, especially at the edge of the wafer helps to mitigate the inhomogeneity. As it will be discussed during the electrical characterization, the yield of this fabrication process is around 30% of electrically functional devices, which translates to 30 devices total, 5 devices per design. This poor yield is mainly due to the last process step, the KOH wet etching which probably weakens the thin filtering membranes while, once released, letting the device float in solution and collide with each other. It is important to stress this yield since it also impacted the subsequent characterization steps.

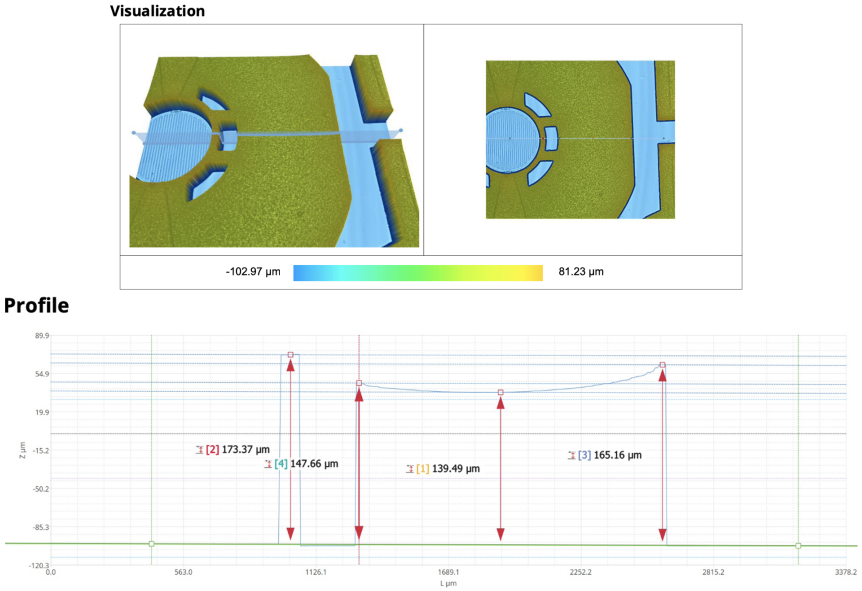

Figure 2.17: Imaging with an interferometric microscope (SNEOX, Sensofar) of electrolytic growth of nickel. The thickness of the layer is varying from 139µm to 173µm. The inhomogeneity is correlated to the difference in pattern size: smaller patterns turned out to grow faster than larger patterns.

Finally, after the last process step, which consists of the release of the devices from their substrate through silicon wet etching, a global inspection of a few devices of each design is done using SEM imaging for a global inspection (see figure 2.18), checking for the integrity of the structure, membrane and continuity of the electrodes. The full electrical characterization of devices is discussed in upcoming sections.

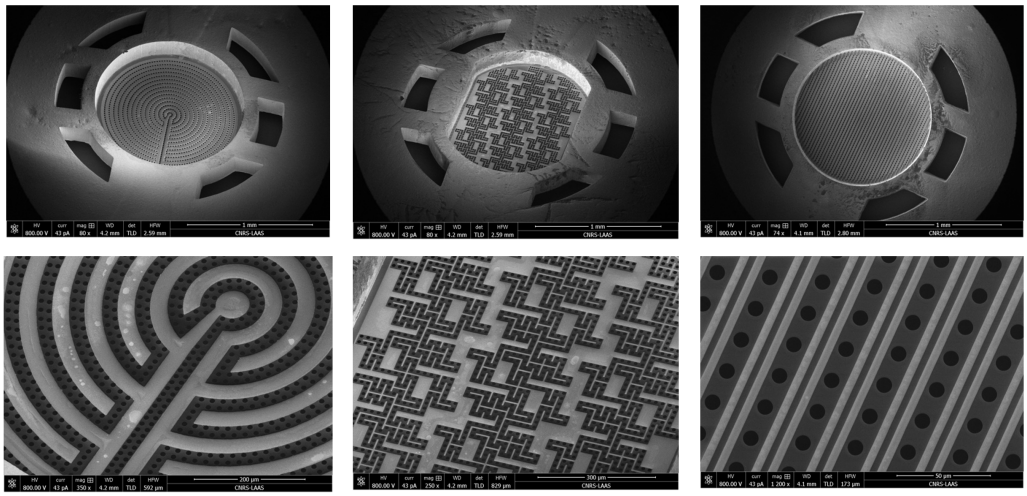

Figure 2.18: SEM Micrographs of three different designs with a large view of the device comprising the supporting structure on the first row. The second row is a zoomed-in micrograph on the membrane exhibiting multiple electrode geometries.

As a side note, SEM characterization can sometimes bring surprisingly beautiful and unexpected insights, especially during the development of new processes. We share in figure 2.19 two of these unexpected electron micrographs. This form of microscopy enables us to explore new perspectives beyond human perception. The appeal of the images produced through this method may stem from their precise beauty: the depiction on the monitor is flawless, as intended (see figure 2.18). Nevertheless, encountering beauty during the investigative process, such as when a process step performed unexpectedly, yields an entirely distinct sensation. During such explorations of unfamiliar worlds, our minds make connections with our previous sensorial experiences to try and understand what it sees: the depth of glaciers crevasses, a glazed cherry on top of a frosted cake ... or just a cracked resist and a sputtering default? These occurrences are highly personal, intimate, and arduous to share, yet so much more profound.

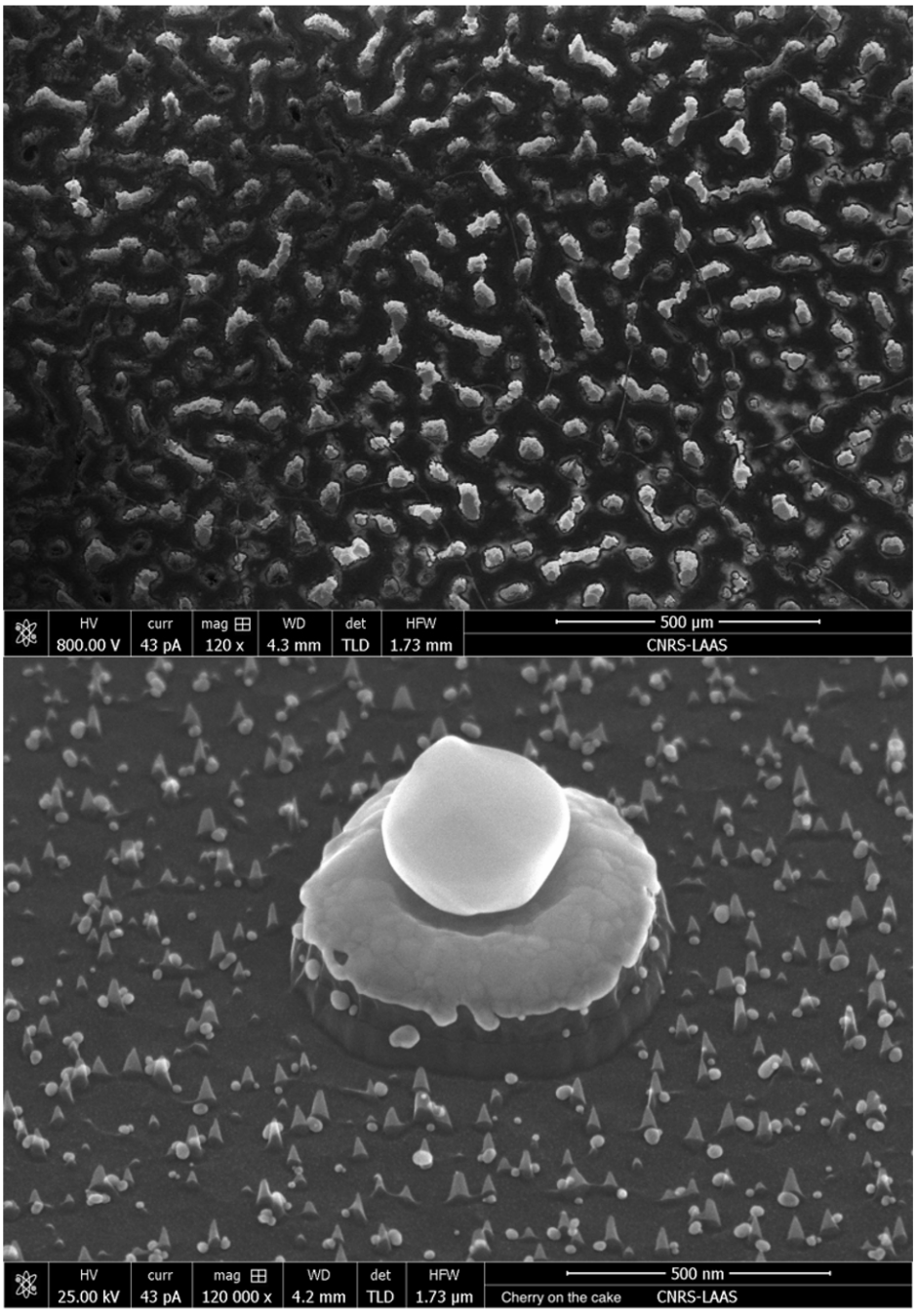

Figure 2.19: SEM Micrographs of process side effects. On the top, resist cooling induced cracks in it, the golden layer beneath it was a shining light from its depth. On the bottom side, a metallic micro particle of unknown origin induced micro masking effect during an etching process, resulting in a nicely glazed cherry cake.

2.3 Experimental Characterization of Microfabricated Devices

2.3.1 Experimental Platform

As depicted in figure 2.20, the experimental setup consists of a fluidic system to transport the different solutions through the filter, an electrical system for measuring the impedance of the device and a holder which encapsulates this device within the fluidic channel and relocates electrical contacts outside of the holder.

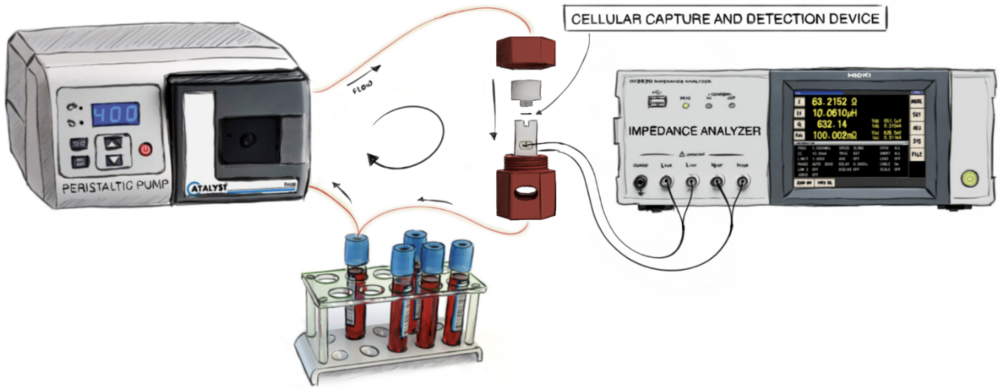

Figure 2.20: Experimental setup using a peristaltic pump to flow samples through the cellular capture and detection device. The microfabricated device is held in the fluidic system using a 3D printed holder. This holder has integrated pogo pins for electrical contact in between the microdevice and the impedance analyzer.

The fluidic system is composed of a peristaltic pump (Catalyst FH100) and a 1.6 mm internal diameter silicone biocompatible tubing (Masterflex™ 06424-14). This pump is using a 3-cam rotative head to push the fluid along the tubing and is controlled in terms of the number of rotations per minute, thus allowing a precise flow and regular flow control without tampering with the sample. The sample is processed in a closed loop at 30 RPM, which yields a flow rate of 11.5 mL/min.

The electrical setup consists of an impedance analyzer (HIOKI IM3570) connected through shielded coaxial wires to the holder pins. Some of its main functionalities and technical specifications are reported in table 2.1.

Measurement Modes	LCR and Analyzer
Measurement Range	100 mΩ to 100 MΩ
Measurement Frequency	4 Hz to 5 MHz
Measurement Accuracy	Z ±0.08% and θ: ±0.05°
Measurement Time	0.5 ms (FAST mode at 100 kHz)

Table 2.1: HIOKI IM3570 Impedance Analyzer specifications.

Finally, the holder is composed of two locking systems. The two inner pieces of the holder, represented in white on the figure 2.21, are machined from a biocompatible material (POMc, polyoxymethylene in its copolymer form), and are intertwined to hold the microdevice in place and close the fluidic channel. Two toroidal gaskets are used above and below the microdevice, to seal it in the fluidic channel. Top and bottom sides of the holder present threaded slots for inlet and outlet fluidic connectors. Spring loaded pogo pins (Harwin P70-2300045R) are inserted to contact the pads leading to the electrodes on the microdevice. A second 3D printed (FDM, Fused Deposition Modeling) layer encapsulates the first two pieces to hold them intertwined using a screw mechanism (in red on figure 2.21). Slits and openings ensure the accessibility of both the electrical and fluidic connectors are accessible when closed.

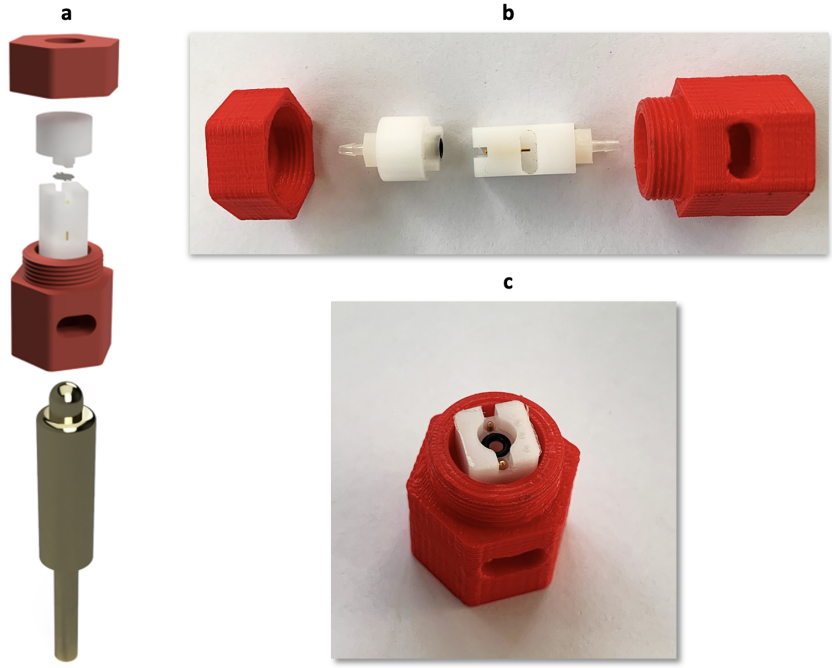

Figure 2.21: (a) Scattered 3D model of the holder machined in POMc (white parts), 3D printed (red parts) and the spring-loaded pogo pin used for electrical contact in between the microfabricated device and the impedance analyzer. (b) Scattered and top view (c) of the fabricated filter holder.

2.3.2 Experimental Protocol

The solutions used during experiments include ethanol, PBS (Gibco 1X), RPMI (Gibco 1640), Fetal Bovine Serum (FBS), paraformaldehyde (formalin, neutral buffered 10%). The blood samples are purchased from Etablissement Français du Sang (EFS, 6 mL whole blood tubes with EDTA coating). Bleach and deionized water are used to clean and sanitize the holder. The impedance analyzer calibration is done using two specifically designed devices for both the open and short calibration respectively shown on figure , thus compensating for length of cable and potential parasitic effects at the junctions of the spring-loaded pins.

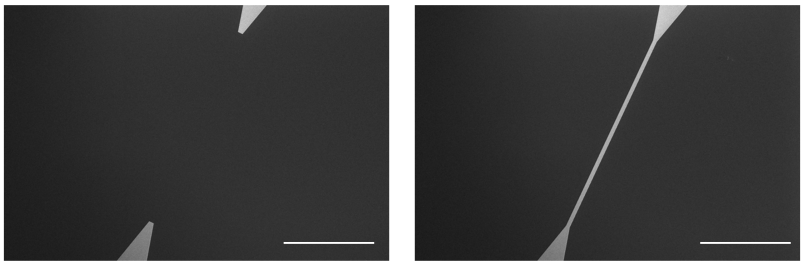

Figure 2.22: SEM Micrographs showing electrode designs of the calibration devices: open calibration and short calibration. These devices follow the same fabrication process, being on the same wafer as the sensing devices. Scale bar is 500µm.

Once the impedance analyzer is calibrated, the microdevice is inserted in the holder, which is connected both to the fluidic system and impedance analyzer. Priming steps include flowing 15 mL of ethanol to improve the wettability of the device and remove any trapped air bubble. Next, 15 mL of PBS is used to replace ethanol in the system and establish physiological conditions. These priming steps are applied in an open-loop setup and in reverse flow (against the normal flow direction as defined in figure 2.1) to remove eventual impurities.

A first reference impedance spectrum is measured in PBS. The 5 mL sample of the fluid to analyze is then processed in a closed loop for 10 minutes in forward flow at 11.5 mL/min. During this time, impedance spectroscopy measurements from 1 kHz to 5 MHz at 50 mV are performed every 2 minutes until the end of the process.

Post-processing steps include the rinsing of the fluidic system with 20 mL of PBS in forward flow followed by the introduction of paraformaldehyde for cell fixation. The incubation takes 20 minutes. The fluidic system is then washed off paraformaldehyde with another 20 mL of PBS before retrieving the holder and the microdevice from the setup. Devices are then mounted in between slide and coverslip with a mounting medium for optical observation. Optical observations are made under an upright Olympus microscope with Bright field, GFP and Hoechst fluorescence imaging, depending on the staining used, with 10x and 20x objectives. Even though the fluidic system is closed, for safety reasons, the experimental platform is mounted under a chemical hood whenever paraformaldehyde (PFA) is used.

2.3.3 Biological Model

Cells used for experiments are from a prostatic cancer cell line PC3 established in 1979 [67]. They have been genetically modified to generate the Green Fluorescent Protein within their cytoplasm. This protein, first isolated from a jellyfish in 1962 [68] (Aequorea victoria) exhibits two excitation peaks, a major one at 395 nm and a minor one at 475 nm and its reemission is at 509 nm. Together with this addition, a gene was added, inducing the resistance of the cells to the G418 (or Geneticin) antibiotic. During cell culture, the addition of such antibiotic will create a selection pressure, therefore ensuring that every cell present in the culture still has its genetic modification intact and exhibits GFP.

Hoechst staining is also used for nucleus staining through DNA interlacing. This staining is done manually, usually after the experiment by using a mounting medium which incorporates that staining agent. This compound has an excitation wavelength of 350 nm and retransmits at 461 nm which is distinct from the GFP staining, therefore, two different light filters or "cubes" are used to access individually these two fluorescent signals.

The culture of these cells is done within a pressurized biological laboratory at LAAS (safety level P2). Every cell passaging is done under a microbiological safety cabinet for protecting the cell culture from contamination through a sterile environment and follows the usual steps of cell passaging. The cells are then incubated at 37°C and 5% CO2 in a high humidity environment to avoid medium evaporation.

The medium used for cultivating these cells is composed in majority of RPMI 1640 which is a culture base containing vitamins and phenol red, allowing a pH control through the color of the medium. To this base is added 10% of Fetal Bovine Serum (FBS) which is the main growth factor. To avoid contamination, penicillin is added at the rate of 1% and, to keep a selection pressure, G418 is also added at the rate of 1%.

Figure 2.23 show bright field microscopy images of PC3 cells during cell culture. Their elongated, fibroblast like shape is characteristic of adherent PC3, they, however, go back to rounded shapes when in suspension. b exhibit PC3 cells at high confluence and their surprising wavy self-alignment pattern following the theories of nematic liquid crystal [69].

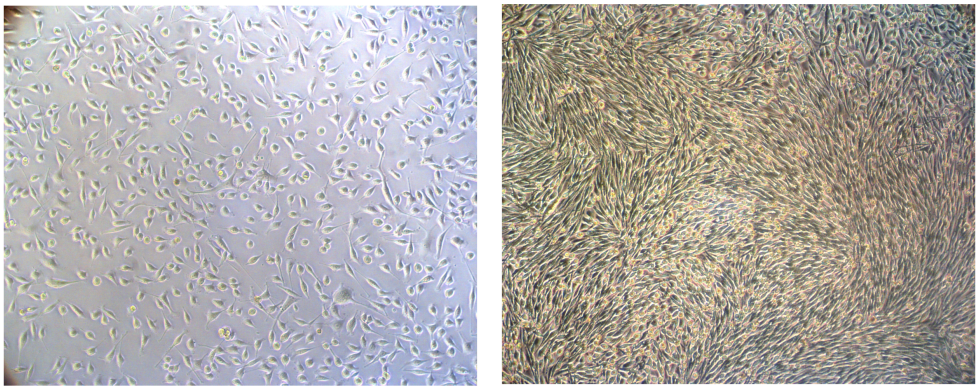

(a) **(b)**

Figure 2.23: (a) PC3 cell culture at "normal" density. Living cells are adherent to the substrate (culture flask) and look elongated compared to rounded dead cells which detach from the substrate.(b) PC3 cell culture at high confluence creating beautiful wavy patterns. We can see that the cells self-align in a priori random directions. This phenomenon follows the theories of nematic liquid crystals [69].

Finally, the upcoming experiments may mention that a sample is spiked with cells. It means that cultivated PC3 cells are added in a controlled concentration to a sample with the idea of mimicking circulating tumor cells in biological samples (whole blood, blood plasma) or in simpler media (culture media, saline solution). Figure 2.24 shows the size repartition of PC3 cells with a mean diameter of 17.4 µm (±0.4 µm) which therefore should be retained by the 10µm diameter pores of the filtering membrane.

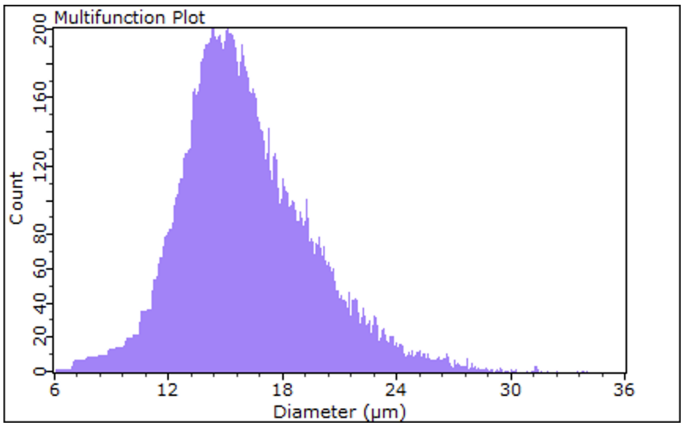

Figure 2.24: Histogram of PC3 cells size in suspension with a mean diameter of 17.4 µm (±0.4 µm), measured using a Scepter cell counter.

2.3.4 Cell Capture Characterization

Although the fabrication process described above was developed based on from the experience of SmartCatch company in the design of cell capture membrane, the use of a novel, 1.4 µm thin membrane for cell filtration has never been explored before.

Moreover, since the experimental platform does not allow live in-situ optical monitoring of the cell capture, the results shown in figure 2.25 are remote images of the final configuration of the captured cells by the filter. Dynamic phenomena on the capture mechanism are not accessible. Thus, any further evaluation of the impact of the flow rate on cell capture efficiency would either require modifications of the experimental platform or a tremendous number of experiments to access to statistically significative data. However, since the fabrication yield of electrically functional devices is low, qualitative characterization of the capture on the membrane took precedence over quantitivity which could only be done through numerous experiments.

The functionalities that are required from the filtering membrane are to trap and hold cells above a certain size threshold on the membrane during the filtration process. An appropriate alignment of the trapped cells on the membrane pores is also essential for future electrical characterization. Cell Capture experiments were led following the experimental protocol described above without electrical measurements. The ambition of such experiments is to explore the capture ability of the fabricated devices together with understanding the kinetics and various effects at play during the filtration process.

Hence, filtration was experimented in two different media: in culture media for preliminary experiments, thus characterizing capture phenomena. Then, we chose to filter cells from whole blood to demonstrate the usability of such devices in complex media.

Filtration of PC3 Cells in RPMI

Evaluation of the cell capture ability was done in a simple, culture media (RPMI with 5% FBS and antibiotics) with spiked PC3-GFP at a concentration of 1000 cells/mL within 5 mL. The sample was processed in a closed loop for 10 minutes and the experiment repeated over 3 identical devices. The Hoechst nucleus staining is done after the capture experiment through the mounting medium. Having access to both a nucleus and a cytoplasmic staining allows individual counting of the overlapping cells by counting the number of nuclei but also evaluates cell stacking through the GFP staining.

The results shown in figure 2.25 display the superposition of GFP, Hoechst (respectively in green and cyan) and Bright Field fluorescence images taken after the experiment. The cell distribution over the membrane is homogeneous in the sense that there are not apparent zones depleted of captured cells with a random distribution of the occupied pores across the whole membrane surface and, as shown on Figure 44, the positioning of the trapped cells corresponds well to the membrane pores. A priori, there does not seem to be any unwanted adsorption or sedimentation phenomena of cells on the membrane out-off the pores during cell filtration. We therefore conclude that the physical capture is related to the transmembrane pressure differential inducing flow lines across the pores and size retention of all the PC3 of the population that exhibit sufficient size and stiffness for not being able to translocate through the cylindrical pore.

It is also interesting to note that, despite the non-filtering fluidic slits on either side of the membrane, a certain number of cells are trapped and maintained on the membrane, even under a high flow rate (12mL/min). The capability of the membrane to hold cells while the sample processing goes on is indeed a very important feature for future electrical characterization. Removing the fluidic slits may improve the capture efficiency (currently in between 11% to 15%), however, covering the membrane with cells without fluidic slits may drastically increase the transmembrane pressure and therefore push trapped cells through the membrane.

Finally, we demonstrated through these preliminary experiments that the devices allow for a clean capture of spiked cells: cells are well positioned on the membrane pores, in between sensing electrodes. Moreover, trapped cells seems well held on the membrane which filling rate is of 40% with well-positioned cells on pores, in between sensing electrodes, therefore setting promising conditions for electrical in-situ characterization.

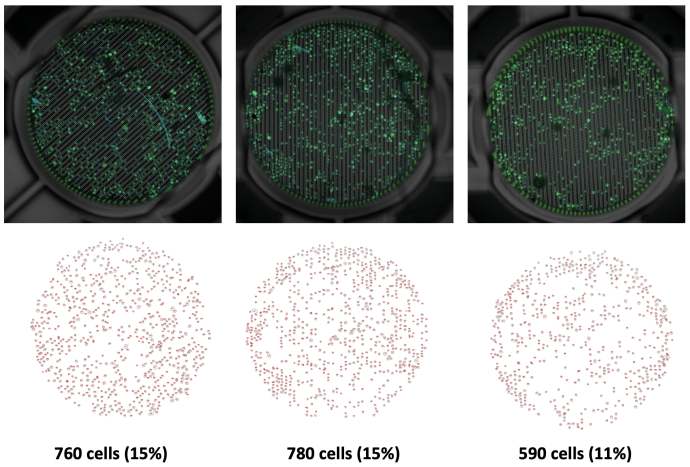

Figure 2.25: Illustration of cell capture (PC3-GFP) in culture media (triplicates). The first row shows a microscopy image superposition of GFP (cytoplasmic staining, green), Hoechst (nucleus staining, cyan) and bright field) for each device with a 10X objective. There are no apparent zones depleted of captured cells with a random distribution of the occupied pores across the whole membrane surface. The fluorescent signals are then processed to automatically count the number of collected cells on each membrane and display the capture rate relatively to the sample cell initial concentration (2nd row).

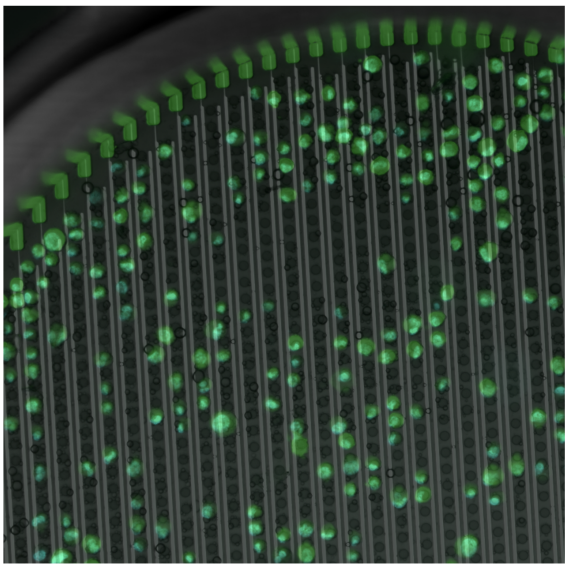

Figure 2.26: Zoom on the third device presented in the previous figure 2.25. The positioning of the trapped cells corresponds well to the membrane pores, in between the sensing electrodes. A priori, there is not unwanted adsorption or sedimentation phenomena of cells on the membrane out-off the pores during cell filtration.

Filtration of Complex Media

Following the previous cell capture demonstration established on cancer cells in a simple media, it is interesting to explore complex media such as biofluids. Preliminary capture experiments in whole blood will therefore be presented in this section.

Blood is composed of figurative elements [70–72] and a liquid medium: the plasma [73]. Figurative elements of blood include erythrocytes (red blood cells for 99% with 5 to 7µm in diameter) which does not contain nuclei nor organelles. On the other hand, leukocytes (white blood cells, 7µm to 25µm in diameter) represent 0.2% and are part of the immune system through different kinds of nucleated (and polynucleated) cells: granulocytes, lymphocytes or monocytes. Finally, thrombocytes (platelets, 2µm to 4µm in diameter), responsible for the blood coagulation represent up to 1% of the figurative elements within blood. The figurative elements constitute 45% of a blood sample and the 55% is the blood plasma. Blood plasma is the liquid compound of blood in which are all the figurative elements. It is mainly composed of water and contains lipids, glucose, and proteins.

Whole blood samples are a good example of complex biofluids: the encompass many biological elements of different sizes and the high number of elements impact the viscosity, thus making it non-Newtonian [74–76]. Moreover, blood hematocrit may vary a lot from one person to another [77, 78]. Therefore, combining all these aspects, blood is an interesting sample to process through the filtering membranes. It should be noted that, since biological elements are already present in whole blood samples, cultured cancer cells will not be used for spiking the sample. Indeed, a first question which may rise is, regarding the composition of blood as depicted previously, both in terms of element size and occurrence, which element will be captured on the membrane. Based on the previous description, it seems that RBC (red blood cells) and platelets should pass through the membrane and WBC (white blood cells) stay trapped within the membrane. However, the high concentration of RBC (5 billion/mL) compared to the one of WBC (5 million/mL) may still fill the membrane by clogging, therefore limiting the WBC capture.

Blood samples consists of 6 mL EDTA coated tubes collected from healthy donors of EFS. The filtration protocol is kept identical to the protocol previously described. To avoid sample tampering and be able to evaluate the devices in real conditions, no chelating agents were added to the collected blood sample.

Before starting the filtration protocol, the blood sample is mixed using a Vortex mixer to resuspend all the blood cells and have a homogeneous distribution. The sample is processed in the system for 10 minutes at 12mL/min in a closed loop. Post filtration, the device is then mounted in between slide and coverslip with a mounting medium integrating a Hoechst staining solution, thus staining nucleated blood cells (leukocytes).

Figure 2.27 exhibits two devices post filtration with a superposition of Hoechst

(in blue) and Bright Field images. Blue trails can be seen on this figure, they are dust trails which are fluorescent in the Hoechst wavelength. Stained nuclei appear on both capture devices and, according to the composition of blood samples, we assume that they are PBMCs (Peripheral Blood Mononucleated Cells). Although the blood donors are healthy, these stained nucleated cells could also be circulating tumor cells. However, a more complex staining combination would be needed to assess this possibility.

Furthermore, the repartition of trapped cells seems to be relatively homogeneous as in the previous experiments. We can, however, see a capture depletion in figure 2.27b in the top right corner. This depletion is next to what looks like a trapped air bubble and a trail of dust. Both the bubble and the dust could also have been introduced after sample processing during the device manipulation for its removal from the experimental setup and transferred to a glass slide for observation. Further experiments are needed to assess the impact of pollutants on the filtering efficiency of the membrane, although it seems to stay localized.

The number of trapped WBC could, however, not be evaluated since many cells seems to form aggregates on the membrane which complicated the cell counting. We can also see that the positioning of cells regarding the membrane pores is not as efficient as previous experiments in culture media. Indeed, cells seem to be spread over the membrane without apparent preference for interstices between the sensing electrodes or the filtration pores. We can, however, observe unstained capture material which, if linked to the WBC through an aggregate, could explain the poor cell/pore alinement. This unstained material cannot be characterized without further specific staining.

Finally, even though the cell density in whole blood is large compared to the number of pores on the filtering membrane, the membrane is not clotted and still exhibits free pores. Whether some pores are free because of a physical capture limitation or because of an increase in transmembrane pressure pushing the cells through the membrane is not known at this stage. However, the transmembrane pressure may have increased following the filling of the membrane, this increase must have been limited by the fluidic slits since the nucleated cells were not pushed through the filter.

These preliminary experiments demonstrate the capability of the device to operate in complex media without inducing clogging. Although the number of trapped RBC and platelet could not be evaluated, the ability of the membrane to capture and maintain WBC on the filtering membrane within a crowded environment is demonstrated. We can see that the positioning of cells above capture pores could still be improved even though stained WBC are well present in electrodes defined sensing areas.

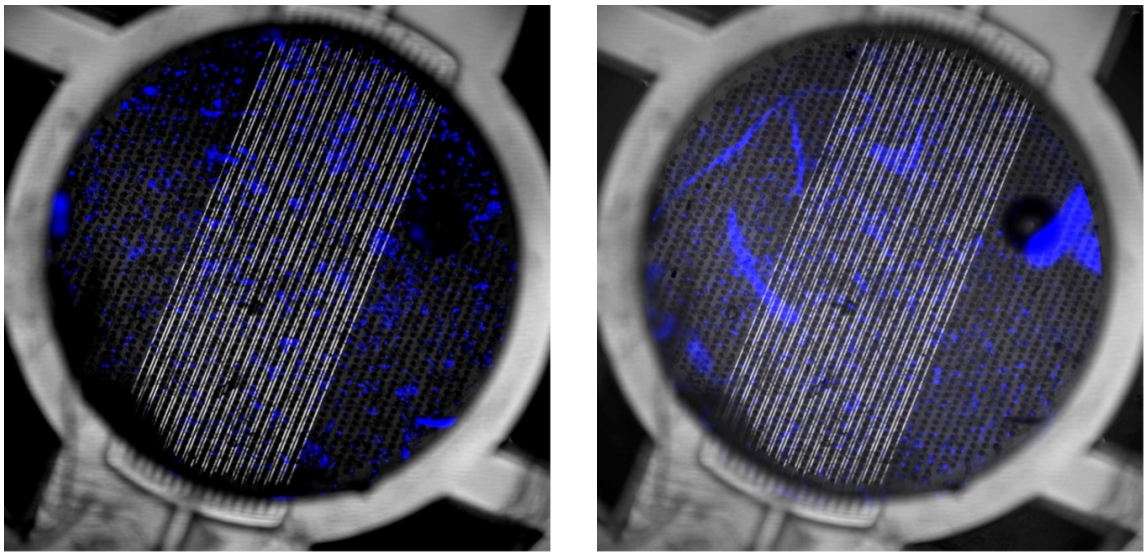

(a) **(b)**

Figure 2.27: Whole blood sample processing (duplicate). Superposition of Hoechst and bright field images with a 10x objective. Stained cells a probably peripheral mononucleated blood cells which were captured on the filtering membrane. No capture depletion nor preference seems to be observed from the electrode defined sensing areas which are well covered by trapped cells.

2.3.5 Electrical Characterization of in-situ Cell Capture

The membrane characterization presented above addressed and demonstrated the capture ability of the membrane both in simple and complex media. In the following sections, the electrical aspect will be characterized and discussed.

Multiple design shown previously were fabricated. The first electrical characterization of the devices is therefore made in a saline, electrolytic solution (PBS) which is electrically close to culture media and whole blood in terms of conductivity (1,6 S/m). The point of this first characterization is to electrically compare electrode designs through their frequency response by measuring impedance spectra. It will also allow the development of an equivalent electrical model which will be used to further interpret electrical measurements in more complex media.

Indeed, following these preliminary experiments, best performing electrode designs will be characterized in two different media: (1) in PBS solution with added microspheres therefore mimicking a cell suspension in an electrolyte, and (2) in whole blood samples. Therefore, the sensitivity of the device together with insights in cell capture kinetics and parasitic effects will be discussed.

Results presented in the following section were all obtained using the experimental platform together with the protocol described previously. The flow rate used is of 11.5 mL/min which corresponds to 30 rotations per minute of the peristaltic pump and electrical impedance spectra are ranging from 10 kHz to 5 MHz at 50 mV. The

overall sample processing time is 10 minutes with electrical measurements taken every 2 minutes.

Reference Measurements in PBS Solution

Calibration measurements are performed in a PBS solution, within the closed fluidic platform presented previously. The goal is to evaluate the measurement drift which could be induced by the different elements forming the experimental platform (pumping system, temperature, etc.).

Figure 2.28a exhibits the relative deviation S (%) defined in Eq. 2.1 of the magnitude of the impedance in static PBS with the peristaltic pump stopped for 10 minutes in the range of frequency of interest for our measurements. The mean relative deviation over the frequency band is of 1.2%, thus indicating that impedance measurement in PBS is stable and is therefore a good reference for future experiments.

$$S = 100 \times \frac{|Z|_{10min} - |Z|_{0min}}{|Z|_{0min}} \tag{2.1}$$

Where $|Z|_t$ denotes the measured magnitude of the impedance at time t [minutes]. Following characterization measurements were done in PBS, under flow, using the previously described experimental protocol. Figure 2.28b exhibits the relative impedance measurement shift over 10 minutes of PBS circulation at 11.5 mL/min. Its mean is of 0.7% which indicates that, under flow, the device measurements are highly stable along time.

It is interesting to note that the drift of impedance measurements is lower when the device is under flow than when the PBS solution is static. This phenomenon may have multiple sources. Indeed, a temperature gradient in the vicinity of the filter which is magnified when the solution is not flowing may introduce such a shift. Also, although the solution is considered homogeneous, local ionic gradient could be the reason for the impedance measurement drift. Even though the order of magnitude of both the static (a) and dynamic (b) shifts seems comparable, complex electrochemical and fluidic effects are at play in between these two states which prevents us from trying to correlate them.

Finally, the presented results were obtained using devices with the hybrid design. They were, however, repeated on the other designs, as well as which each showed a similar behavior, both in terms of frequency and amplitude.

Following calibrations and stability measurements, each electrode design impedance is measured in a PBS solution under flow. Figure 2.29 present impedance magnitude and phase of each device. The overall shape of the impedance modulus exhibits first a downward slope followed by a plateau which is characteristic respectively of a capacitive behavior and a resistive behavior. Indeed, as discussed in chapter 1,

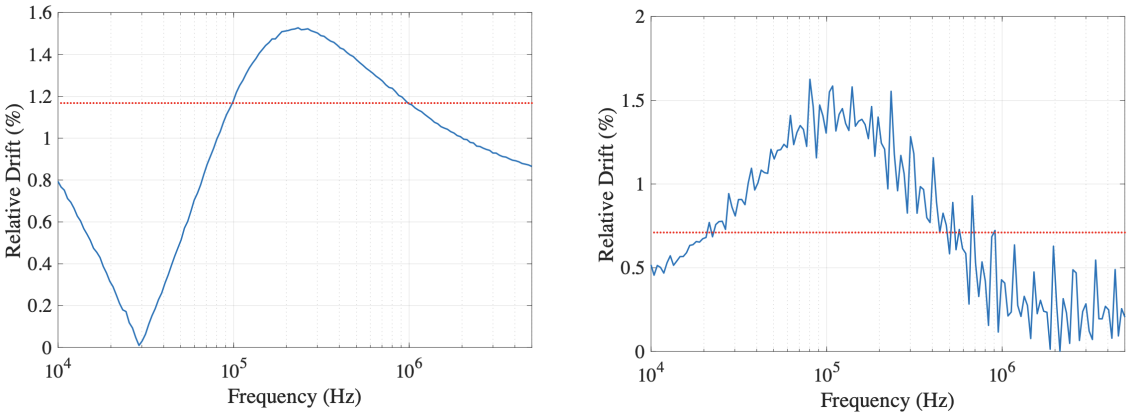

(a) **(b)**

Figure 2.28: Relative impedance measurement drift along 10 minutes against measurement frequency with the pumping system turned off (a) and 11.5 mL/min of flow rate (b). Dashed red line shows the mean impedance drift over the frequency measurement range.

the impedance of a capacitor is inversely proportional to the frequency whereas the impedance of a resistor is independent to the frequency.

Moreover, a capacitance induces a -90° phase angle whereas a resistance does not affect the phase angle (0°). The phase diagram displayed in figure 2.29 confirms the transition from a capacitance to a resistance behavior.

Therefore, to further investigate these experimental results, a simple equivalent electrical circuit composed of a capacitance in series with a resistance is used to fit each experimental spectrum. Moreover, the coupling of these two elements in series generates a cut-off frequency at which the system transitions from the capacitive regime to the resistive one and which is reported in table 2.2 along the fitted values for both components for each electrode design shown in figure 2.29.

Following chapter 1, the capacitance is induced by the interface in between the metallic electrodes and the electrolytic solution. The induced electrical effect is called a double-layer capacitance (DL capacitance).

The resistance reported in table 2.2 models multiple resistive effects which are cumulated in series: the contact resistance, the access track resistance, and the inter-electrode resistance generated by the electrolytic medium. However, impedance measurements do not allow to investigate these effects separately, as they are modeled by a sum in a single resistor. Nevertheless, since the access tracks and contacts are identical for every electrode design, we assume that their resistance is identical, thus, a change in resistance from one device to another will be attributed to the inter-electrode resistance, which may differ from one design to another.

From table 2.2, we can observe that the devices offering the lower cut-off frequency, and therefore larger resistive bandwidths, are the concentric and fractal designs with the hybrid design exhibiting the highest cut-off frequency. On the other hand, the

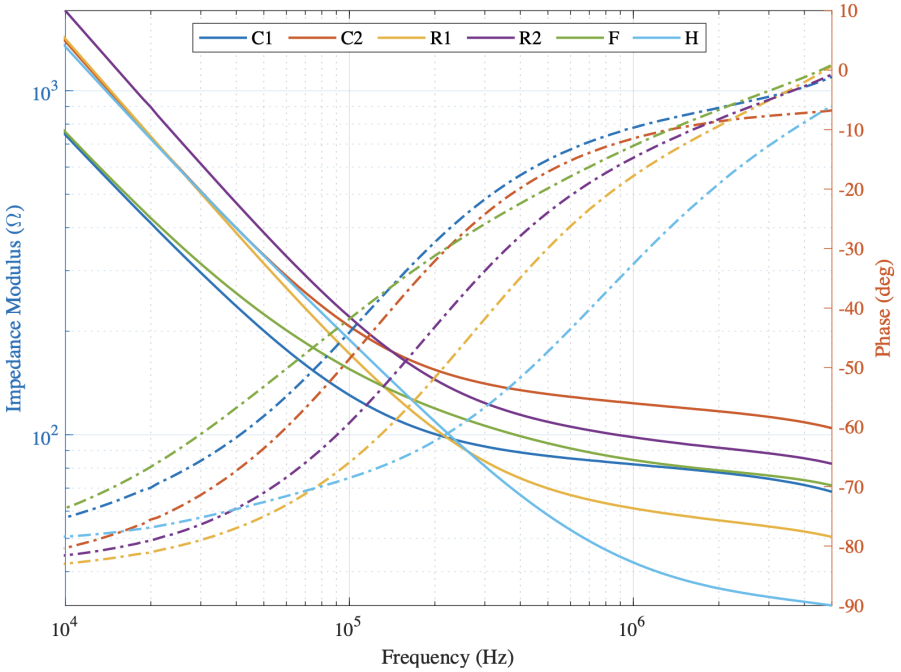

Figure 2.29: : Spectra of the impedance magnitude (full line) and phase (dashed lines) for each device design: Concentric with either 14µm (C1) or 29µm (C2) electrode spacing, Rectangular (R1 and R2), Fractal (F) and Hybrid (H). The data is plotted from 10 kHz to 5 MHz.

	Con. 1	Con. 2	Rect .1	Rect. 2	Fractal	Hybrid
Resistance	78 Ω	113 Ω	68 Ω	90 Ω	96 Ω	34 Ω
DL Capacitance	17 nF	8.8 nF	12.5 nF	8.1 nF	21.3 nF	9.3 nF
Cut-off Frequency	120 kHz	160 kHz	187 kHz	218 kHz	78 kHz	504 kHz

Table 2.2: Device resistance, double-layer capacitance and cut-off frequency in PBS 1X for each electrode design following a curve fitting process of impedance spectra presented in figure 2.29 on a series RC equivalent electrical circuit.

hybrid design and rectangular design (with an inter-electrode spacing of 14µm) offer the lowest resistance.

The DL capacitance value is proportional to the electrode surface, as described in chapter 1. Thus, for a given electrolyte, the DL capacitance of coplanar electrodes per unit of surface ($F/\mu m^2$) is constant in between devices and the overall double-layer capacitance (in Farad) will be dependent on the electrically effective surface of the electrodes. This electrically effective surface usually differs from the geometrical one, as it characterizes the interface between the electrode and the electrolyte, both at the atomic scale. Indeed, if the electrode surface is roughened, its real surface won't follow the usual S=l×w equation but will be larger [79, 80]. Small defects such as resist leftovers or micro/nanoscale electrode structural defects will play a role in this evaluation. Moreover, even though the electrolyte is considered identical, local changes in ionic concentrations of the multiple ionic layers building up next to the electrodes will also be reflected on the effective surface [81]. It is, however, essential

to precisely characterize the effective electrical surface since it reflects the sensing surface of the electrodes and is needed for dimensionless measurements to compare equally different electrode designs.

Looking at the double layer capacitances reported in table 2.2, three groups of electrode designs can be made, in decreasing order of capacitance and therefore decreasing electrical effective surface. The respective geometrical surface is indicated next to each electrode design.

1. Fractal (380.103 µm^2) and Concentric 1 (554.103 µm^2)
2. Rectangular 1 (570.103 µm^2)
3. Hybrid (291.103 µm^2), Rectangular 2 (486.103 µm^2) and Concentric 2 (500.103 µm^2)

We can see through this list that the effective surface is not only poorly related to the geometrical one, but also that, since the sensor is coplanar (i.e. based on fringe effects), the shape of the fractal design and number of finger elements of the hybrid design places them at a high effective surface compared to their geometrical one.

Looking at the resistance in PBS solution of every electrode design, all are in the same range except the hybrid design. The "basal" resistance (resistance in the reference medium) is important to consider, as it directly impacts the sensitivity of the sensor. Indeed, considering a cell inducing a given resistance in between the electrode's sensor, the relative impedance change on the overall system induced by the cell will be larger on a low impedance sensor.

As discussed previously, combining these two effects in series leads to the creation of the two respective regimes (capacitive and resistive) with a transition at a cut-off frequency. This frequency is measured and reported in table 2.2. In order to sense biological cells, present in between electrodes, the system must reach a resistive regime within the measurement band, which is given by the impedance analyzer limits shown in table 2.1.

The calibration and reference measurements allowed the characterization of the microfabricated devices through an electrical equivalent circuit. Curve fitting based on the electrical model was used to extract components values and compare the different electrode designs. Out of the 6 fabricated designs, all of them offer a low enough cut-off frequency, therefore enabling the resistive regime to be reached within the measurement range. However, among these devices, two of them show a lower basal resistance, thus a potential higher sensitivity to cells: (1) the rectangular design with a single row of pores and (2) the hybrid design. Hence, these two designs will be preferred for upcoming experiments.

Microsphere Density Detection in PBS Solution

Leading towards cell filtration and detection experiments, microspheres were first used to mimic cell filtration together with electrical detection on the rectangular design with a single row of pores in between the electrodes. Highly electrically insulating polystyrene microspheres of 10µm in diameter were flown through the device in a PBS solution at high concentration (105 particles/mL) to fill as many pores as possible on the filtering membrane.

Figure 2.30 shows the filtering membrane after sample processing. The fluorescence image exhibits well positioned spheres on the membrane pores as well as what appears to be clusters of spheres sitting on top of the sensing electrodes. Although each pore is not filled, the density seems to correspond well to the one obtained on previous experiments (see figure 2.25 and figure 2.27).

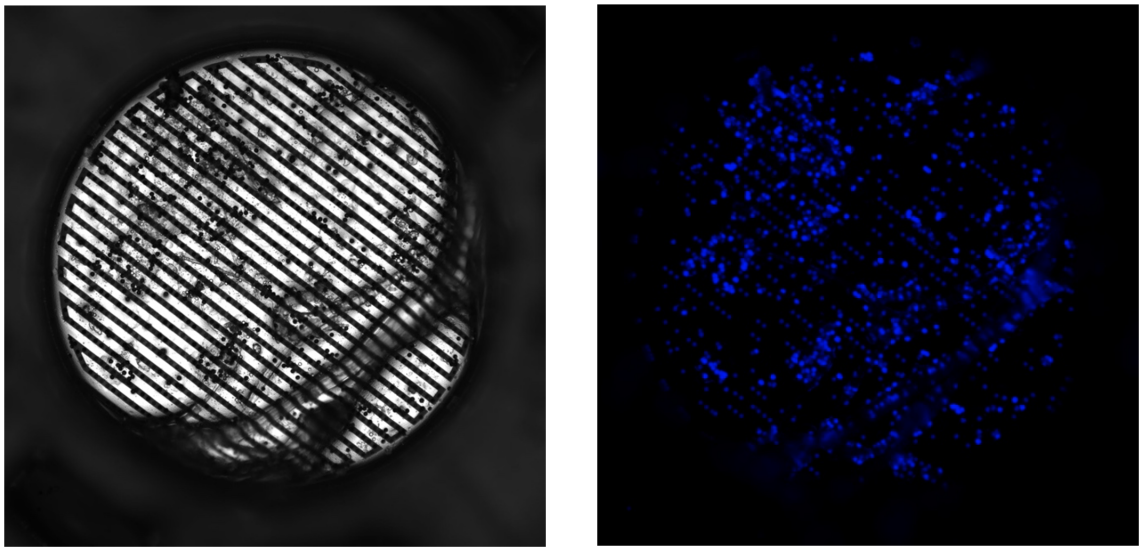

(a) **(b)**

Figure 2.30: Optical Microscopy images with a Bright Field view (a) and a DAPI view (b) of the collected µSpheres on the filtering membrane.

In-situ impedance spectroscopy measurements were performed every two minutes along the filtration process. Figure 2.31 exhibits these impedance spectra and their relative shift (as described in the previous section by Eq. 2.1) in frequency. Over the measurement range, the deviation is the largest (up to 19.7%) between 300 kHz and 5 MHz, that is, in the resistive regime region of this electrode design. Therefore, the inter-electrode resistance, characterizing the inter-electrode medium and its constituents (microspheres in this experiment) increased over the 10 minutes of sample processing of 20%.

Moreover, we previously evaluated the impedance measurement shift at 1.2% in static PBS and 0.7% in a PBS flow of 11.5 mL/min. This 20% impedance shift is therefore induced by the addition of the microspheres within the PBS sample.

Indeed, the replacement of the PBS solution in between the electrodes by the insulating microspheres along their capture by the filtering membrane raises the inter-electrode resistance and therefore impacts the overall impedance spectra. These first results of electrical measurements in a solution containing microspheres mimicking biological cells demonstrate the combined functionality of capture through the filtering membrane and in-situ detection of captured elements using the sensing electrodes.

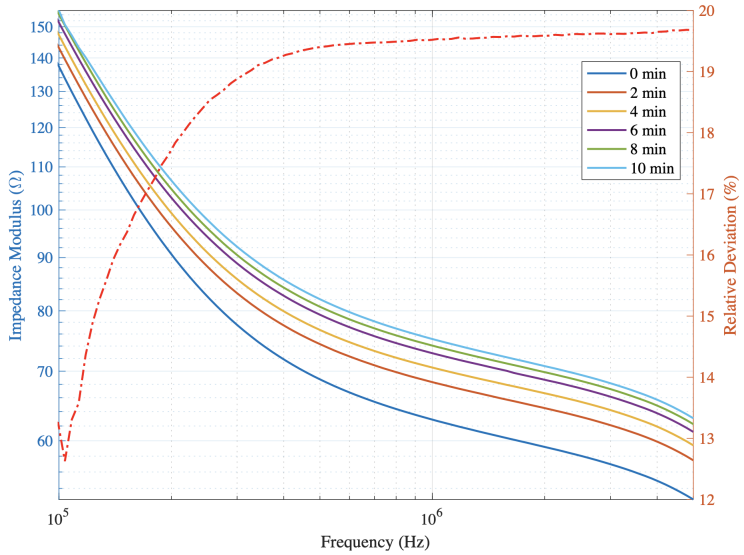

Figure 2.31: Impedance Spectra Modulus (full line) taken every two minutes for ten minutes during a filtration process of 10µm µSpheres in PBS 1X. The red dashed line represents the relative deviation over 10 minutes along frequency measurement.

Cell Density Detection in Whole Blood

Preliminary electrical detection was demonstrated in the previous section on microspheres within a PBS solution. As described in the previous section regarding whole blood composition, the large number of figurative elements is processed at high concentration. We herein aim at expending this in-situ electrical detection to biological cells within whole blood samples. Processing such samples brings fluidic challenges and electrical ones as well. Indeed, the rectangular design was sensitive enough to detect the accumulation of microspheres on the membrane. However, electrically characterizing biological elements may induce a lower shift. On the other hand, the high concentration of figurative elements within a blood sample may disturb the electrical measurements, thus hiding the detection signal in the electrical noise induced by the billions of cells. Herein, we will evaluate the sensitivity of the hybrid electrode design to detect the cell density over the membrane while processing the whole blood sample and compare it to electrical characterization of three media without cells: blood plasma, culture media and PBS solution.

Figure 2.32a exhibits the typical impedance spectrum profile and gives the magnitude of the device impedance as a function of the frequency from 1 kHz to 5 MHz. Plotted data were obtained at 0 min, 2 min and 10 min under whole blood circulation through the device. Between 1 kHz and 100 kHz, the device impedance does not change significantly when the blood flows, while in the 100 kHz to 5 MHz frequency range, the impedance magnitude |Z| increases gradually over time. Measured impedance spectra can be fitted using a very simple electrical circuit, as discussed in the following section. To characterize the time variation of the impedance, the magnitude |Z| at 1 MHz is displayed in figure 2.32b as a function of time t for two identical experiments and nominally identical devices. We can notice an increase in the magnitude during the first 4 minutes and a plateau indicating a saturation-like behavior before the end of the experiment.

In figure 2.32c, we report the shift of impedance magnitude between whole blood circulation and three control experiments, where a saline solution (PBS 1X), a cell culture medium (RPMI with 5% FBS) and blood plasma are used. The impedance relative shift S (in %) is derived from measurement results obtained at 1 MHz. The relative shift during the 10-minute experiments with whole blood ranges from 44% to 46%, while it is limited to 8% to 16% for blood plasma and 2% to 7% and 1% to 4% for the culture medium and PBS solution, respectively.

The stability of the impedance spectrum at low frequencies (between 1 kHz and 100 kHz see Figure 2.32a) originates from the predominance of the ionic DL capacitance. As it is unchanged under blood circulation, the low-frequency impedance spectrum cannot be used to detect any adsorption or cell capture on the micro-perforated membrane. By extension, the impedance stability also indicates that variations due to environmental factors (including temperature fluctuations) are negligible and that microelectrodes are not damaged during experiments by potential faradic reactions.

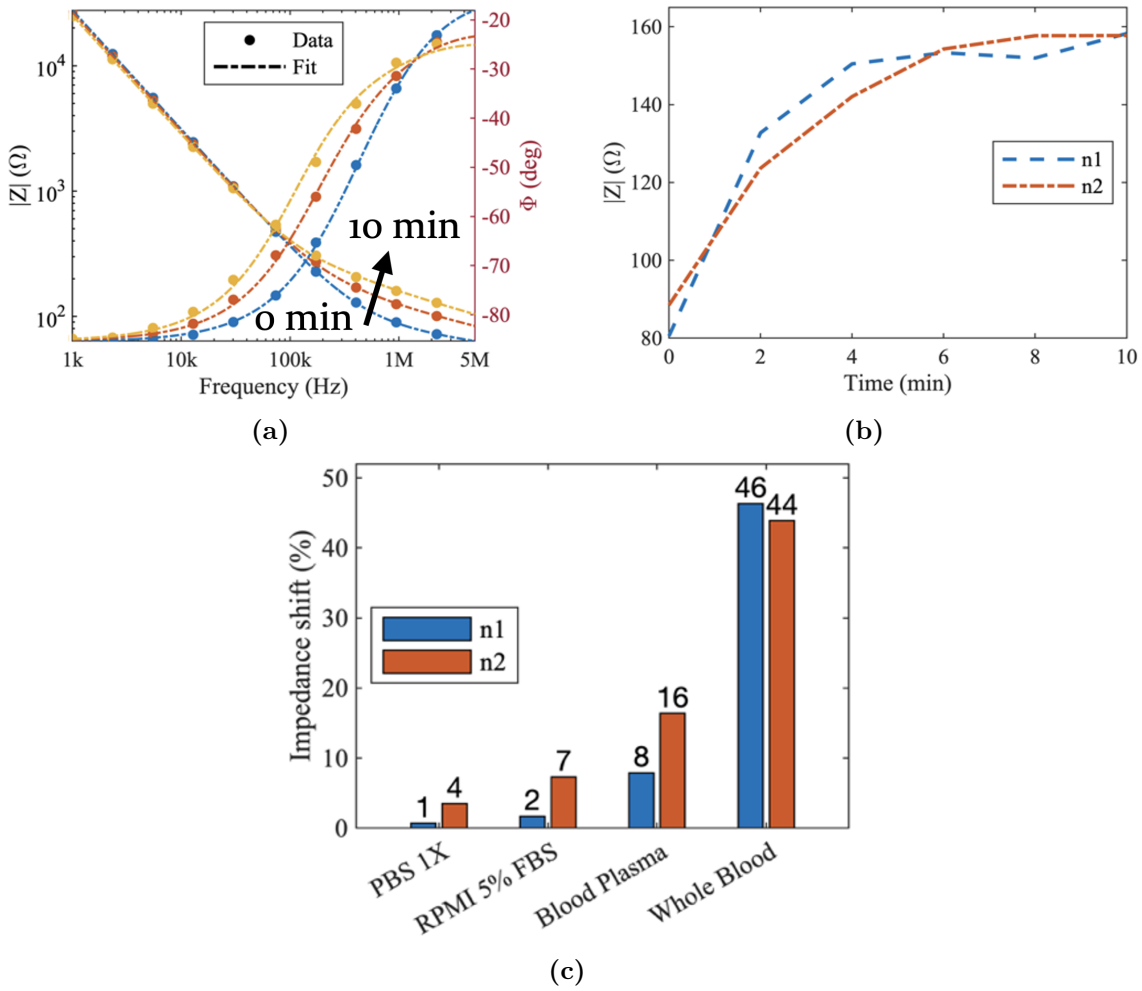

Figure 2.32: (a) Six impedance spectra are measured every 2 minutes for 10 minutes (at 0, 2, 4, 6, 8 and 10 min) along the filtration process of a blood sample through the Cellular Capture and Detection Device, three of them are shown in the figure at 0 min, 2 min and 10 min (respectively blue, red and yellow). The dashed curves are the results of a fitting based on the equivalent electrical circuit model detailed in Section 4; b. Same measurement data as in panel a. plotting the time evolution of the measured impedance at 1 MHz for two identical independent experiments; c. Comparison of the impedance relative shift at 1 MHz over 10 minutes of sample processing between saline solution PBS 1X, cell culture medium (RPMI 5% FBS), blood plasma control samples and whole blood sample.

Above the cut-off frequency of 100 kHz, the measured impedance provides information about the dielectric properties of the region close to the gaps between the interdigitated microelectrodes. The impedance variation over 10-minute experiments correlates with the capture of white blood cells on the micro-perforated membrane.

Indeed, the device impedance with pure PBS, cell culture medium (RPMI 5% FBS) and blood plasma exhibit comparatively much smaller variations and consequently, the time variation of the impedance observed in blood is not dominated by the electrolyte itself, or by the deposition of proteins, but it originates from the capture of blood cells. WBC capture is validated by optical inspection of the device after 10 min of blood circulation using nucleus staining with Hoechst label. Figure 2.33 exhibits many nucleated blood cells captured by the micro-perforated membrane.

Finally, the equivalent electrical circuit model allows for an accurate description of the impedance spectra and its intrinsic component values evolution supports the detection through an increase of the resistivity between the sensing electrodes. It is also interesting to note that, due to the RC equivalent circuit model, the cut-off frequency evolution, which can be seen on the phase diagram, is tightly linked to the resistive component. Hence, the measurement of cut-off frequency shifts may provide a second way of electrical detection. The equivalent electrical circuit together with modeling of the electrical dispersion of blood samples will be discussed in the upcoming section.

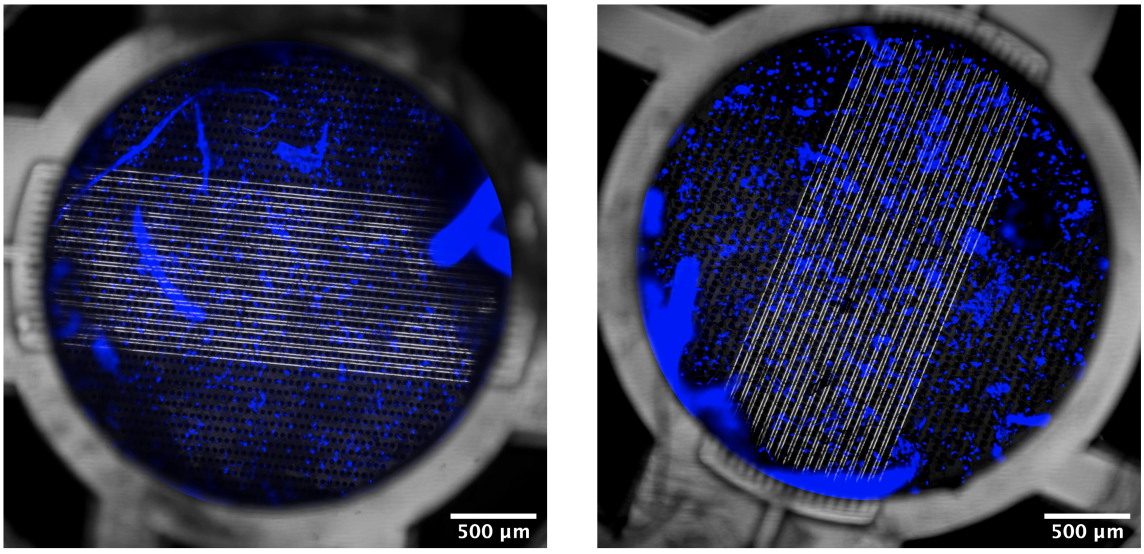

(a) **(b)**

Figure 2.33: Overlay of bright field and colored Hoechst nucleus staining images with 10x objectives (duplicate). Both images are showing the capture and detection device after 10 min of whole blood processing on two identical devices.

Hence, we demonstrated for the first time that the fabricated device can both retain biological elements such as white blood cells while electrically characterizing the cell density over the filtering membrane along the processing of a complex whole blood sample. This result is validated by the processing of control biological samples such

as blood plasma or culture media. Moreover, an electrical equivalent circuit presented in the next section is used to fit the impedance data and will help further electrical study and future device optimization. This contribution to the scientific literature through a publication [82] offers new possibilities for high flow rate processing of biological samples with integrated in-situ electrical characterization of collected cells.

2.3.6 Analytical Description of the Equivalent Circuit Model

Experimental characterization of the microfabricated devices in multiple media allowed for the collection of impedance data. Further equivalent electrical circuit modeling was needed to interpret the collected data on a physical standpoint. Moreover, biological samples are electrically dispersive, which means that their electrical properties vary depending on the frequency. In this section, both the electrical modeling of the coplanar sensor together with the theory of dispersive media will be discussed. The final objective is to combine the previously mentioned aspects into a unified equation, therefore allowing the interpretation of experimental data together with predicting the sensor behavior both in simple and complex media for future design optimization.

As discussed in chapter 1, models were developed to account for the specific geometry of coplanar interdigitated sensors together with the interfacial effects. Here, we compare these models together with Finite Elements Methods (FEM, COMSOL Multiphysics Software) simulations with the results presented above. The equivalent circuit model developed previously includes multiple elements for the description of interfacial effects (double-layer capacitance, charge transfer resistance, ...). However, our measurement methods and the sensor design do not allow for measuring all these effects individually.

Indeed, figure 2.32 only exhibits two regimes: a capacitive and a resistive one. Thus, using an equivalent circuit with more than two elements to model our sensor would lead to overfitting. This overfitting is then at the expense of future developments, we therefore limit the equivalent circuit to the two quantifiable elements as shown in figure 2.34.

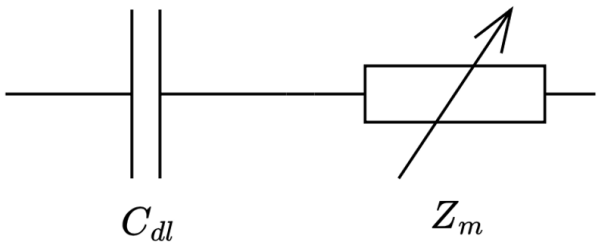

Figure 2.34: Equivalent circuit model for the interdigitated sensors. It is composed of a double-layer capacitance for modeling the interfacial effects and a variable impedance to model the medium and its dispersion.

The interface between the electrode and the medium is reflected through the double-layer capacitance C_{dl} modeled as a constant phase element (or CPE as presented in chapter 1) to obtain the interfacial impedance Z_i whereas the impedance of the medium can be described through its own complex impedance Z_m.

With Z_i the interface impedance (Eq. 2.2) and Z_m the medium impedance (Eq. 2.3), the system can thus be described through Eq. 2.4 for dispersive media. In the case of non-dispersive medium, σ and ϵ_r are assumed to be non-dispersive, i.e. independent of the angular frequency ω.

$$Z_i = \frac{1}{Q_0(i\omega)^n} \tag{2.2}$$

$$Z_m = \kappa \frac{\sigma(\omega) - j\omega\epsilon_0\epsilon_r(\omega)}{\sigma(\omega)^2 + (\omega\epsilon_0\epsilon_r(\omega))^2} \tag{2.3}$$

$$Z = Z_i + Z_m = \frac{1}{Q_0(i\omega)^n} + \kappa \frac{\sigma(\omega) - j\omega\epsilon_0\epsilon_r(\omega)}{\sigma(\omega)^2 + (\omega\epsilon_0\epsilon_r(\omega))^2} \tag{2.4}$$

We can, furthermore, evaluate the form factor of the electrodes κ through Eq. 2.5, as follows:

$$\kappa = \frac{2}{(N-1)L} \frac{K(k)}{K(\sqrt{(1-k^2)})} [\mathrm{m}^{(} - 1)] \tag{2.5}$$

where $\epsilon_r(\omega)$ denotes the real part of $\epsilon^*(\omega)$, while $\frac{\sigma(\omega)}{\epsilon_0\omega}$ is the imaginary part of $\epsilon^*(\omega)$.

Fitting results derived from this model combining the impedance of the coplanar sensor together with the electrical dispersion of the medium are in very good agreement with measurement data for PBS solution, culture medium, blood plasma and whole blood, as it can be observed from figure 2.32a.

Figure 2.35 shows the variation of the interface and medium impedance as a function of time for culture medium and whole blood together with the fitting values of the electrical model (see table 2.3). We observe a good stability over the experiment for the interface impedance Z_i that models the double layer effects, with 4% to 12.7% deviation in culture medium and whole blood, respectively. On the other hand, the medium impedance Z_m shifted by 100% in whole blood and by 7.4% in culture medium.

	Q_0 [F.cm^{-2}.s^{n-1}]	n	κ [m^{-1}]	σ_i [$S.m^{-1}$]	$\Delta\epsilon_r$
0 min	8,86.10^{-9}	0.9505	50	0.63	56; 5337
2 min	9.32.10^{-9}	0.9489	50	0.35	56; 6973
10 min	9.87.10^{-9}	0.9489	50	0.24	56; 6437
with the constants: α = [0.32; 0.32]; τ = [8.38.10^{-12}; 441.10^{-9}]; ϵ_0= 8.854.10^{-12}; ϵ_∞= 4.					

Table 2.3: Fitting values of the equivalent electrical model for three impedance spectra in whole blood.

We herein developed an electrical equivalent circuit that accurately models both interfacial effects and dispersive media. This model allowed further interpretations by enabling independent characterization of the interface impedance. This characterization showed that the sensor is electrically stable while the medium impedance shifted along sample processing, demonstrating the ability of cell density detection over the filtering membrane and within complex samples. This model is also used in the upcoming chapter for the design of a single cell sensor.

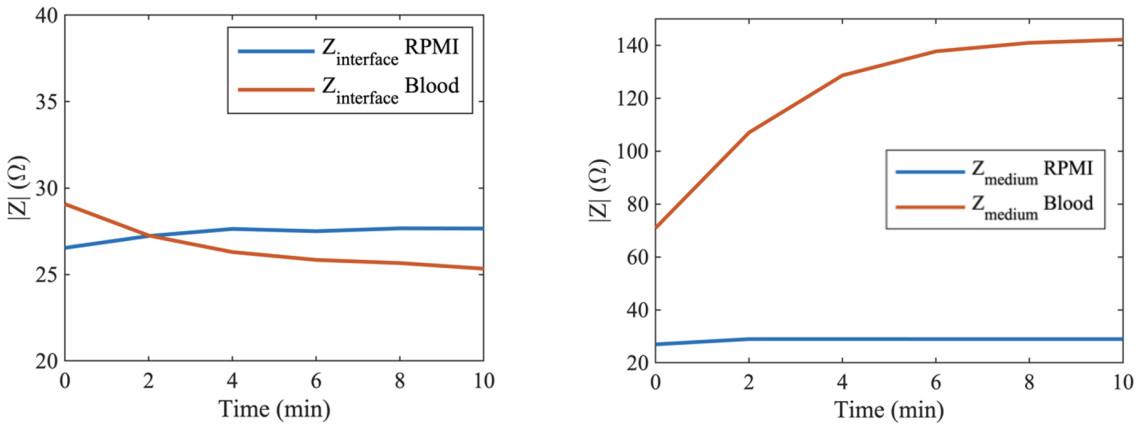

Figure 2.35: Fitting result of the electrical equivalent circuit model for impedance evolution in whole blood and in culture media (RPMI 5% FBS) at 1 MHz over 10 minutes of experiment. (a) Plot the Interface impedance evolution whereas (b) shows the medium impedance.

2.3.7 Electrical Insights in the Capture Kinetics

Following spectroscopic measurements in whole blood, we changed paradigms and opted for a real-time, thus high frequency measurements of the impedance during a blood sample filtration with the aim of characterizing the capture kinetics along sample processing together with electrically detecting single cell capture events through impedance steps.

Although the experimental protocol and platform were kept identical, the impedance analyzer was set to do LCR measurements (i.e. at a single frequency) of the impedance modulus and phase. Changing from spectroscopic measurements to LCR measurements allows for a higher time resolution. A full-impedance spectrum takes in between 2 and 5 seconds to measure, depending on the impedance analyzer settings (bandwidth, precision...) whereas it takes 3.8 ms for each measurement in LCR mode, thus measuring 265 data points per seconds.

Moreover, the frequency behavior of the sensors was well studied in previous sections, showing that the impedance variations are occurring in the region from 100 kHz to 5 MHz. We therefore fixed the frequency measurement at 1 MHz for the following experiments.

Figure 2.36a exhibits the impedance magnitude variation along with 10 minutes of filtration in whole blood. Its shape, a first increase in impedance for the first 4 minutes followed by an impedance plateau correlates with figure 2.32b. It also allows discussing the capture kinetics. Indeed, the increase of impedance magnitude |Z| of the filtering microdevice at 1 MHz during the first 4 minutes of the experiments reveals the capture of WBC by the micro-perforated membrane. After a 4-minute capture phase, a plateau is reached. This plateau can be explained either by the decrease of the electrical sensitivity of the device under cell accumulation, and/or a decrease of the capture efficiency of this device. Indeed, as the number of captured cells increases, the sensitivity could be expected to decrease if the contribution to the global impedance of the next captured cell is lower than that of the previous one. However, electrical simulations performed using COMSOL Multiphysics and cell deposition in between the electrodes of our device did not reveal such an effect. We thus conclude that the plateau correlates to the limit at which the capture efficiency of the filtering membrane tends to zero, although each membrane pore is not occupied. Figure 2.36b shows the capture kinetics evaluated using optical microscopy on a previous design of micro-perforated membrane without integrated microelectrodes. In this experiment, PC3 cells were spiked in culture medium. The number of cells observed on the micro-perforated membrane was recorded in-situ by optical inspection [83]. The obtained results exhibit the same saturation trend between 4 and 10 minutes.

We thus conclude that the integrated microelectrodes can detect and measure in real time the rate of cell capture taking place on the micro-perforated membrane in

whole blood samples.

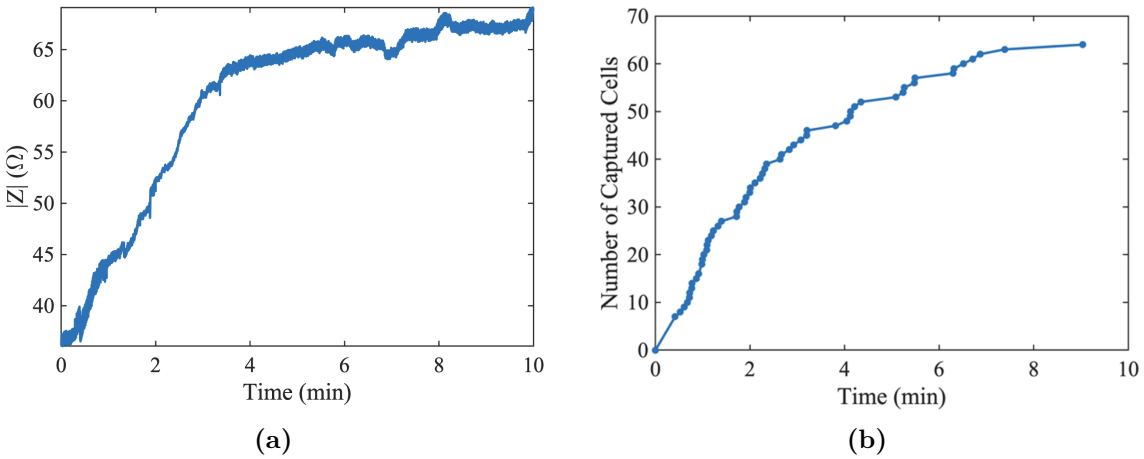

Figure 2.36: (a) LCR Measurement of impedance modulus along with 10 minutes of whole blood filtration at 1 MHz. (b) Cell capture dynamics obtained on a previous microdevice without integrated electrodes exhibiting a membrane of 137 pores.

Furthermore, figure 2.37 shows, in a closer timeframe, the impedance evolution during whole blood processing. Thanks to the high time resolution, two local abrupt impedance changes appear: the most identifiable is the 2-ohm step increase at 114s then followed by multiple and periodic downward spikes in between 115 and 120 s.

These local impedance variations may be due to a single event of cell capture on the filtering membrane. However, the encapsulation of the microdevice in the fluidic channel does not allow for live optical characterization, thus forbidding the validation of such assumption. Modifications in the experimental platform would be needed to be able to obtain an optical confirmation which could then be correlated with an impedance step increase during a single cell capture event.

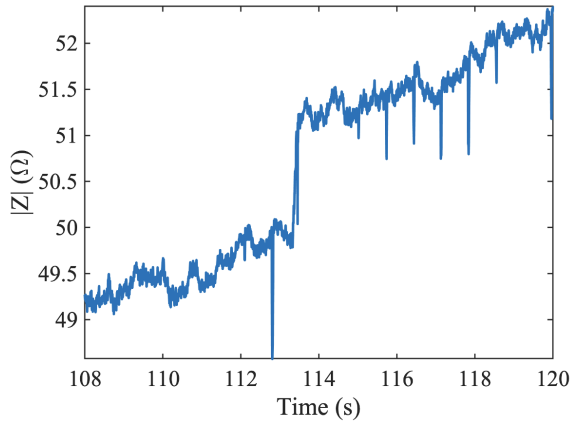

Figure 2.37: Focus on a 12 second timeframe with multiple behaviors: periodic and non-periodic high and low steps.

Finally, looking at the periodic elements within the signal which can be seen when flowing PBS in the system (see figure 2.38a) we make the hypothesis that these periodic variations are coming from the peristaltic pumping system which, as presented in Figure 2.39b, uses 3 cams (in red) on a rotative head to push the fluid through the tubing by inducing local compression of the latter. Indeed, this assumption is confirmed by the Fourier Transformation (FFT – Fast Fourier Transform) of the impedance signal, breaking it down into a combination of sine waves of different frequencies. Figure 2.39a shows the frequencies involved in the signal represented in figure 2.38a together with its harmonics: 1.4 Hz, 2.8 Hz, 4.2 Hz ... which is correlated to the rotation speed of the pump: for a flow rate of 11.5 mL/min, the pump spins at 30 rotations per minutes with 3 cams, thus leading to a pump frequency of 1.5 Hz. Moreover, the signal presented in figure 2.38b was observed following the passing of a bubble through the filtering device, thus inducing an impedance increase due to the medium change from a conductive electrolyte to an electrical insulator.

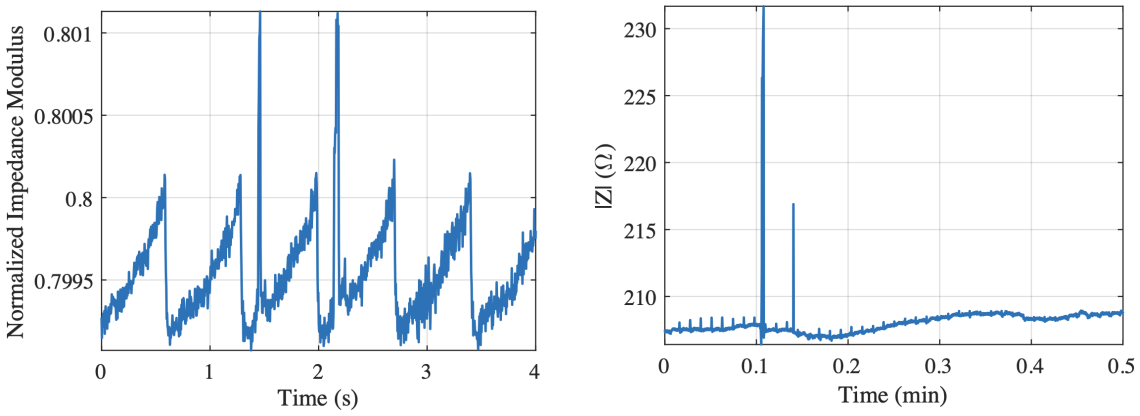

(a) **(b)**

Figure 2.38: LCR Measurement of impedance modulus along PBS filtration at 1 MHz with a periodic variation (a) and two local impedance spikes (b).

Altogether, these results show that the device is sensitive enough to characterize the biological accumulation on the filtering membrane along sample processing. Impedance steps which may be induced by single cell capture events were observed, but modifications in the experimental platform are required to optically confirm the correlations between these steps and capture events. On the other hand, the in-situ electrical measurements allowed the characterization of the pulsatile fluidic effects induced by the peristaltic pump, together with the introduction of air bubbles in the system. Therefore, the microfabricated devices may also bring an understanding of the capture conditions within the enclosed system along sample processing.

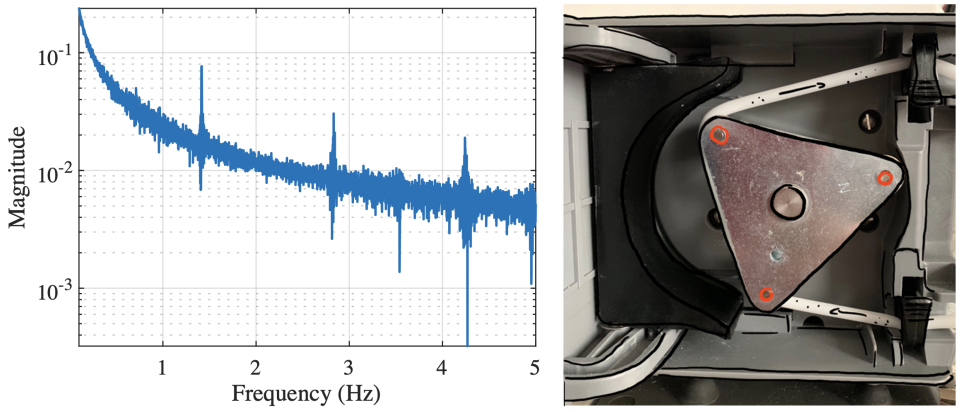

(a) (b)

Figure 2.39: Fast Fourier Transform (FFT) of the signal displayed in figure 2.38 with a peak at 1.5 Hz which corresponds to the rotation speed of the peristaltic pump (b) with the spinning head surrounded by the fluidic tubing and the three cams on the red spots.

2.4 Conclusion and Perspectives

Following the fabrication of devices for in-situ evaluation of cellular density on a filtering membrane, conclusions can be drawn regarding the fabrication process optimization, the experimental platform together with the limitations of the sensor and the future developments towards real-time in-situ sample analysis.

2.4.1 Fabrication Process

As mentioned in section 2.2, optimizations were achieved to stabilize the fabrication process and increase the yield of electrically functional devices. The two critical elements are the electrodes and the filtering membrane.

Regarding the sensing electrodes: sharp angles in between the connection tracks and the contact pads were removed and replaced by slowly widening tracks. Also, the change of electric insulator, from polymers (DF) which were inducing constraints on the access lines when heated, to ceramics (SiO2, SiNx), which are more stable but requires to be etched through plasma. Following these two improvements, as long as the membrane was intact (i.e. it was still supporting the electrodes), every single electrode was functional whereas, using the previous fabrication process led to only 1 out of 6 devices with intact membranes being electrically functional.

The filtering membrane is thin (1.4µm) and its stability is due to the ratio of SiO2 to SiNx which is 800 nm to 600 nm, respectively. However, the last process step which consists of the etching of the silicon substrate in a Hydroxide Potassium solution for 5 hours, also etches SiO2. Although it is at a slower rate, if the ratio is not kept constant, the constraints do not compensate anymore and the membrane

becomes too fragile for proper manipulation and the subsequent seed layer etching steps that were done manually, one device at a time. A specific handler was designed to protect one face of the wafer from the etchant, while keeping the backside exposed. Thus, the membrane was not attacked during the last step. However, this step still releases devices which are then roaming freely in the solution, thus exposing the thin membrane to etchant, and potentially breaking the filtering membrane by colliding with other devices.

Even though single steps of this process are not challenging, the difficulty lies in the succession of each step. The complexity of the technological process is mainly due to the use of multiple and different materials, which in turn relies on different patterning techniques thus increasing "small steps" (such as seed-layers etching, rinsing...). However, the yield of the whole fabrication process is driven by the last critical process step: the release of the devices followed by manual etching of all devices seed layer one at a time. The yield of this fabrication process is around 30% of electrically functional devices, which translates to 30 devices, 5 devices per design.

2.4.2 Towards Real Time Single Capture Event Detection

As discussed in section 2.3 and confirmed later with experiments with microspheres and whole blood samples, the best performing electrode design is the hybrid one. Indeed, although the rectangular design met the criterion of frequency bandwidth, it showed a larger basal impedance which, in turn, lowered the relative variation of the impedance in presence of microspheres, and allows for the real-time evaluation of the cell density on the membrane. Moreover, high temporal resolution LCR measurements allowed to go further and brought insights into the capture kinetics, broadening the potential of these devices for real-time characterization of the cell capture conditions. However, limitations in the current experimental platform does not allow to confirm the real-time detection of single cells capture events. Achieving such validation would open doors to live detection and in-situ characterization of trapped cells based on their electrical signature.

2.4.3 Usability for Liquid Biopsy

As mentioned in chapter 1, a direct application of such devices is turned towards liquid biopsy applications. The membrane of the fabricated device is designed in terms of pore size for retaining nucleated blood cells. However, leukocytes overlap in size with Circulating Tumor Cells, it is therefore possible to trap these rare cells on filtering membranes and, with pore size, shape and disposition optimization, reduce the peripheral nucleated blood cell contamination. The developed cleanroom fabrication process is well suited for both large batch device production and device optimization through prototyping. To improve the capture efficiency of rare elements, it may be

useful to increase the number of devices in series and in parallel. In such case, an electrical detection of the cell density over the membrane for a multidevice capture shell system would bring useful insights about the filtration rate and completion, especially in clinical environments where sterility needs to be kept throughout the process so as to not tamper with the sample or keep the environment safe for the patient. Moreover, we demonstrated that the device with integrated electrodes allows for a live monitoring of the capture conditions (flow rate stability and bubble detection) within an optically closed system. Following the proof of concept, further characterization experiments on many samples would establish a relationship in between the impedance shift and the filter occupation. Finally, the integration of this device in a see-through experimental platform may help understand fluidic effects and their respective impact on impedance measurements (see figure 2.37), and therefore bring impedance characterization to enclosed systems for in-vivo applications.

3 Towards *in-situ* Single-Cell Analysis and Phenotyping

3.1 Device for *in-situ* Electrical Sensing Combined with Imaging Characterization

Following the principle of in-situ electrical detection of biological elements and the technological developments presented in chapter 2, we herein aim to extend the functionalities of microfabricated devices to cell in-situ analysis and phenotyping. Therefore, two devices will be presented in the following section, each with a different fabrication approach together with an instrumental platform combining their electrical, fluidic, and optical integration within a microfluidic 3D printed chip. Although designs and fabrication processes differ from the ones presented in the previous chapter, the fabricated devices are still based on two essential technological elements: the electrosensitive element and the membrane that isolates the elements of interest from the biofluid.

3.1.1 General Structure of the Analytical Device

As introduced, two devices will be presented in this chapter. They will be referred to as the silicon devices and glass devices. Their main difference is the substrate and supporting structure, which are either made of silicon or glass.

Chapter 1 described the concept of developing a broadband sensor for dispersion analysis and its implications regarding the design of the sensing electrodes. As commented in this chapter, in order to increase the sensitivity of the new sensors, widen the frequency band and limit undesirable effects, an optimization was led and is presented in the section 3.6 of the present chapter.

However, the global concept of a filtering membrane with sensing electrodes is kept identical as the device presented in chapter 2. As so, the structure can be declined in three parts: the filtering membrane, the sensing electrodes and the supporting

structure.

The supporting structure, which was grown by electroplating on the previous devices, is herein defined through subtractive pattern transfer techniques (etching) directly within the substrate. This new fabrication paradigm allows to both, remove the final step of liberation of the membrane which was a considerable bottleneck of the process yield and, by using the substrate as the supporting structure, use non-conductive materials such as silicon or glass instead of nickel.

However, such a change from an additive (deposition) to a subtracting (etching) approach also implies drastic design modifications. Indeed, since the bilayer membrane is grown on top of the substrate, the supporting structure will therefore be standing below the membrane or, in other words, the membrane will be on top of the supporting structure. It will therefore move the fluidic canal created by the supporting structure under the membrane and may impact the fluidics and capture the kinetics of our devices. This point will be discussed in 3.5.1.

In the specific case of glass devices, the fabrication process will use a 2-photon micro structuring technique, thus allowing for a three-dimensional control of dimensions. Therefore, the supporting structure and the previously called membrane will be fabricated in a single monolithic structure (shown in figure 3.1), thus leading to the filtering part being as thick as the supporting structure (300µm). The term “sieve” may be more appropriate to describe such a filtering structure instead of the term “membrane” used in the previous conventional 2D surface micromachining process.

Finally, the fabricated devices are to be integrated in a 3D printed microfluidic chip providing a fluidic, optical and electrical access to the membrane and sensing electrodes. To do so, the supporting structure was enlarged to a 1 cm square shape, allowing the relocation of electrical contact further away from the filtering zone, thus leaving a comfortable margin for the 3D printer to design the fluidic canal and holes for contact pins insertion.

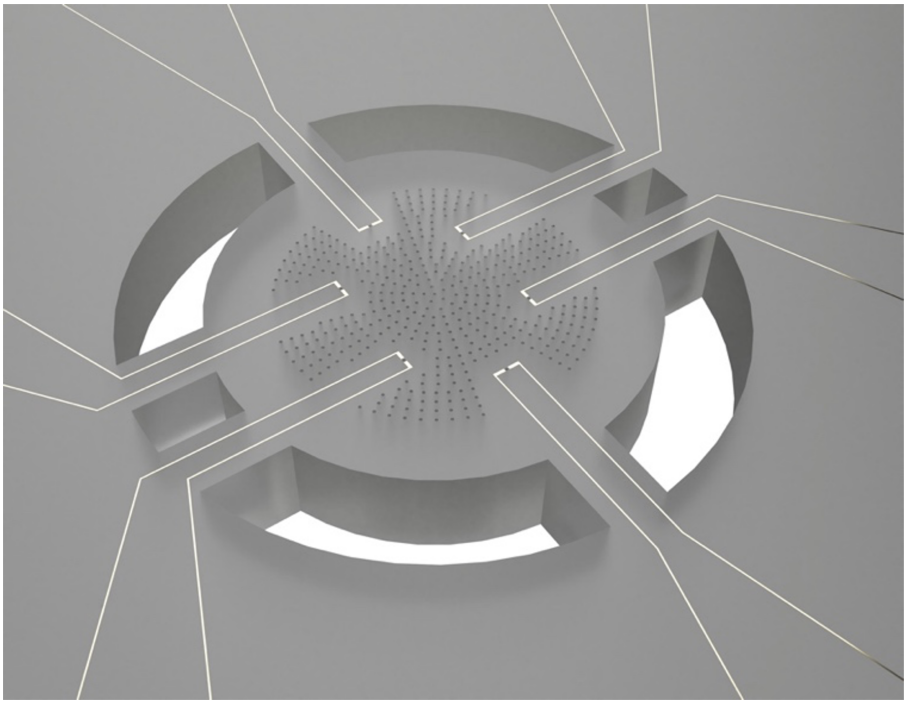

Figure 3.1: 3D CAD representation of the glass devices with the supporting structure and central sieve with electrodes on top.

3.1.2 Geometry of Electrodes

The silicon and glass processes use both the same electrode geometry with the same exposure masks. These electrodes were designed to favor the sensitivity and bandwidth of the sensor while avoiding undesirable electrical capacitance effects.

Since the concept of cell analysis is applied at the single cell level, sensing electrodes surround a single capture pore. However, to increase the probability to capture a single cell in between the electrode pair, the electrode pattern is repeated, thus giving 6 electrodes pairs indexing 6 pores of the membrane. This limitation in the total number of connected pores is due to the size of contact pins which will be used to make electrical contact with the microfabricated device.

Finally, the retained electrode geometry is presented in figure 3.2 showing the 12 lateral contact pads (680 µm in diameter), the access tracks (4µm width) and sensing electrodes on the membrane. The electrode configuration around a pore, as shown in figure 3.2c and d, is defined by an area of 20 µm by 10 µm uncoated by the insulating layer. This exposed or sensing area is the same for the 6 electrodes, even though the insulator design varies. Indeed, among the 6 electrode pairs, four arbors the design shown in figure 3.2d showing "standard" electrode insulation, whereas 2 electrode pairs follow the design presented in figure 3.2c where the insulator surrounds the indexed pore to create a well in which the cell can be captured.

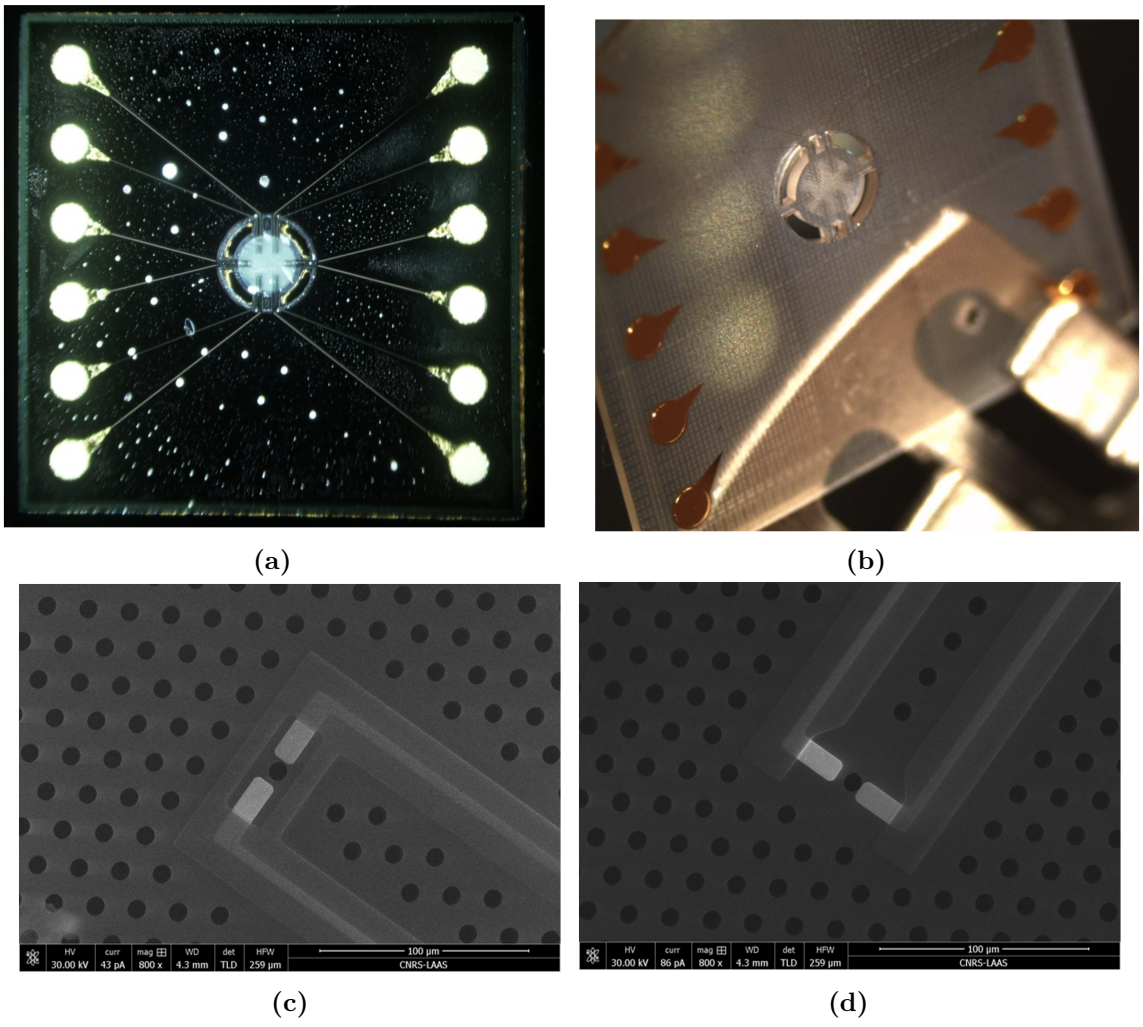

(a) **(b)**

(c) **(d)**

Figure 3.2: Silicon (a) and glass (b) microfabricated devices showing the contacts pads on each side with access tracks leading to the filtering structure in the center. c and d SEM Micrographs showing the two insulator designs surrounding the indexed pore for c) and standard configuration for d) for a silicon device.

3.1.3 Device Integration

Along developing new processes, we also aim to improve the experimental platform presented in chapter 2. Indeed, many aspects needed to be addressed, the most important one being that the system was optically closed. Therefore, electrical measurement could not be optically monitored and needed to be confirmed a posteriori through multiple control experiments.

We address this issue among others in this chapter where we present a 3D printed microfluidic chip allowing the integration of the microfabricated device in a fluidic canal while allowing for optical and electrical accesses to the filtering structure. This addition is made possible thanks to recent process development in stereolithography 3D printing which will be described.

Finally, this integration enabling the use of live microscopy together with multiple sensing pairs which needs to be addressed individually induces the need for an automation platform both for live experiments or data post-processing.

3.2 Micro-Fabrication Process

The fabrication process reported here was elaborated from the fabrication and experimentation achieved on the devices for cell density detection that are presented in chapter 2. The major bottleneck in terms of yield of the previous process was the last technological step, namely the substrate wet etching for device release. Hence, these new processes intent to overcome these issues while reducing the fabrication time and resources.

3.2.1 Silicon Process

The first process based on previous developments (*i.e.* the filtering membrane and the electrodes) was established. The main modification from the process presented in chapter 2 is the supporting structure. Indeed, instead of being grown by electroplating which induces a final step of releasing the devices from their substrate, here, the supporting structure is etched within the silicon substrate. This process, apart from the nickel electrolytic growth, keeps the same materials and fabrication techniques as presented in chapter 2 and yields to a new technique named the Silicon Deep Plasma Etching.

Specific Fabrication Technique: Deep Plasma Etching

The new technique, called the Bosch process for silicon deep etching, alternates passivation and etching cycles by switching the nature of the gas species forming

the plasma, as illustrated in figure 3.3. The SF_6 plasma cycle etches the silicon material, while the C_4F_8 plasma passivates the surface including the vertical edges of the structures by depositing a thin fluorocarbon polymer layer. The bottom part of the passivating polymer layer is removed with O_2 plasma but leaves the passivation layer on the edges of the structure in order to protect the edges of the structure during the next SF6 etching cycle and lead the possibility to generate highly anisotropic etching and create very high aspect ratio structures. Note that this alternance of passivation and etching generates scalloped edges, which are characteristic of this deep silicon etching process. Plasma parameters used for the process are given in table 3.1.

Gas	Flow rate	Time	RF Plasma	LF Polarization
SF_6	700 sccm	3s	2300W	85W
C_4F_8	350 sccm	3.5s		
O_2	200 sccm	2s		

Table 3.1: Plasma parameters for Bosch etching process.

This process step forms the silicon supporting structure of the devices, the last step of the fabrication process requires optimization. Indeed, due to an almost 2:1 aspect ratio of the side openings (250µm wide for a depth of 500 µm), this part of the design is etched slower than the membrane's canal which has a ratio of 1:2.5. Moreover, the stopping layer of the backside etching is the 1.4 µm bilayer membrane, which is also etched, even though at a smaller rate, by the plasma. Thus, due to the difference of the ratio, the canal was fully etched with the membrane exposed to the plasma while the side openings were not perforated. In order to fully etch the latter, in between 5 and 10 minutes of over-etching were needed which, in turn, etched through the filtering membrane. To solve this issue, the backside etching of silicon was done in two steps: a first full-wafer backside isotropic etching to thin the wafer from 550 µm to 250 µm. The backside lithography of the fifth layer was then done and followed by the Bosch process described above.

Moreover, to avoid damaging the equipment's chuck by going through the wafer, the latter needs to be "glued" to a second silicon wafer on which the etching will end. However, this process is highly sensitive to temperature, thus, a good thermalization of the etched wafer is needed in between the two wafers to avoid damaging the resist and obtain a homogeneous etching. Due to the topography on the front side (contact pads, insulator...), a thermal paste is used for bonding the two wafers and retaining the devices once separated. Once the etching is done, the final O_2 plasma was done to remove hydrophobic fluorinated compounds, thus allowing for a chemical release and cleaning the devices using peroxymonosulfuric acid (H_2SO_4 + H_2O_2).

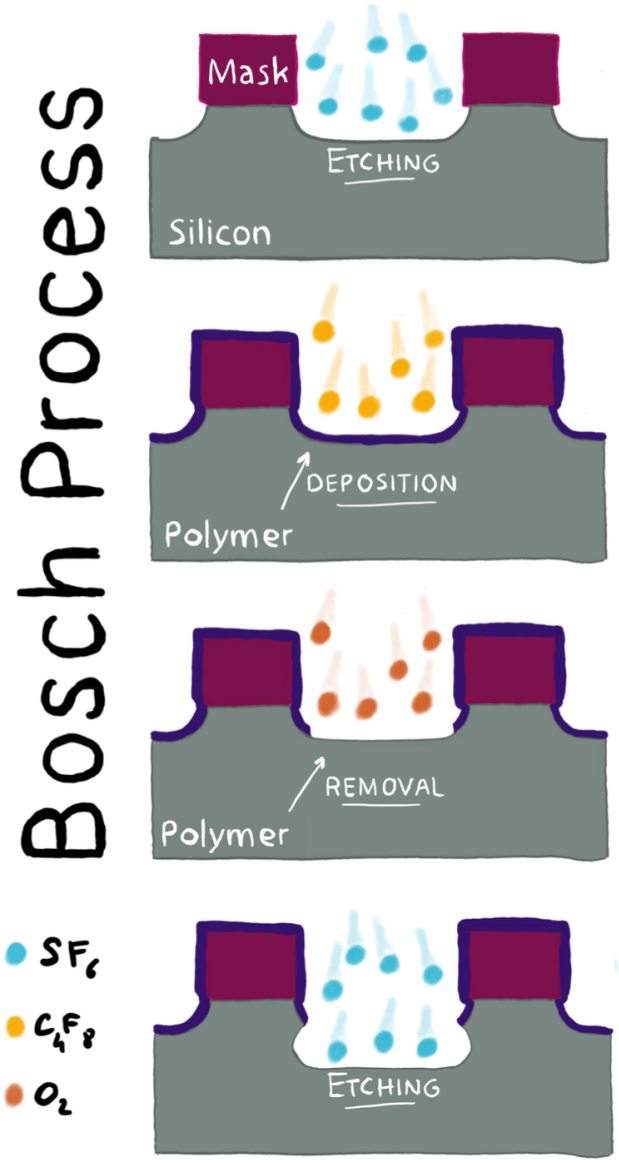

Figure 3.3: Deep anisotropic silicon etching (Bosch Process) working principle.

Microfabrication Process of the Silicon-Based Devices

The design of the supporting structure exhibits a larger imprint, thus reducing the number of devices per wafer to 43. Five mask levels have been designed using Klayout software. The first level (L1) corresponds to the electrolytic growth of the electrical contact pads on the front face of the devices. The microelectrodes, connection tracks and electrical contact pads are defined on the same second level (L2). The insulation of the connection tracks and contact pads is defined on the third level (L3). A fourth level (L4) corresponds to the pores of the filtering membrane centered between the pairs of microelectrodes previously defined and to the lateral openings. Finally, a fifth and last level (L5) forms the silicon supporting part through a plasma deep etching process on the backside of the wafer. Figure 3.4 illustrates the successive stages in the manufacturing process, which is detailed in the Appendix.

Figure 3.4: Schematic representation of the steps in the microfabrication process for devices with integrated electrodes on a silicon supporting structure (diagrams are not to scale).

Characterization of the Fabrication Process

The process is quantitatively characterized at every step using microscopy and profilometry techniques together with qualitative imaging under SEM microscope. As presented in chapter 2, special care needs to be taken during resist stripping at the electrode definition step.

Even though the yield of this process is higher than the one presented in chapter 2 (around 70% of devices are functional), the bottleneck is still the last process step. Indeed, the wafer bonding with thermal paste is done at ambient pressure. Trapped air bubbles in between the two wafers are pulled out in the plasma vacuum, thus lifting one side of the wafer (as it can be seen in figure 3.5a). This step could, however, be improved by using a vacuum press to remove trapped air while bonding wafers. Figure 3.5b shows the released devices after the wet etching of the thermal paste and the resist. Devices which had proper thermalization during the plasma etching process (*i.e.* in the upper part of figure 3.5a) are etched through fluidic slits with the filtering membrane still intact and are ready to be integrated.

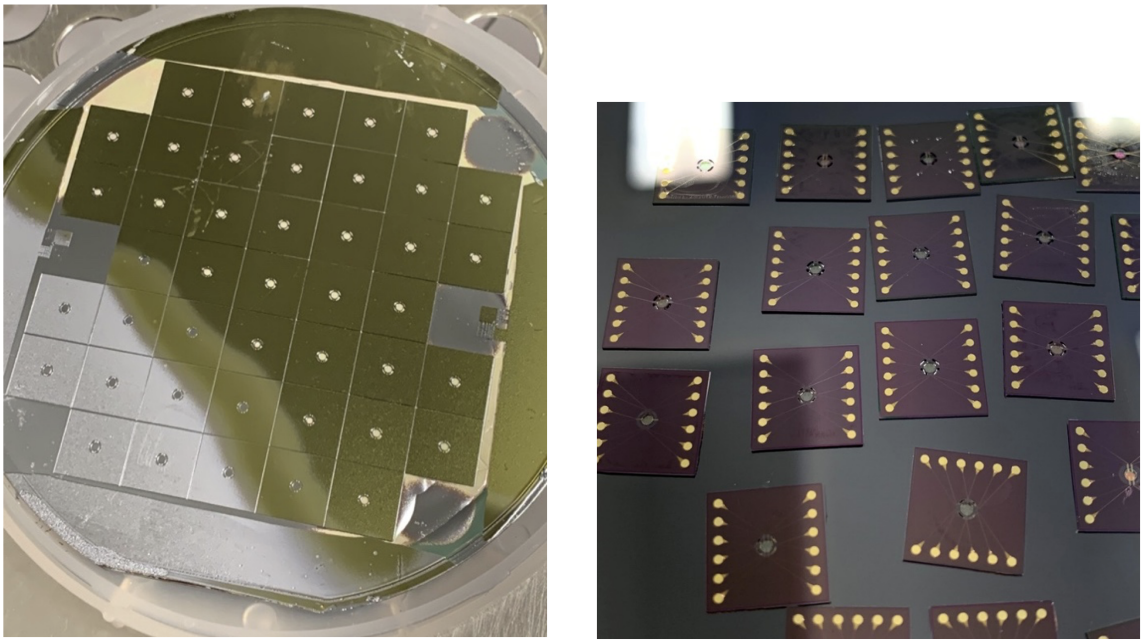

(a) **(b)**

Figure 3.5: Devices after deep plasma etching. a Lifted wafer with the stripped resist on the lower left. Above that line, resist can be seen with thermal paste leftovers in between devices. b Separated devices after a chemical release of the devices from the silicon substrate.

SEM micrographs of the fabricated devices are shown in figure 3.6. We can notice that the membrane is held flat by the silicon supporting structure underneath it, which indicates that it has not been damaged by the silicon etching process and still has its mechanical properties while the four largest fluidic slits are perforated. Moreover, we can see that most of the layers are aligned properly. However, and as it

can be seen on figure 3.8, the alignment in between the sensing electrodes and the membrane pores could be improved (shift of around 1 µm) by tailoring alignment patterns on photolithography masks with smaller alignment gaps.

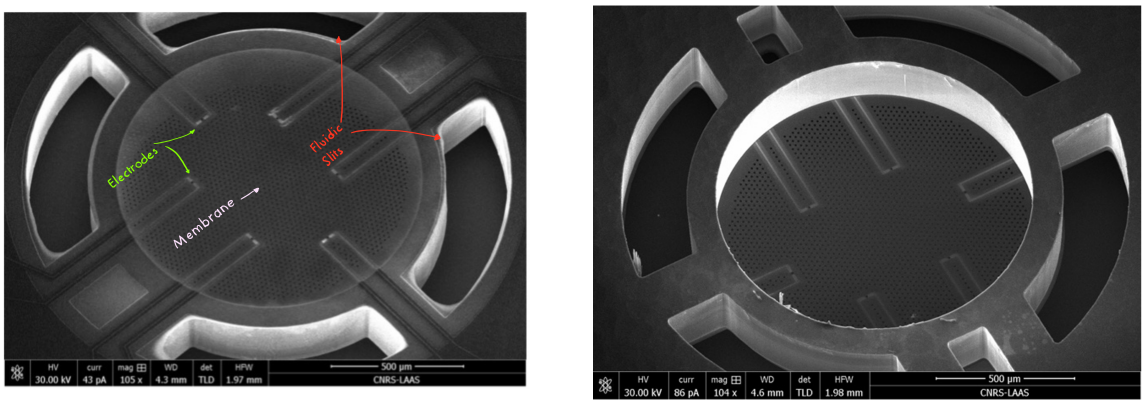

(a) **(b)**

Figure 3.6: SEM Micrographs of the upper (a) and lower (b) sides of the devices.

Taking a closer look at the filtering membrane next to the sensing electrodes (see figure 3.7), we can see the double layer forming the membrane on the side of the pore walls. The pore is well defined, as well as the electrodes which show a smooth surface without granularity.

Finally, the electrodes are well defined (see figure 3.8), and the continuity of the access track is checked using a probe station and an impedance analyzer, taking contact on the contact pad on one side and on the electrode on the other. These measurements allowed us to experimentally characterize the resistance of the access track for the three different track lengths and compare them to their equivalent electrical circuit model, composed of two parallel resistances for the two layers, respectively 100 nm gold and 50 nm chromium (see table 3.2). We can see that these values are relatively low compared to the expected impedance of the electrodes within electrolytic media (kΩ to MΩ), which suggests that the access tracks together with the contact pads do not dominate the impedance value.

	Measured Resistance	**Simulated Resistance**
L1: 4.5 mm	232 Ω	246 Ω
L2: 3.8 mm	191 Ω	208 Ω
L3: 2.8 mm	148 Ω	153 Ω

Table 3.2: Resistance of access tracks for three different lengths: measurement and simulation results.

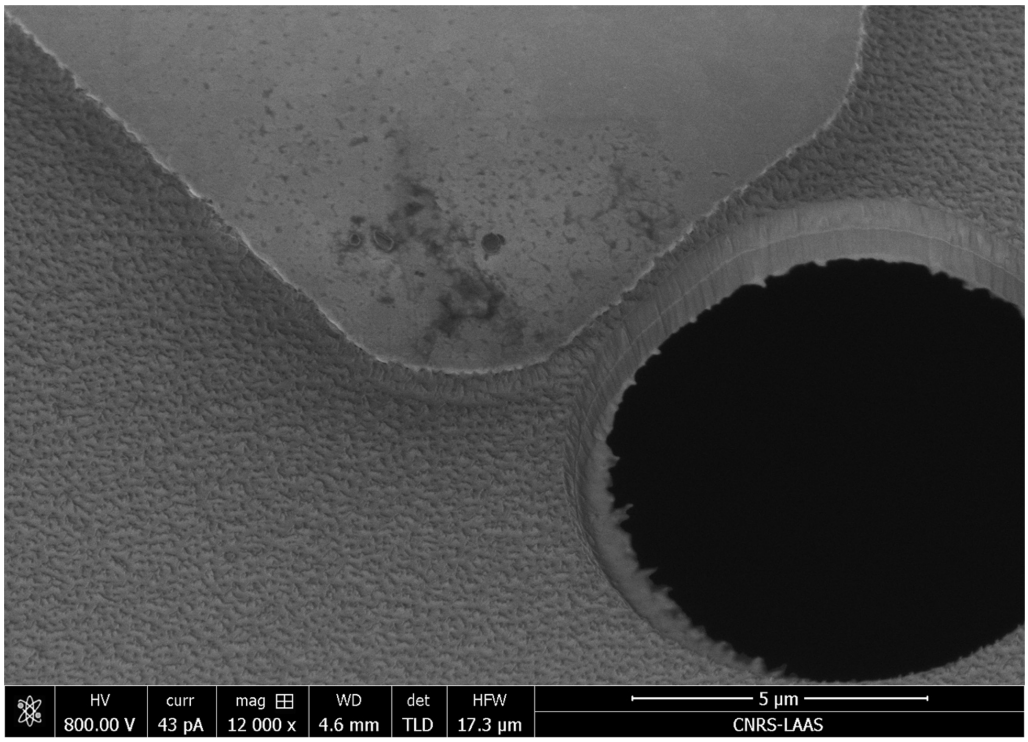

Figure 3.7: SEM Micrographs showing a single pore of the filtering membrane together with a sensing electrode on its side. We can notice the double layer forming the filtering membrane on the pore's wall.

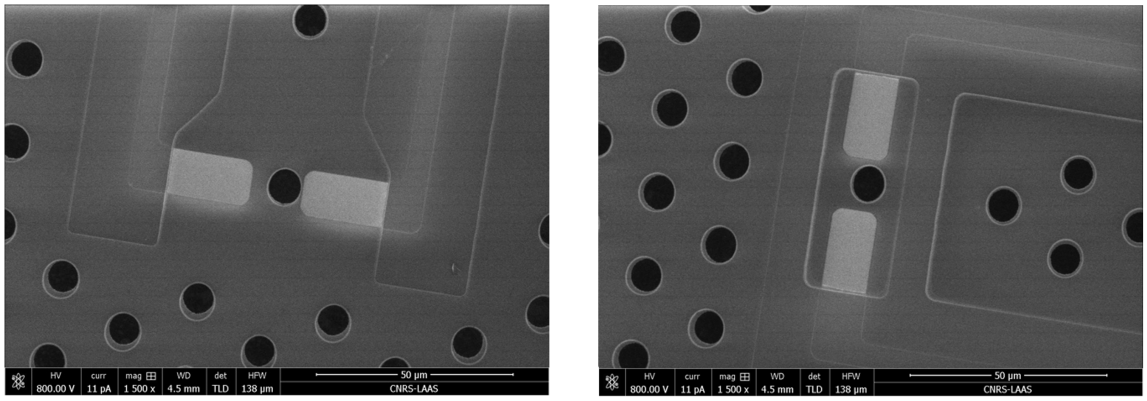

(a) **(b)**

Figure 3.8: SEM Micrographs of defined electrodes on the filtering membrane with the electrical insulator on top which differs: a insulates each track individually whereas b surrounds the electrodes and the capture pore, thus connecting the two insulators.

3.2.2 Glass Process

A second process, was established following the arrival of a new tool in the technological platform. The goal of this process is to simplify the fabrication protocol by reducing the number of steps, together with solving electrical issues induced by the silicon substrate.

Specific Fabrication Technique: Selective Laser Etching

Selective Laser Etching (SLE) is a subtractive laser technology allowing fabrication of complex-shape 3D glass parts with micrometer precision (see figure 3.9). This technology consists of two fabrications steps: femtosecond laser irradiation and subsequent chemical etching. Tightly focused femtosecond laser beam at 1030 nm induces modifications of transparent material within the focal point of the laser beam. By spatially moving the laser focus, the structure is written in point-by-point fashion. Afterward, the sample is immersed in a solution (Potassium Hydroxide) which etches out preferentially laser modified areas.

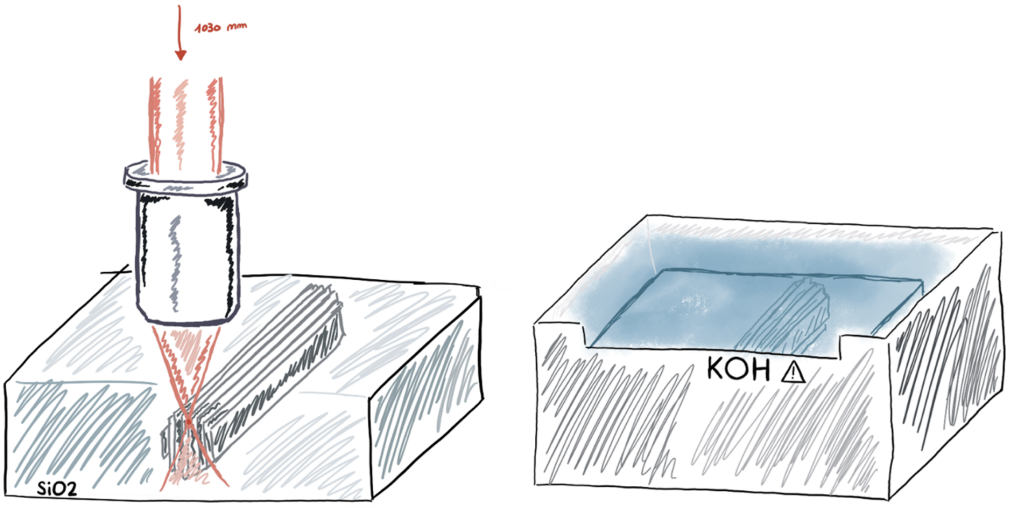

Figure 3.9: Selective Laser Etching working principle. The SiO2 substrate is written by 2-photon laser paths, inducing defaults in the material. These defaults are then preferentially etched in an etchant solution (Potassium Hydroxide or KOH).

The machine used for our process is manufactured by Femtika (Laser Nanofactory). Although the working principle of such techniques is well known, the light-glass interactions inducing the topography (called nanograting) used for SLE are still unclear as of today and deserve to be discussed.

This process is based on the absorption on the highly focused laser spot of 2 (or more) photons, therefore inducing non-linear effects such as multiphoton ionization and tunneling ionization. To be promoted from the valence to the conduction band

by this multiphoton absorption, the electron must absorb enough photons so that the number of photons absorbed times the photon energy is equal to or greater than the band gap of the material. The transition between multiphoton ionization and tunneling ionization is expressed by the Keldysh [84] parameter γ defined as follows:

$$\gamma = \frac{\omega}{eF}\sqrt{m\Delta} \tag{3.1}$$

where ω denotes the angular frequency of the laser, Δ is the width of the forbidden band separating the valence band from the conduction band, e and m designate respectively charge and reduced mass of the electron and the hole and F is the electric field magnitude. Finally, when the Keldysh parameter is $\gamma < 1.5$, photoionization is a tunneling process. In the intermediate regime, the photoionization is a mix between tunneling and multiphoton ionization, as depicted in figure 3.10.

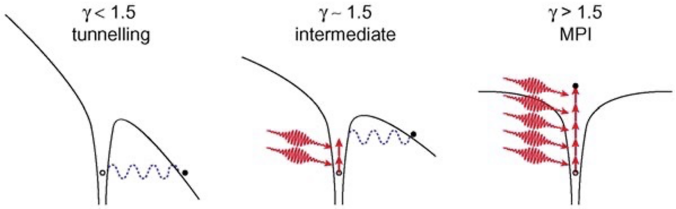

Figure 3.10: Schematic diagram of the photoionization of an electron in an atomic potential for different values of the Keldysh parameter. In a solid, the electron is promoted from the valence to the conduction band, rather than ionized. From Chris B Schaffer et al. [85].

Light Glass interactions can induce different types of modifications, as shown in figure 3.11 where (a) is unprocessed glass, (b) and (c) show smooth positive refractive index modification (Type 1) and (d) displays topographical modifications (Type 2) through the creation of so-called nanogratings shown in Figure 3.12. These modifications strongly depend on the combination of pulse duration and energy together with the numerical aperture (NA) of objectives.

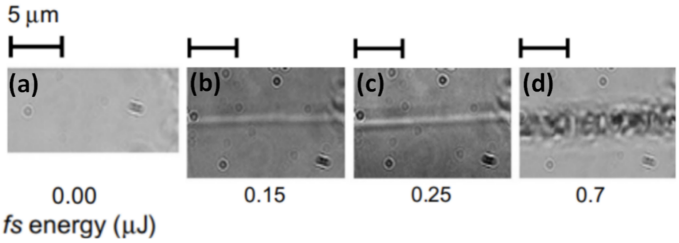

Figure 3.11: Glass modification examples. (a) unmodified material, (b,c) type I of glass modification or refractive index changes. (d)—type II modification or nanogratings. From C. Hnatovsky et al. [86].

Figure 3.12 shows the impact of light polarization angle on the formation of nanogratings. A light polarization perpendicular to the scanning direction (Figure

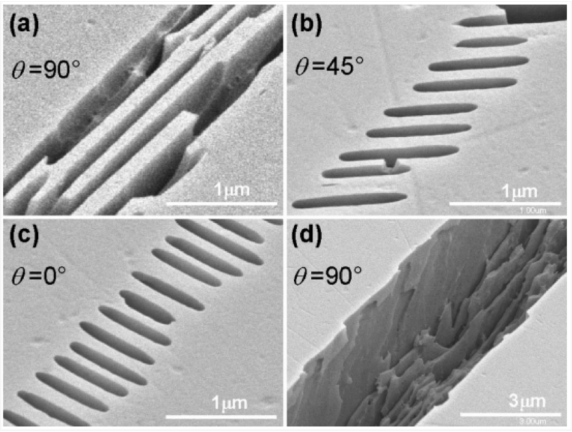

Figure 3.12: Examples of type II glass modification and visualization of nanogratings direction dependency to light polarization. (a) Nanogratings induced with light polarization perpendicular to scanning direction- the angle between polarization and scanning direction 90°, (b) 45° and (c) 0°. (d) Nanogratings modification after etching. From C. Hnatovsky et al. [86].

3.12a) induces nanogratings in line with the scanning direction and therefore perpendicular with the light polarization. The opposite effect is shown in figure 3.12c with 0° polarization angle. Following a 90° polarization laser writing and wet etching, figure 3.12d shows the etched line with nanogratings residuals at the bottom. The interpretation regarding the formation of periodic nanogratings is linked to interferences between the incident light field and the electric field of the bulk electron plasma wave, resulting in the periodic modulation of electron plasma concentration [87].

Moreover, figure 3.13 shows the impact of the writing polarization on the subsequent wet etching rate where circular and 90° polarization led to the highest etching rate.

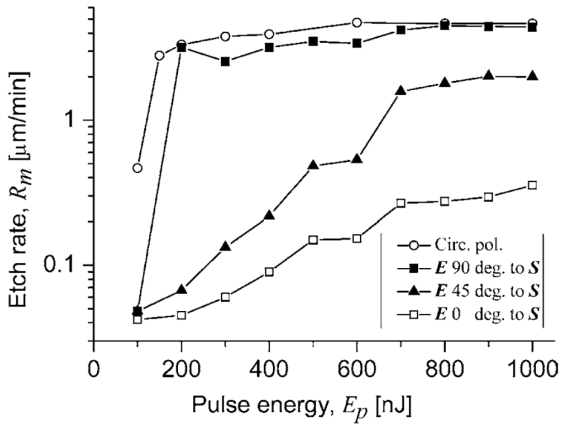

Figure 3.13: Polarization-selective etch rates for the transverse writing geometry. From C. Hnatovsky et al. [86].

Finally, as described previously, the theory surrounding light and electron interactions is well understood thanks to the work of L.V. Keldysh in 1964. The induced

damaged by laser-writing together with subsequent wet etching in different conditions (etchant, energy, polarization...) are also well documented and machines using this principle commercialized. However, the principle of atom displacement following electronic excitation, which is at the core of this technology, is still not well described and multiple contributions could lead to the creation of defaults in the material.

The Coulomb explosion mechanism is used for material ablation at high laser power. However, within the lower laser power range used for SLE processes, the main contribution comes from inelastic electron-phonon scattering which transfers the electronic excitation energy to the lattice, which is then heated up, exceeding the melting point of the material. Moreover, the electronic excitation may weaken the covalent bonds and causes a repulsive force between atoms, thus creating an instability in the atomic structure and displacement of atoms [88].

Application of Selective Laser Etching in our context

This technique can be qualified as a fast-prototyping technique in the way that designs can be adapted and fabricated faster than using standard cleanroom fabrication methods. Indeed, the workflow uses CAD designing to generate a 3D model which is then converted by a proprietary software into laser paths.

In our case, the glass substrate on which the writing is done needs first to be thinned down from 500 µm to 300 µm. In order to do so, the SLE software writes cubes which borders are then etched, thus detaching whole cubes of substrate for faster etching. This step, however, leaves the back side of the device with a rougher topography as shown in figure 3.14 exhibiting leftovers of the square matrix.

Since the method is based on wet etching, the difference in size of the different parts which are to be etched needs to be considered when designing the structure. Indeed, 3 µm diameter pores are nominally written but, due to the over-etching of the filtering structure needed to etch the larger design parts (fluidic slits, substrate thinning), 10 µm diameter pores are finally obtained. A general rule of thumb for taking into account this over-etching is at a rate of 1 µm per 100 µm of substrate thickness or 1 hour of etching. As an example, a 500 µm substrate needs approximately 5 hours to etch, thus, a 1 µm diameter written pore design will end up being 5µm in diameter. This approximation then needs to be refined through iterations.

Regarding our specific design, the parts that need to be etched are either large: the whole substrate surface during substrate thinning and the side slits (200 µm wide approximately); or really small: 3 µm for the pores of the filtering membrane. This simplifies the laser trajectories as it will only write outlines, therefore lowering the writing time to 2 hours. This technique also lowers the etching time to 3 hours in a KOH solution at 80°C.

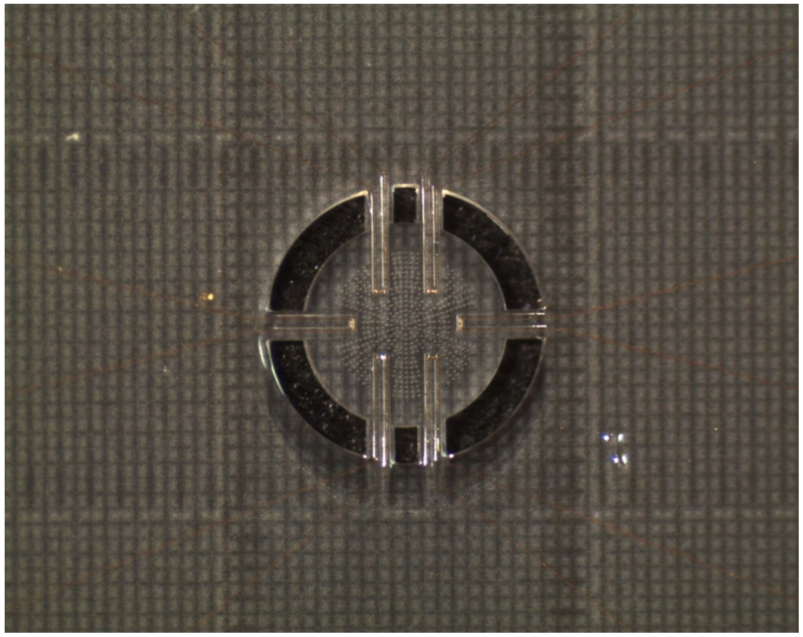

Figure 3.14: Focus on the central part of glass devices showing, in the background, a square matrix due to the substrate thinning technique.

Microfabrication Process of the Glass-Based Devices

Figure 4 illustrates the successive steps of the manufacturing process (details are given in the Appendix. The design of the supporting structure keeps the square shape described in the silicon process. With the use of the SLE technique for defining the membrane together with the supporting structure, only three masks, which have been designed using Klayout, are needed for this process. The SLE process is divided into two steps: a first step writes the 3D structure within the glass substrate, then, after fabrication of the gold microelectrodes and their electrical insulation, are etched in a KOH solution to selectively etch the written parts. In that sense, the 3D structures are only revealed at the last stage of the process. The first mask level (L1) corresponds to the electrolytic growth of the electrical contact pads on the front face of the devices. The microelectrodes, connection tracks and electrical contact pads are defined in the second level (L2). The insulation of the connection tracks and contact pads is defined in the third level (L3).

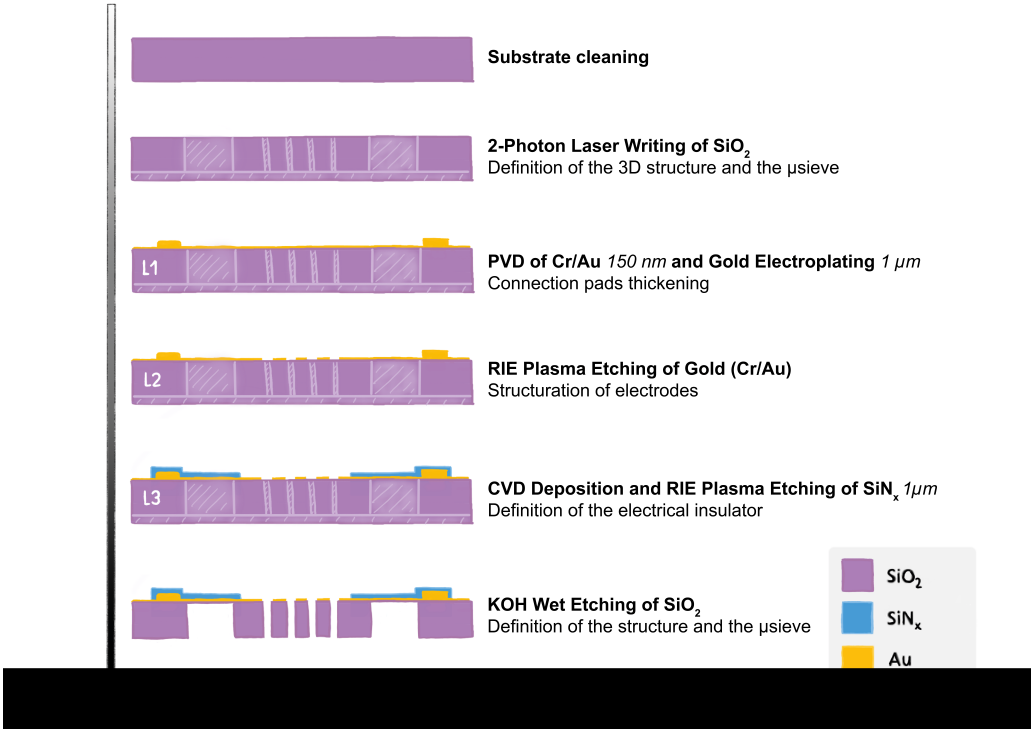

Figure 3.15: Schematic representation of the technological steps of the microfabrication process for devices with integrated electrodes on a glass supporting structure. Diagrams are not to scale.

Characterization of the Fabrication Process

The first characterization step is performed after the 2-photon laser writing. Indeed, although the structure is still embedded within the bulk of the substrate, the laser creates nanogratings together with a refractive index modification inducing dark lines when observed under a microscope (see figure 3.16). Moreover, since our design is symmetrical by translation on the z-axis, the microscope observation allows for the verification of the conformity of the design dimensions at the surface of the substrate which should be identical to the ones written in the lower layers, within the substrate bulk.

Following this characterization, conventional optical microscopy and mechanical profilometry are used to verify resist thicknesses and dimensions of transferred electrodes and insulator designs. However, due to the laser writing, mechanical constraints are induced in the 3x3 cm substrate which is slightly bent. It therefore impacts the following photolithography steps needed for the electrode and insulator definition through a poor mask/substrate contact, thus bringing alignment difficulties together with a poor thermalization when doing the resist baking and post exposure baking. Although the alignment of the 2 layers regarding the filtration pores is good, these effects created ripples both on the electrode and insulator definition as shown on figure 3.17. Further resist process optimization would be needed to obtain perfect

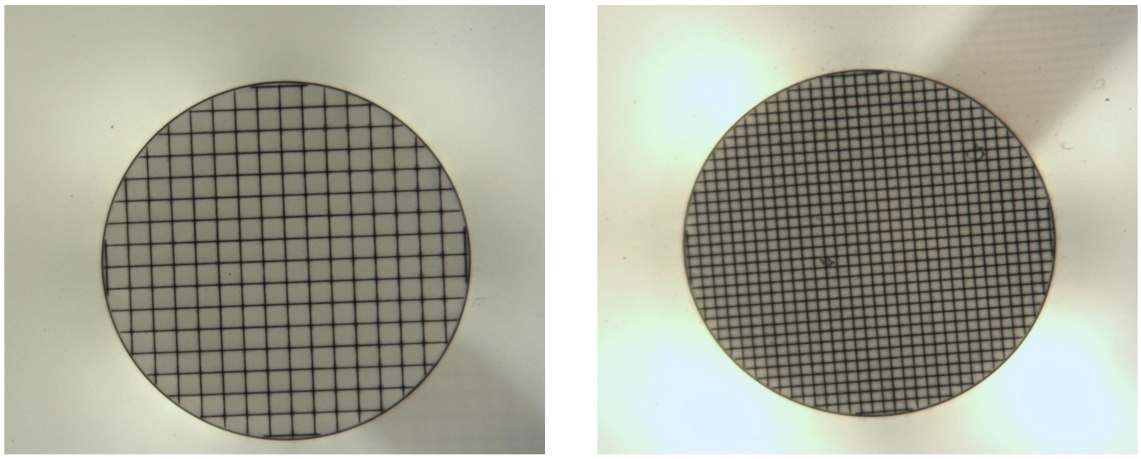

(a) **(b)**

Figure 3.16: Bright Field Microscope images after SLE writing on a glass substrate. A circle of 1.6 mm is filled with hatching cubes of 100 µm (a) and 25 µm (b). The dark lines are due to laser paths inducing refractive index change together with topographical modifications. From D. Bourrier.

photolithography steps following an SLE laser writing, however, in our case these imperfect edge definition of the metallic and insulating patterns did not impede the functionality of our device in the context of this thesis research.

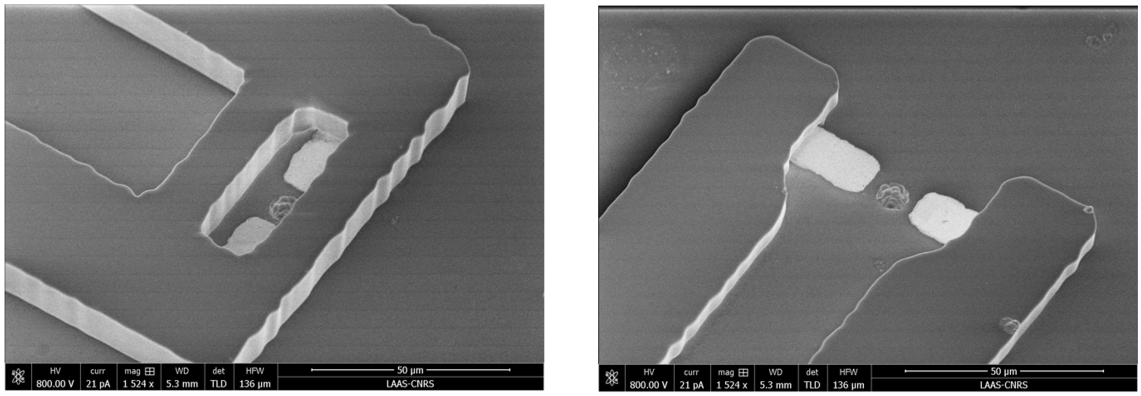

(a) **(b)**

Figure 3.17: SEM Micrographs showing the sensing electrodes and the insulator surrounding a single capture pore. Both the electrodes and the insulator show ripples due to poor lithography steps induced by the bending of the glass substrate.

Finally, qualitative SEM imaging is achieved to evaluate the overall state of the device after the wet etching process, the final process step. Figure 3.18a and b show respectively the front and back side of the membrane. The backside is apparent due to the laser paths of the thinning procedure. Moreover, the pore size (9.8 µm) is identical on the front and backside and seems well opened. Further characterization is, however, required to verify the dimensions of the inner part of the pores. Figure 3.18c exhibits the fluidic slits wall surrounding the filtering structure. The walls appear straight and, although the laser path in between layers can be seen, the scalloping

effect is negligible compared to the size of the openings. A larger micrograph including the central part of the filtering device is shown in Figure 3.18d and confirms the general aspect of the fabricated device: the electrode alignment regarding the pores and the insulator is correct, and the device does not show any weakness points such as cracks. The KOH etching, however, leaves some residuals which need to be cleaned afterwards using deionized water.

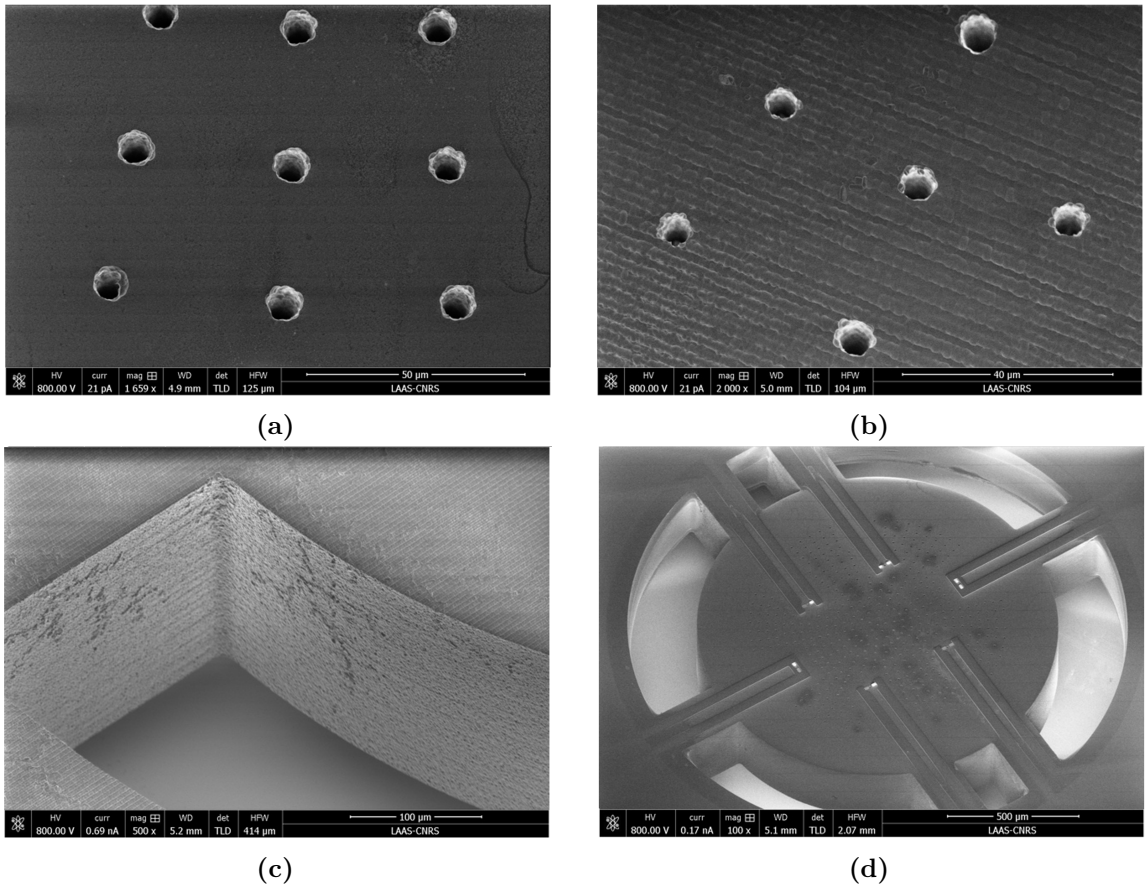

Figure 3.18: SEM Micrographs of membrane pores on the front side (a) and backside of the device b. The backside of the device exhibits lines due to the wafer thinning step. The fluidic slits shown in c are well defined and the overall device shown in d does not show any weakness points such as glass cracks.

3.3 Device Integration: ICHIP

A 3D printed integration chip is fabricated to embed the microdevice in a fluidic channel while featuring an optical access to the microperforated membrane for live epifluorescence imaging. This chip in printed by Stereolithography (SLA) using an original Print-Pause-Print (PPP) process in three steps.

3.3.1 Stereolithography and Print Pause Print (PPP) Process

Stereolithography or SLA is an additive manufacturing process allowing a layer-by-layer fabrication of complex 3D structures (see figure 3.19a). The foundation of stereolithography lies in the exothermic polymerization process known as the curing reaction of resins, involving chemical cross-linking reactions. The UV light exposure initiates this reaction, which is marked by two transitions: gelation and vitrification. Gelation is a liquid-to-rubber transition that leads to a significant increase in viscosity. During this critical phase, both liquid phase and solid phase coexist in the system. Vitrification is a gradual process by which liquid or rubber resin transforms into a glassy solid resin.

A conventional structure fabrication process follows three major steps. First, the computer design of the 3D parts followed by a slicing step of the design in printable layers. The printer then exposes every layer by laser writing within the resist tank. Finally, the fabricated structure is dismounted from the platform, cleaned from unpolymerized resist with solvents and post-treated with global UV curing. The following protocols are done using a DWS J29+ printer (see figure 3.19b) with a planar resolution (x, y axis) of 30µm and a vertical resolution of 10µm in the z-axis. The DS 3000 resist is a biocompatible resist which can be used as a support structure for cell culture. It requires 15 minutes post UV curing treatment (see figure 3.19c).

3.3.2 ICHIP Fabrication

Following a PPP approach, the fabrication protocol for integrating both a see-through glass coverslip and a clean room fabricated silicon-based device in a 3D printed chip is shown on figure 3.20. The printed design is shown in figure 3.20c and figure 3.21 with the integrated parts together with a representation of the flow within the chip, going from the inlet to the outlet and therefore crossing through the integrated µSieve. A spring-loaded pin held by a multiplexer PCB (described in section 3.3.5) is inserted post-printing for electrical contact with the integrated device.

The adaptation of the Print Pause Print technique to our process is done through six steps for integrating two objects: the glass coverslip and the µSieve. First, a donut

(a) **(b)** **(c)**

Figure 3.19: (a) Working principle of 3D printing through stereolithography. (b) DWS SLA Printer and (c) the UV post-curing station Form Cure (Formlabs).

shape is printed, corresponding to the bottom side of the chip with the inner part of the donut being the optical access (see figure 3.20a). The printing is paused and a silanized glass coverslip is deposited on top of the donut, the printing then resumes, and the coverslip gets trapped in the polymerized resist. Fluidic channels are printed on top of the coverslip and, after a second pause, a microperforated membrane is incorporated and gets imbedded by the polymerized resists (see figure 3.20b).

Finally, resist development is done by flushing ethanol through the fluidic channel and is followed by a 15 min UV curing.

The result of this 3D integration shown in figure 3.21 provides an inverted optical access to the imbedded microperforated transparent membrane with fluidic connectors on top, allowing for live imaging of the device during cell capture and top side access to electrical contact pads of the device through inserted spring-loaded pins.

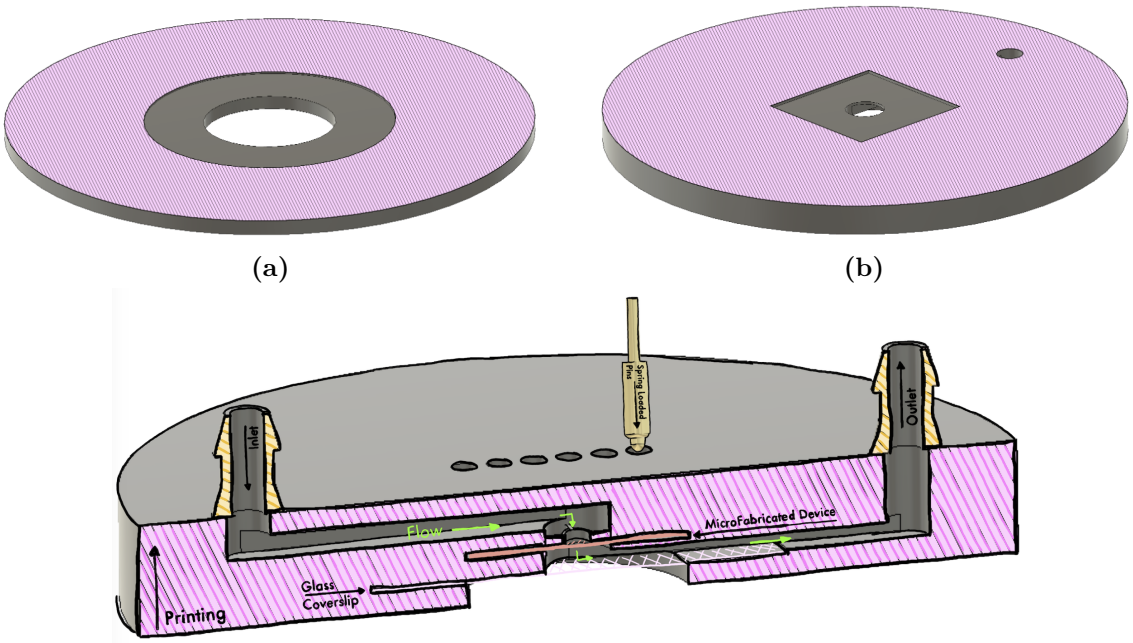

(a) (b) (c)

Figure 3.20: 3D Printed (SLA) Microfluidic Chip Fabrication Process. Integration of the glass coverslip (a) followed by the integration of the microfabricated device (b). The upper fluidic canal and connectors are then printed on top of the two integrated objects (c).

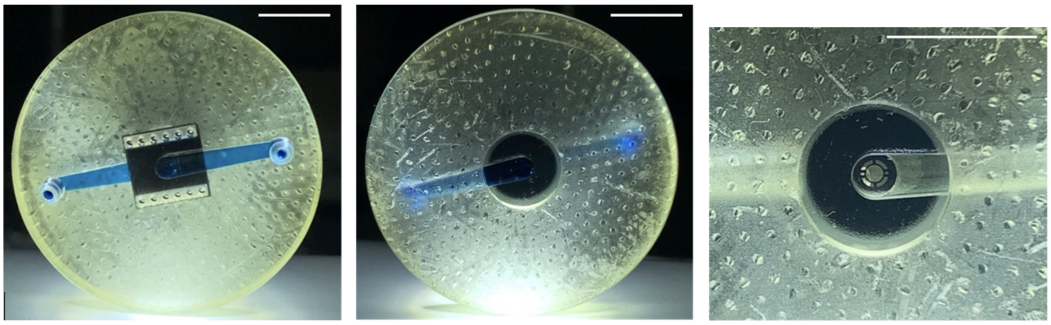

(a) (b) (c)

Figure 3.21: Integration of the cleanroom fabricated silicon device with optical, electrical, and fluidic access in a 3D printed chip. The printed chip has an overall diameter of 40 mm, the fluidic channel has a cross-section ranging from 1,5 to 2.25 mm2 and is filled with a blue dyed solution on photographs (a) and (b). (a) Top side of the chip exhibiting fluidic connectors and the integrated device in its center with access to the electrical contact pads through the 12 holes. (b) Bottom side of the device with optical access, to the fluidic canal and the integrated transparent sieve through a glass coverslip. (c) Close up on the center of the chip, showing the channel, the integrated sieve and the fluidic slits surrounding it.

3.3.3 Silanization Protocol of the Glass Coverslips for 3D Integration

To promote adhesion between polymerized 3D printing resist and glass, the coverslips are silanized with a methacrylate silane. The surface is first activated to expose its hydroxyl groups (-OH) through an O_2 plasma on clean coverslips. The coverslips are then placed in a silane solution, where it reacts with the silane. The detailed process is presented in Appendix.

For a better handling of coverslips in between steps together with a plasma functionalization and salinization on both sides of coverslips, a 3D printed holder (SLA, DWS with DS 3000 resist) shown in figure 3.22 is used.

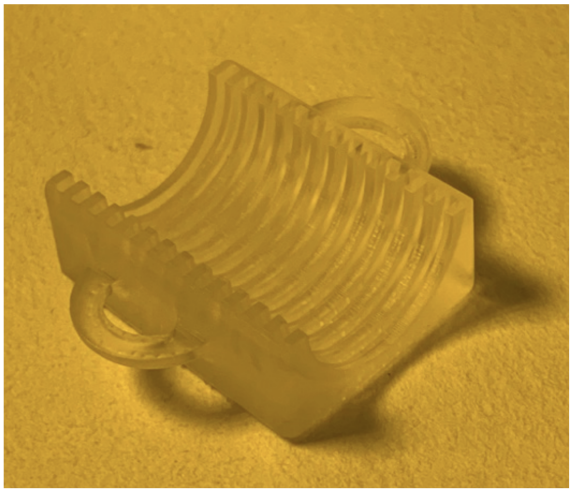

Figure 3.22: 3D Printed (SLA) coverslip holder allowing the handling together with the plasma functionalization and salinization on both sides of the coverslip surface.

3.3.4 Characterization of the 3D Integration

Alignment Resolution

The Print Pause Print technique requires the removal of the printer's head in order to proceed to the insertion of the object of interest before putting it back in. However, SLA printers does not provide any alignment features that would be required for conventional multilayer lithography. The alignment to the already printed structure after an integration step is therefore dependent on the ability of the manipulator to put the printer's head back in the exact same spot. A qualitative way of limiting this error is, when putting the printer's head in, to jam it at the end of the sliding mechanism and also to tilt it, thus putting it in a corner which leads to a reproducible placement.

This method has been characterized (see figure 3.23) by printing two crosses on top of each other with a pause in between the two patterns (control) and another set with a repositioning of the head during the pause (PPP). The control experiment shows the intrinsic variability of the printer which is within the range given by the manufacturer (30-40 µm in the x-y plane).

The Print Pause Print process adds variability to the one of the printers: in the x-plane, the mean shift was of 12.9 µm (± 24.8 µm) for the PPP process compared to 6.6 µm (± 16µm) for the control, and 20.6 µm (± 32.4 µm) compared to 3.5 µm (± 26 µm) in the y-plane. No difference in the angle was detected, both on control and PPP process. This shift is, however, not significant compared to the dimensions of our design and the size of elements inside the chip: cells.

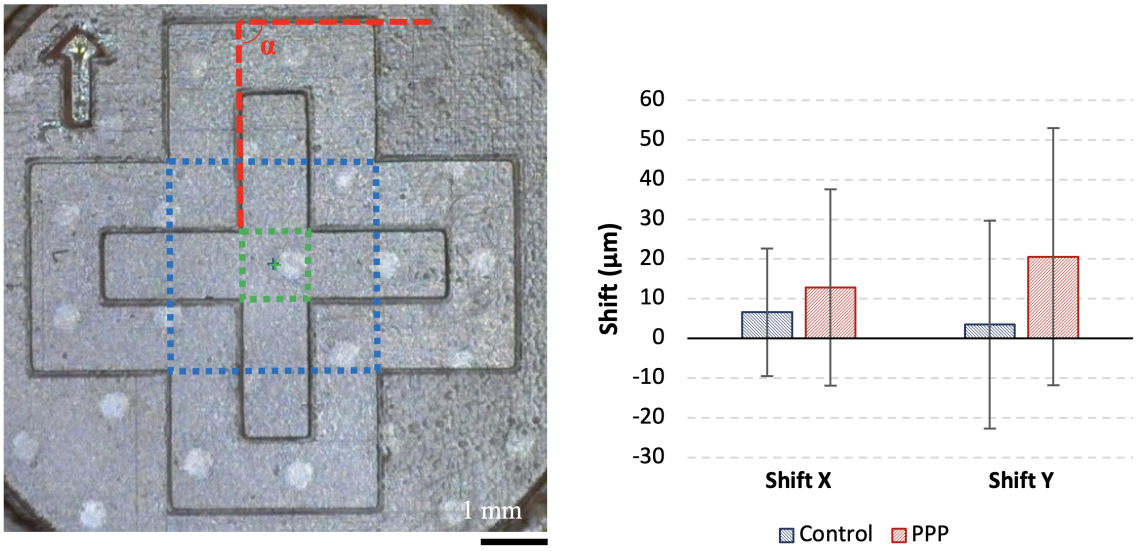

(a) **(b)**

Figure 3.23: (a) Schematic of the measurement: α angle between the bottom and top layer ; position of the center of mass of the top layer (measured with the green quadrilateral inside the inner cross) and position of the center of mass of the bottom layer (measured with the center of mass of the blue quadrilateral inside the outer cross).(b) Characterization of the shift after removal of the printing head during a Print-Pause-Print Process. Error bars represent the standard deviation. From B.Venzac.

Fluidic

Fluidic tests were led to assess the capability of the 3D printed chip to stay watertight at different flow rates. No leaks were found, even at high flow rate of 20 mL/min, the limiting factor thus being the membrane's resistance to induced fluidic pressure which has already been evaluated in chapter 2 and showed to withstand flow rates of this order of magnitude.

However, leaks were induced following the insertion of the spring-loaded pins in

contact with the µSieve, thus short-circuiting the sensing electrodes. A 3D printed spacer using Fused Deposition Modeling (FDM) is therefore added in between the PCB hold, the contact pins and the integration chip (see figure 3.24). With this addition, not leaks could be detected in this range of flow rates.

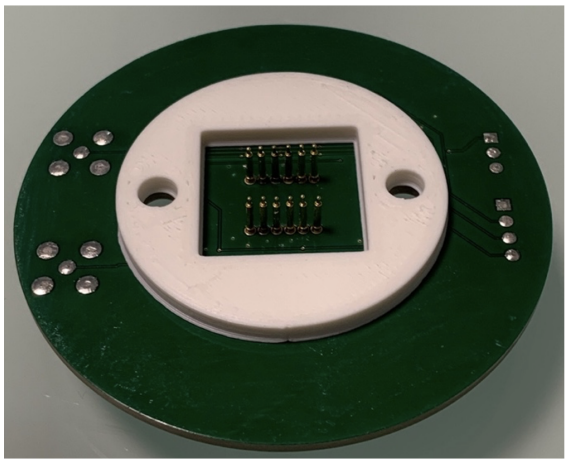

Figure 3.24: Backside of the multiplexer PCB with the added 3D printed spacer (in white) on top to limit the insertion range of the spring-loaded pins.

X-ray Microtomography

Integrated devices were inspected in X-ray microtomography at Institut de Mécanique des Fluides de Toulouse (IMFT). This transmission microscopy technique allows to scan and create a 3D model of a closed system such as our microfluidic chip. Numerical planar cuts can then be made in the reconstructed model to analyze the dimensions of embedded features.

Figure 3.25 shows two side cut views of the 3D printed device at two key locations: the filtration system within the fluidic canal (a) and the electrical contact access holes (b). We can see that the fluidic canal is well defined and the device well integrated within this canal . It can, however, be seen, in the lower left of the µSieve (a) an adhesion issue in between the silicon device and the resist. This is due to the integration order: the device, once deposited within the imprint during the integration hides the unpolymerized resist below it from the laser, leaving unpolymerized resist. This resist gets washed away during the solvent cleaning of the fluidic channel, thus leaving a gap in between the device and the resist. It, however, does not seem to bring any leakage in the system and could be improved by salinization of the microfabricated devices.

Indeed, looking at the glass coverslip, we can see that it is well integrated and that it does not show the same adhesion issues as the device. This can be explained by the fact that coverslips are transparent and that the resist can be polymerized by the laser through the glass layer whereas the silicon devices are obstructing the laser

and unpolymerized resist may be trapped below the devices during the integration step.

Finally, we can see that the pin insertion holes are well aligned with the contact pads. However, due to the reflective nature of gold, the polymerization surrounding the contact pads was not well controlled and design optimization was needed in order to obtain the right dimensions for these holes as a tight fit is required in order to guide the contact pins precisely on the contact pads. Overall, and after many fabricated and integrated devices, the integration process is robust: it does not show leakage and is perfectly reproducible. It takes 2 hours in total to print and 30 minutes to develop and do the UV post-printing curing process.

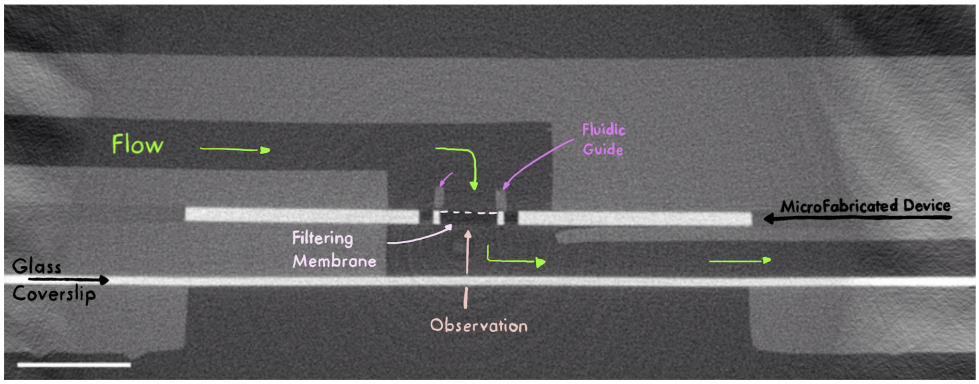

(a)

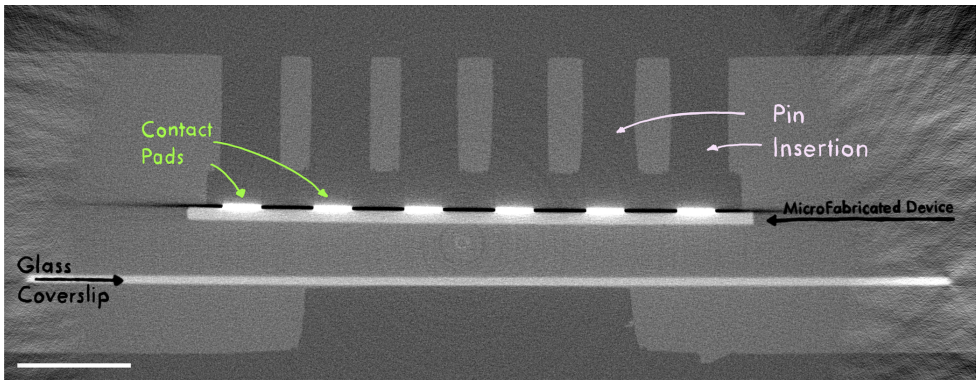

(b)

Figure 3.25: X-ray tomographs of a 3D printed integration chip encapsulating a glass coverslip and a microfabricated device. (a) shows a side cut at the center of the device, thus exhibiting the filtering membrane within the fluidic channel and the glass coverslip whereas (b) shows a side cut at the electrical pin insertion locations with the gold microfabricated pads in bright white. Scale bar: 2 mm.

3.3.5 Electrical Integration

As discussed previously, the microfabricated device embeds 6 electrode pairs which need to be probed individually by an impedance analyzer. Thus, a multiplexer is needed to automatically cycle through these electrodes while a capture sequence is running. The multiplexer, designed by Fabrice Mathieu, Engineer in Electronics at LAAS CNRS, was fabricated by the company CIMULEC Group. The electrical schematic is presented in figure 3.27 and the fabricated PCB board is shown in figure 3.26. The PCB shape is specifically designed to let the fluidic ports accessible through it while holding the contact pins in contact with the device. The 3D printed chip is held in between the inverted microscope petri dish support and the multiplexer PCB, thus avoiding any movement during the experiment while having an optical, electrical and fluidic access to the printed chip and microfabricated device in its core. The working principle of the multiplexer is based on two 8 bits shift registers in series (74HC595). These two shift registers are connected in turn to 12 SPDT CMOS switches, each connected to a spring-loaded pin. Finally, an Arduino is used to control the two shift registers. When in series, a 16-bit signal is sent at the first shift register which sends the first 8 bits to the second shift register.

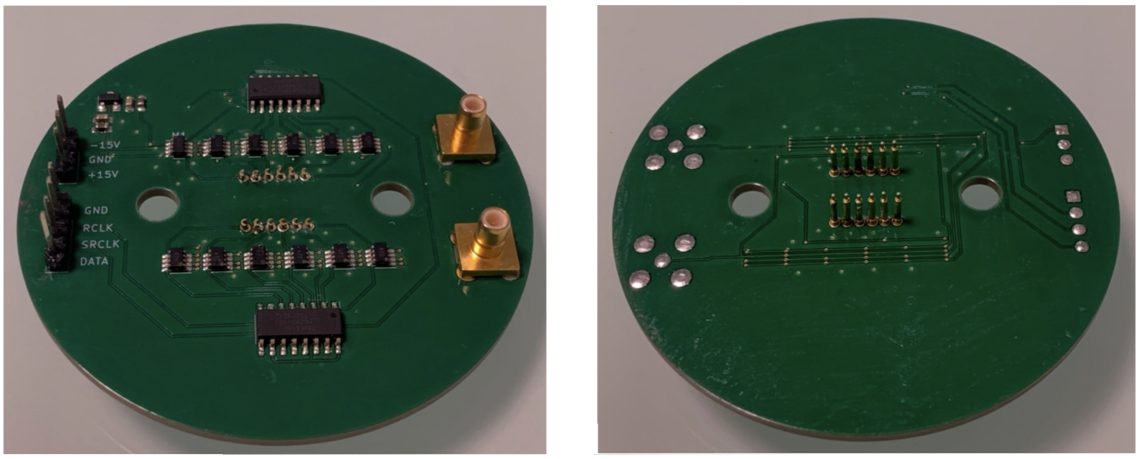

(a) **(b)**

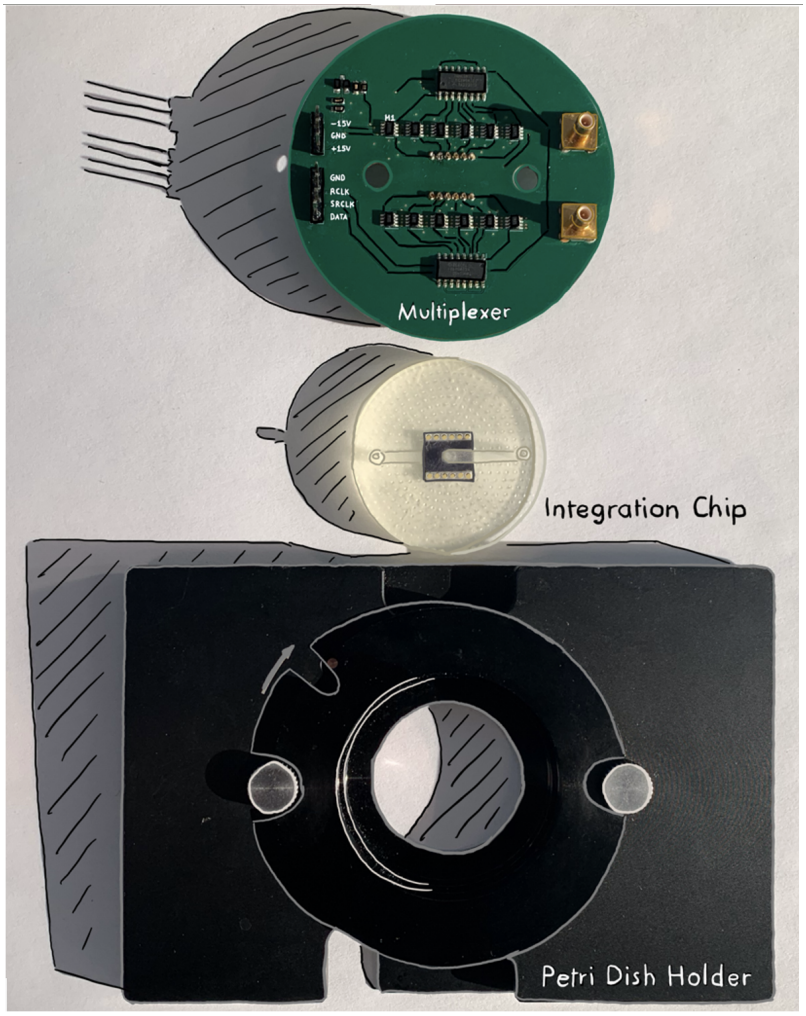

Figure 3.26: Printed Circuit Board (PCB) of a multiplexer. The top side (a) exhibits the electrical components together with two holes for the fluidic connections to go through, two coaxial connections on the right side, and the data and power pins on the left side. In the center, the 12 spring-loaded pins are going through the PCB and can be seen on the top side (a) and on the bottom side (b). c. Shows the positioning of each element: the multiplexer, the integration chip and the microscope petri dish holder (Olympus IX3-HO35D).

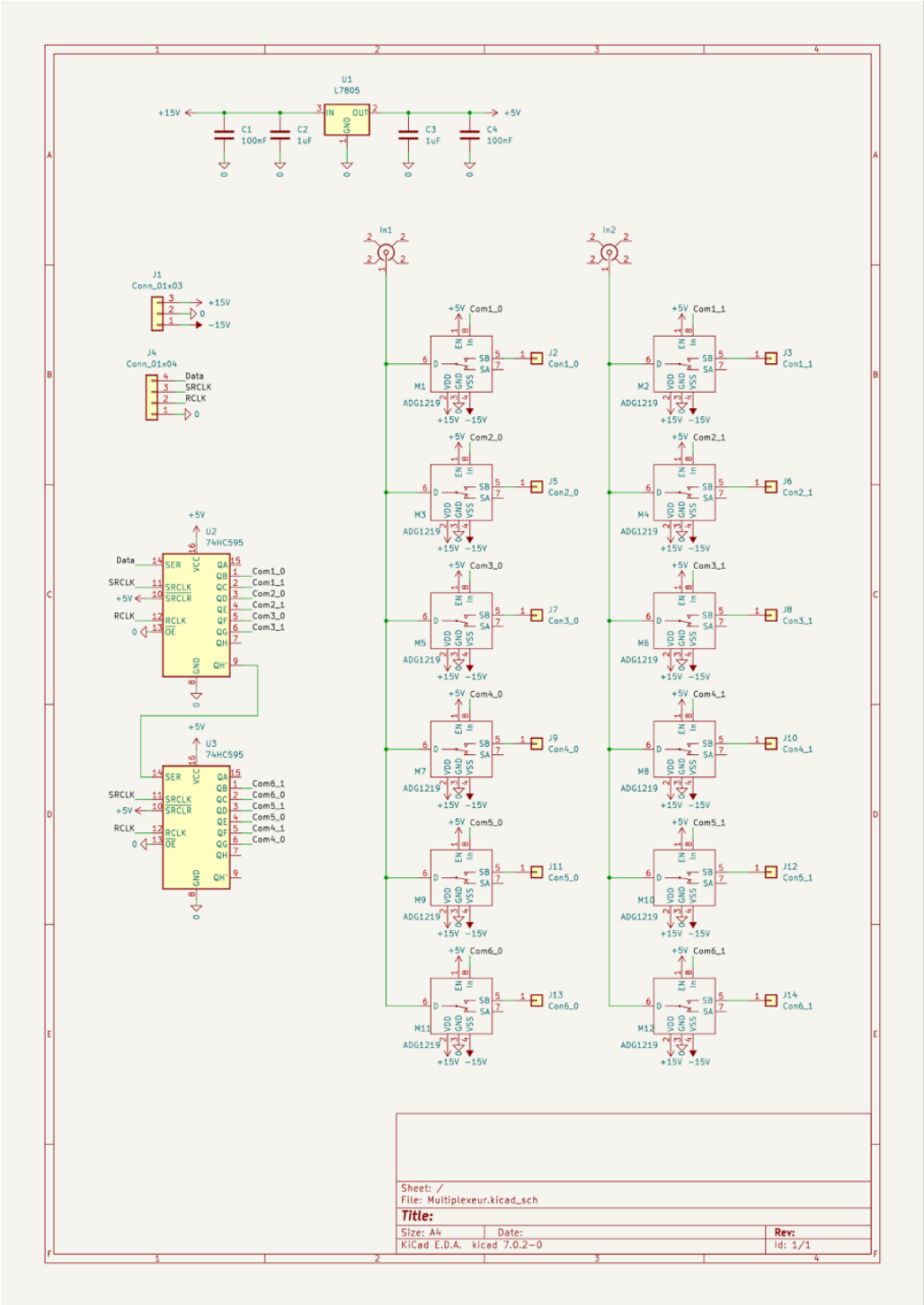

Figure 3.27: Electrical Schematic of the multiplexer. From F. Mathieu.

Finally, the Arduino is controlled through a serial connection and a Python code. Python, although not being the native language of Arduino, can be used to command them. In our case, Python was also needed for the automation of the microscope and the impedance analyzer which needed to be synchronized to the multiplexer. Hence, we chose to write the automation algorithm by using a single coding language. The electrical characterization of the multiplexer is done using an impedance analyzer. For each pin, impedance spectra were measured from 1 kHz to 10 MHz, in open circuit and short circuit. Results are shown in figure 3.28 . Open circuits exhibit a small capacitive of high impedance signal, thus leading to a noisy signal in the low frequency band. Short circuits exhibit a resistive effect within the measurement range, ranging from 247 Ω to 252 Ω depending on the pin pair.

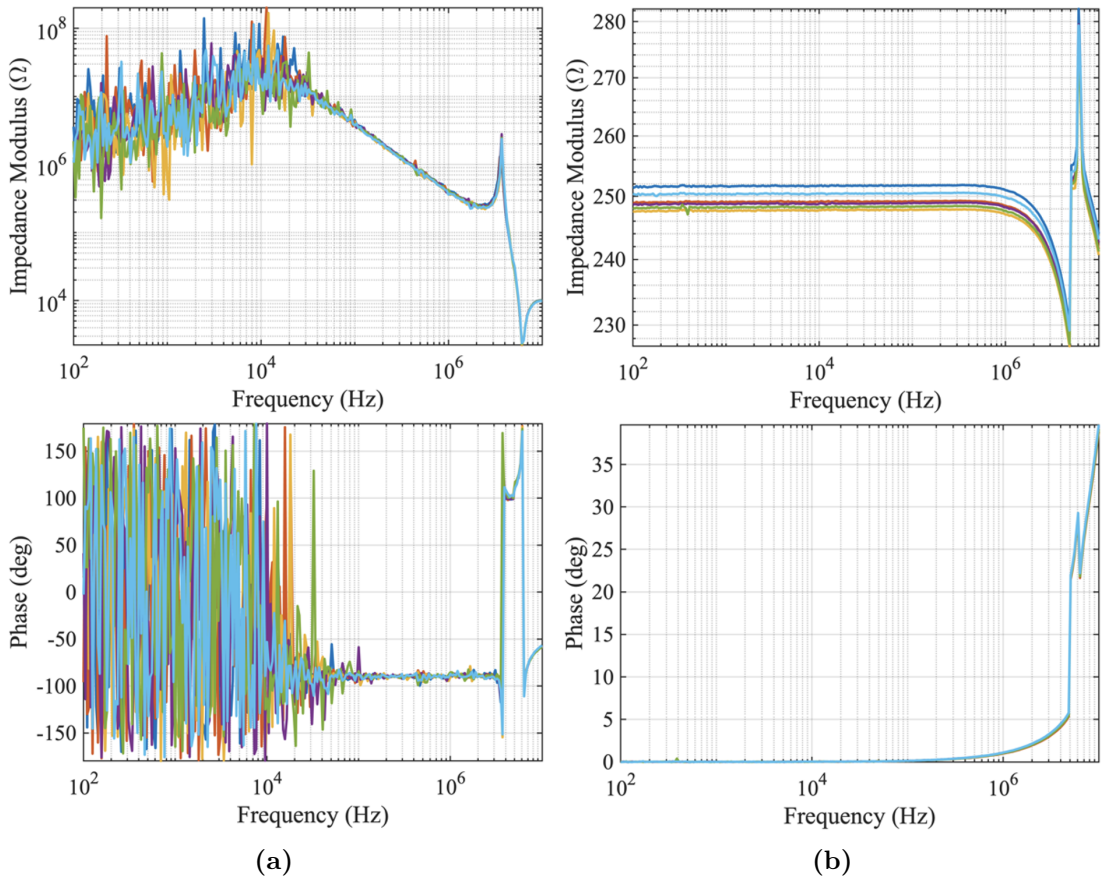

Figure 3.28: Multiplexer characterization through impedance spectroscopy with one color for each pin pair. Measured impedance spectrum of the open circuit configuration (a) and short circuit configuration (b).

We can, however, see on these calibration impedance spectra that, both in open and short circuit, the multiplexer brings an inductive effect around 1 MHz. The origin of this effect still needs to be investigated.

Furthermore, figure 3.29 shows LCR impedance measurements for 30 seconds of an integrated microfabricated device within PBS using the multiplexer to index the 6 electrode pairs. The impedance characterization of fabricated devices will be

discussed in the upcoming sections. It is, however, interesting to note that, as shown in Figure 86b, the multiplexer offers a time resolution of 20 ms for a single electrode. Since the multiplexer cycles through electrodes E1 to E6, it therefore takes around 3 ms for each measurement which includes the switching of the multiplexer and the measurement time of the impedance analyzer.

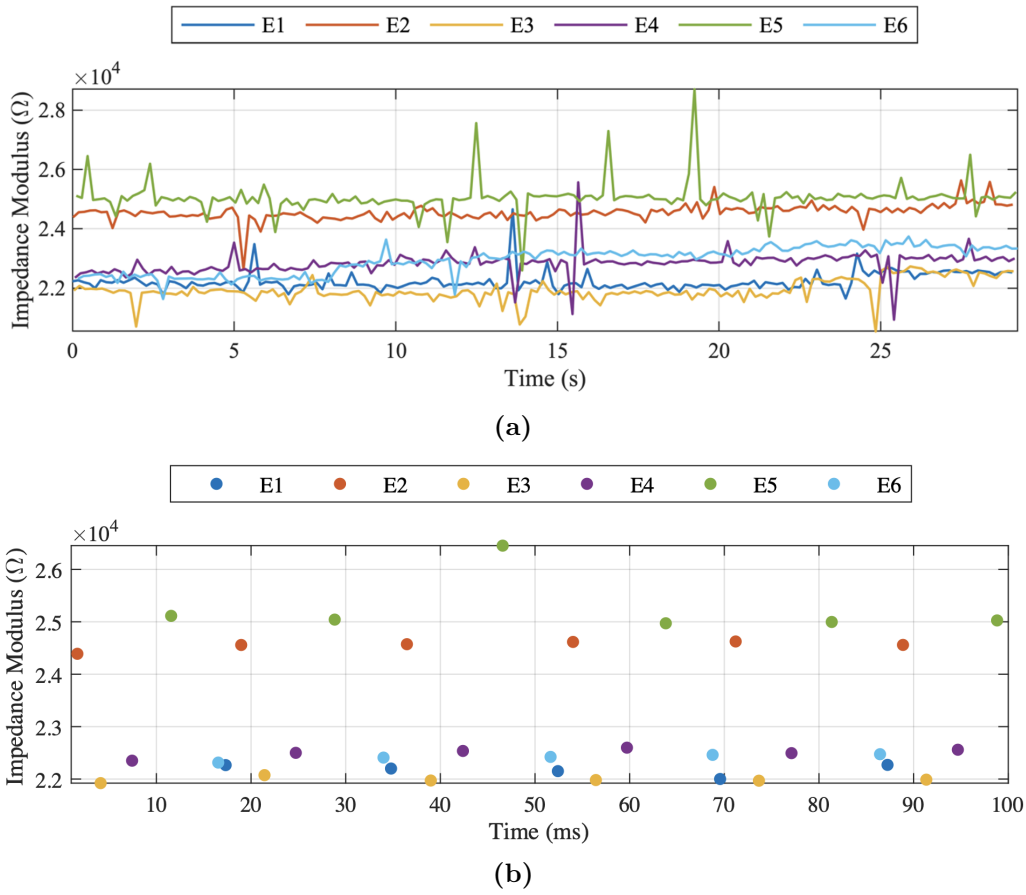

Figure 3.29: LCR Impedance measurements using the multiplexer to index 6 electrode pairs. (a) shows 30s of recording while (b) is a focus on 1 second of measurement.

3.4 Experimental Platform and Automation

3.4.1 Platform Description

The experimental platform was elaborated along the design and fabrication of the previously presented integration chip and multiplexer. The platform is mounted on a vibration isolation table in a dark room to avoid light interference with the microscope.

The optical system is composed of an Olympus Inverted microscope (IX73), a camera (Hamamatsu Orca Flash 4) and an epifluorescent light source (Lumencor Sola 6) covering the excitation for DAPI, GFP, CY3 and CY5 fluorophores. The fluidic system is composed of a CETONI Base 120 syringe pump together with Fluigent 1.6 mm tubing.

The electrical system includes the multiplexer, its power supply and the impedance analyzer (HIOKI IM3570), already presented in chapter 2. Figure 3.30 shows the experimental platform.

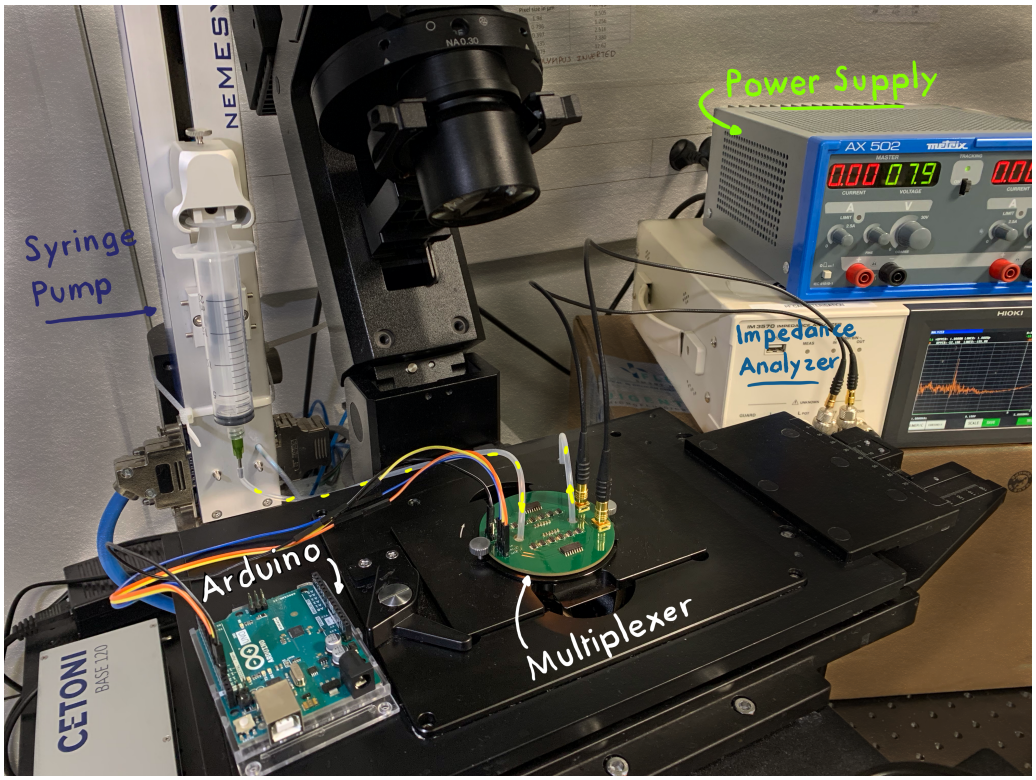

Figure 3.30: Experimental platform including an inverted microscopy system (with a camera and a fluorescent light source), the electrical measurement setup (Arduino controlling the multiplexer powered with an independent power supply) and a fluidic syringe pump.

3.4.2 Experimental Protocol

The experimental protocol can be divided into three main steps: pre-processing, processing, and post-processing.

Regarding electrical measurements and as discussed previously, impedance spectra are time consuming measurements while LCR measurements (i.e. at a given frequency) are much faster. Therefore, these three steps correspond each to a different measurement mode: impedance spectra are measured as reference during the pre-processing step and compared to impedance spectra measured post-process. However, during the sample processing, a high time resolution is needed, we thus employ LCR measurement mode at a selected frequency.

The fluidic system also follows these three main steps. During the pre-processing step, 10 mL of ethanol is flushed through the tubing and integration chip in order to obtain a good wettability and avoid bubble formation. Then, 20 mL of PBS 1X is flushed to replace ethanol and set physiological conditions. The sample processing step starts by flowing the sample within the system using the syringe pump at a flow rate of 1 mL/min until the membrane is fully covered with cells or the sample empty. Finally, post-processing, the trapped cells can be kept on the membrane for further in-situ culture, the device is then filled with culture media. The membrane can also be cleaned and reused by back-flushing PBS and ethanol.

Finally, the microscopy system, which includes the microscope, camera and light engine is synchronized with impedance measurements. It first takes reference images during the pre-processing and post-processing steps. Then, during the processing step, an image is taken simultaneously with each electrical measurement of each electrode pair. Images are added on the fly to an image stack which is shown on the screen for a live experiment follow-up. It is then split in multiple files in order to limit the weight of each file to 2 Go and saved for further analysis. The light engine is switched on and off for every photo to limit photobleaching of the fluorophores that could be induced.

3.4.3 Python Automation

Controlling and synchronizing every element of the microscopy system together with the electrical measurement setup required a software automation. This automation was done using the programming language Python.

As discussed previously, an Arduino Uno R3 is used to pilot the multiplexer by sending the 16-bit data and the actuation clocks allowing selecting which contact pin is linked to the two coaxial outputs connected to the impedance analyzer. Thus, to change routed electrode pair, the Python program sends the pair number, ranging from 1 to 6, to the Arduino through the serial port connected to the computer.

Commanding the other systems (impedance analyzer, light engine and camera) is done through individual serial ports, using dedicated Python libraries developed by the respective manufacturer.

The experimental protocol is hard-coded in the main program and follows the following steps: **Pre-Processing**:

- Initialization of all devices.
- Focus adjustment of the microscope, exposure time adjustment of the camera.
- Configuration of the impedance analyzer for impedance spectroscopy.
- Reference impedance spectroscopy measurements for each electrode pair.
- Reference imaging of the device.

Processing:

- Configuration of the impedance analyzer for LCR measurements.
- LCR measurement and imaging for each electrode pair.

Post-Processing:

- Configuration of the impedance analyzer for impedance spectroscopy.
- Reference impedance spectroscopy measurements for each electrode pair.
- Reference imaging of the device.

3.5 Experimental Characterization of Microfabricated Silicon Devices

Two fabrication processes were previously presented. However, the glass-made devices required further process optimization, thus restricting the 3D integration and subsequent electrical and biological characterization to the silicon devices.

3.5.1 Real-Time Cell Capture Observation

Although the membrane is of similar fabrication than the one already presented and characterized in chapter 2, its placement regarding the supporting structure is not the same, nor is the holder which integrates the device in the fluidic system. Thus, the first experiments were led using only the microscopy and fluidic system on microfabricated devices without integrated electrodes. The very first video shown in figure 3.31 as 6 timestamps correspond to the real-time imaging of PC3-GFP cell filtration on the membrane. This first experiment demonstrates that real-time observation of a cell capture on a microfabricated membrane and within a microfluidic canal is possible.

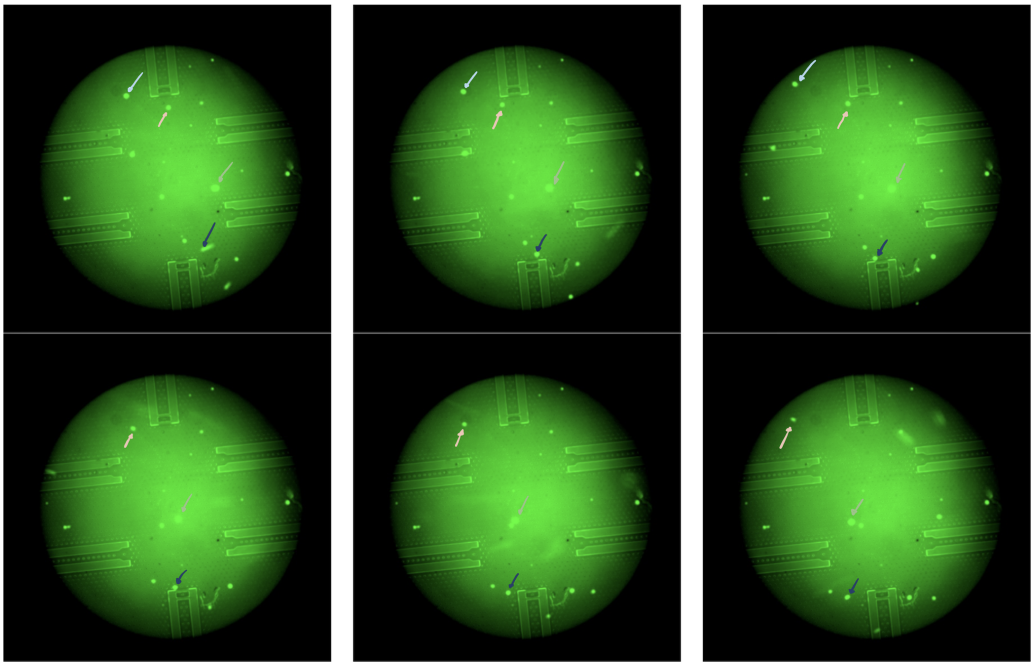

Figure 3.31: Real-time optical inspection of the filtering membrane along cell capture. To read from left to right, top to bottom. PC3-GFP cells in PBS rolling from right to left side of the membrane. Colorized arrows show the displacement of individual cells on the membrane.

Furthermore, it brings valuable insight into the capture kinetics happening in the surroundings of the filtering membrane. Indeed, in this experiment, figure 3.31

shows cells coming on the membrane from the right side, rolling on the membrane and leaving the membrane on the left side.

As discussed in the section 3.2.1 about Silicon Devices fabrication process, the supporting structure is now under the device, thus having, at the same level, the filtering membrane and the fluidic slits. However, fluidic slits handle most of the flow rate, therefore inducing tangential flow over the membrane surface and dragging the cells in the side slits. This side effect was not observed in the microfabricated devices presented in chapter 2 because the supporting structure was grown above the membrane, thus building a well in between the membrane and the fluidic slits. In order to limit this effect for further experiments, an inner fluidic guide of 400 µm height shown in figure 3.32 is printed on top of the filtering membrane during the 3D integration.

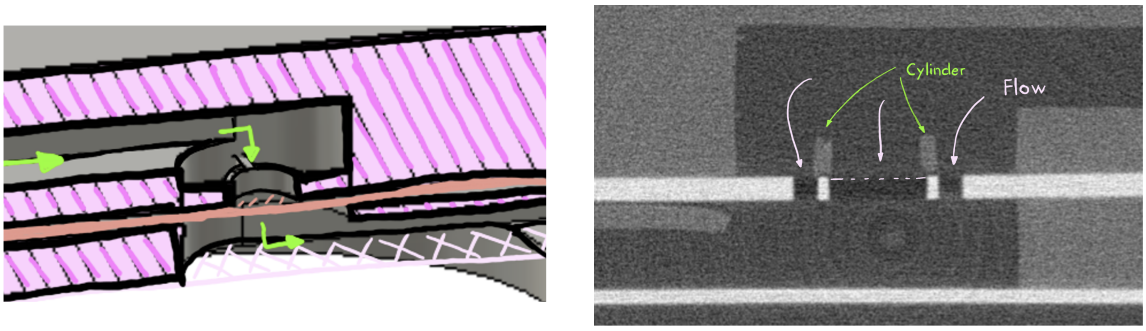

(a) **(b)**

Figure 3.32: Inner fluidic guide printed on top of the microfabricated device. Four arms hold it in the center of the fluidic canal. (a) Shows the 3D CAD model and (b) a tomography image of the microfabricated device with a side view of the cylinder printed on top.

After this design modification, the following capture experiment shown in figure 3.33 did not exhibit any rolling of the cells outside of the membrane, thus leading to a better cell trapping on membrane pores: 420 cells trapped with the initial concentration of 1000 cells/mL in the 5 mL sample.

The previous experiment was repeated with microfabricated devices with integrated electrodes. The addition of electrodes did not seem to alter the capture ability of the filtering membrane as it can be seen in figure 3.34b where the membrane is covered with cells. However, only six pores over 2129 are indexed by electrodes but, as shown in figure 3.34, 4 pores out of 6 indexed pores are occupied by cells.

In order to quantify the number of cells captured in pores indexed with electrodes together with having of precise timestamp of each capture event, automated video post-processing is needed. Indeed, an experiment generates around 2000 frames which, each, needs to be analyzed at the 6 indexed pores. Therefore, an ImageJ Macro was developed and allows obtaining a precise estimation of the timestamp at which indexed pores are filled with cells through monitoring gray intensity evolution. The output of this macro shown in figure 3.34a exhibits sudden steps, correlated with

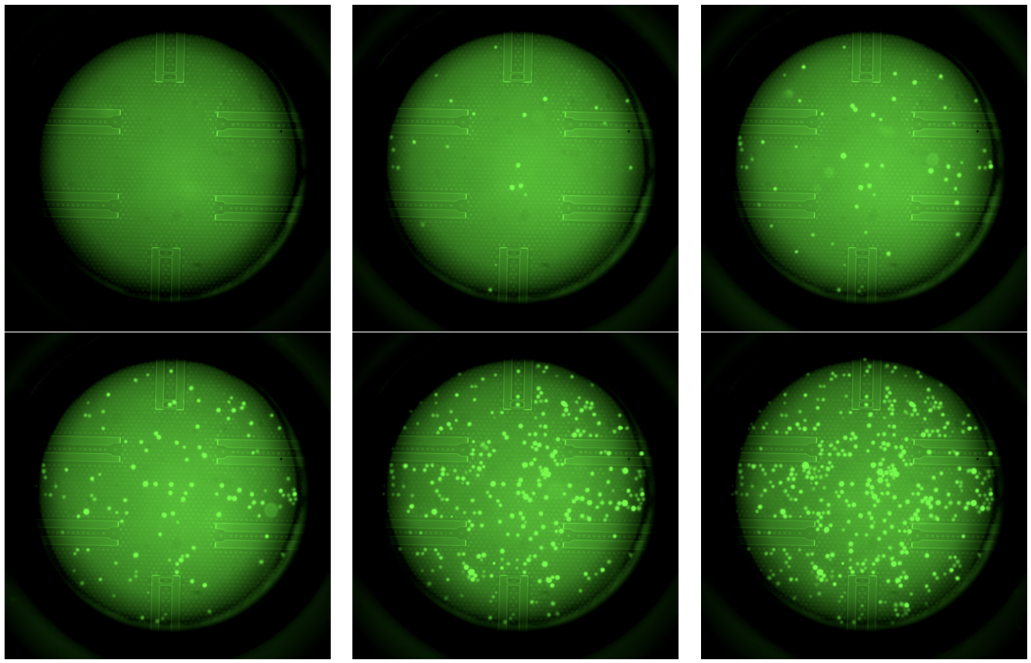

Figure 3.33: Real-time optical inspection of the filtering membrane along cell capture with PC3-GFP cells in PBS. Microfluidic chip with added fluidic guide. Full video available upon request.

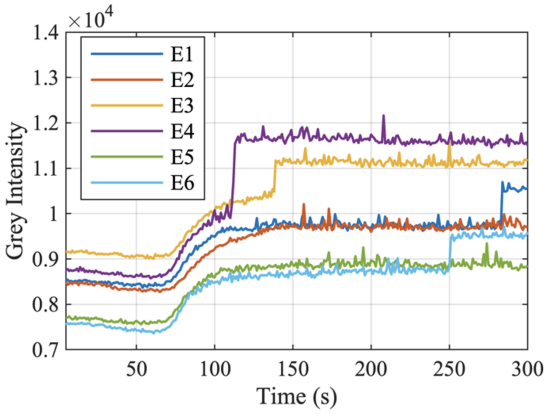

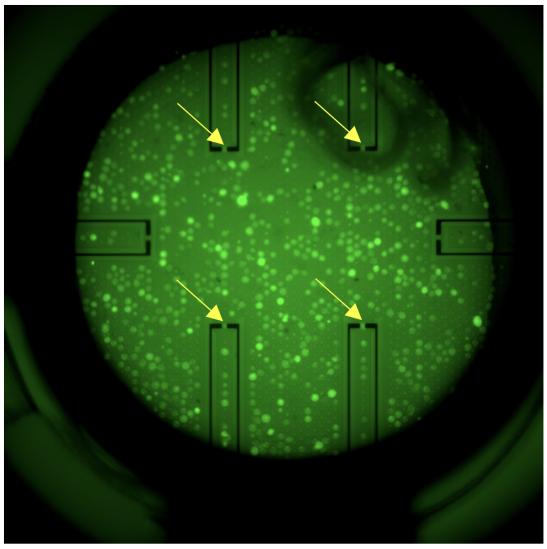

(a) **(b)**

Figure 3.34: (a) Video-Processing of images taken along cell capture showing the evolution of gray intensity between each electrode pair. (b) shows the filtering membrane at the end of a capture experiment with 4 cells in pores indexed by the electrodes (yellow arrows).

a capture event in between an electrode pair. In this experiment, 4 indexed pores are filled in between 100s and 300s of sample processing time which is confirmed by looking at the post sample processing image on the right. This data processing allows establishing precise optical quantification of the capture events, which can then be used as a control in comparison to other quantification methods such as impedance measurements.

3.5.2 In-Situ Cell Culture

Clinical applications usually require further analysis of the collected sample, especially in the liquid biopsy field, thus inducing sample handling and potential tampering. We therefore test whether the device could allow cells to be cultivated on the collection site, within the integration chip, on the microfabricated device directly after the sample filtration.

A fibronectin coating is first done on the integrated filtering membrane. Fibronectin is a protein present in the extracellular matrix and plays a key part in the cell adhesion to the extracellular matrix through integrin/fibronectin binding. This coating is necessary for the adhesion and proliferation of cells on the filtering membrane. The functionalization consists of the injection in the microfluidic chip of a solution at 10 µg/mL of fibronectin in sterile PBS. It is then incubated for 4 hours at 37°C and washed away with PBS.

Figure 3.35 shows bright field images of live cell culture of trapped PC3 cells in the filtering membrane. Following the cell capture protocol described in previous sections, the microfluidic chip was then filled with standard PC3 culture media (RPMI with 10% Fetal Bovine Serum, 1% Penicillin, 1% Geneticin at 37°C) and put in an incubator. The culture conditions and processes were kept identical to the ones used to culture PC3 cells in standard flasks. On D0 (a), cells have just been captured on the membrane, they are not adherent to the surface yet as they keep a rounded shape. However, starting from D1 (b), the fibroblast-like shape of adherent PC3 confirms their adhesion on the filtering membrane. This first experiment did not include staining, such as Propidium Iodide, that would have allowed for the quantification of the evolution of the cell culture. We, however, show in between D2 (c) and D2 (d) the change in culture media within the microfluidic chip. It confirms that cells are well adherent to the surface and that solutions can be flown along cell culture in the filtration membrane without inducing any cell detachment. Further experiments would therefore need to address the in-situ staining capability together with quantification of cell culture evolution.

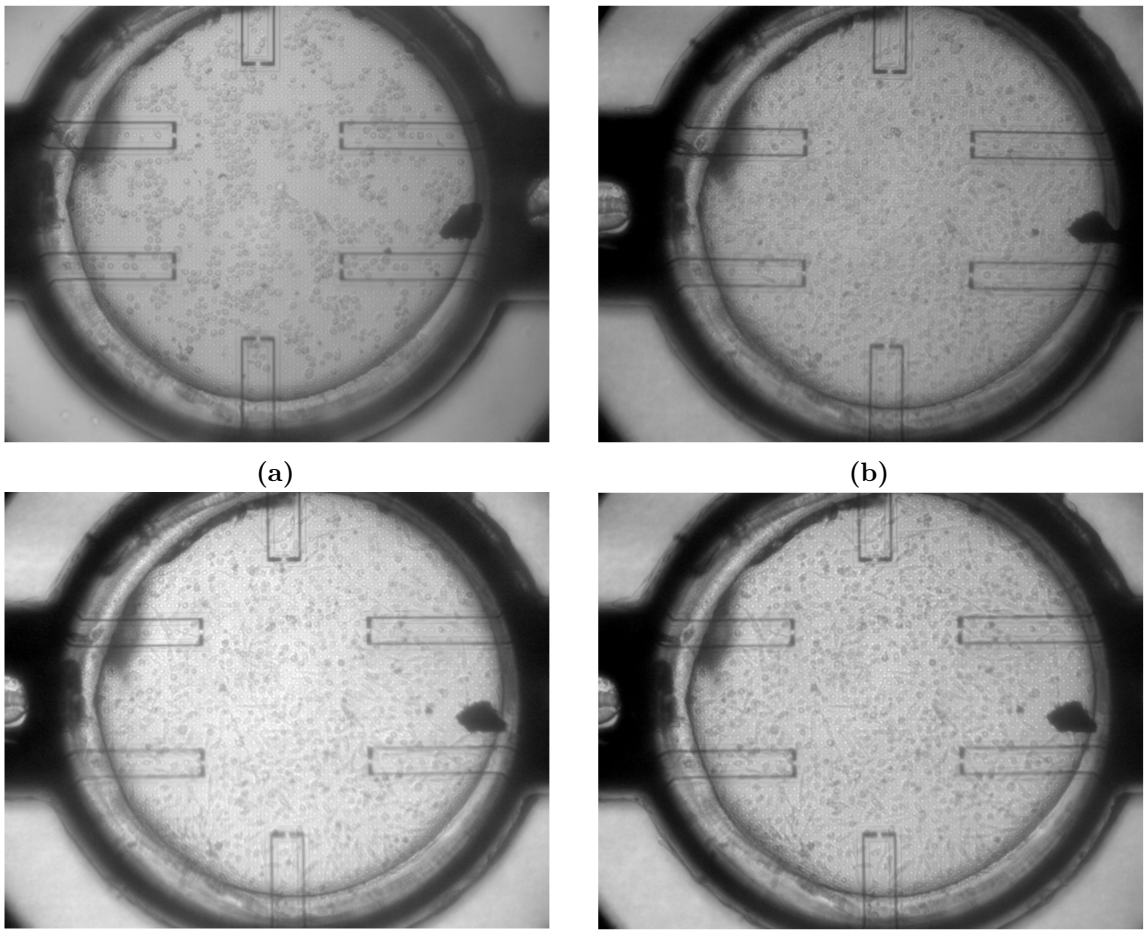

(a) **(b)**

(c) **(d)**

Figure 3.35: Microscopy bright field images during the culture of trapped PC3-GFP cells on the filtering membrane, within the 3D integration chip over three days: D0 (a), D1 (b) and D2 (c) and (d). A culture medium change is done on the third day in between (c) and (d)

3.5.3 Electrical Characterization of Fabricated Devices

We previously characterized the fluidic, optical and biological aspects of our microfabricated devices, integrated system and experimental platform. Finally, the electrical characterization will be discussed in the following sections. Electrical characterization starts with the evaluation of the impedance spectroscopy signature of the device in the reference medium (PBS) and compare it to the predicted signals using equivalent electrical circuit models. This step allows to characterize every electrical phenomenon, therefore setting a baseline for experiments in more complex media.

Calibration Measurements

Electrical measurements are done using the experimental platform described above. Indeed, it allows for a live optical control of the environment surrounding the electrodes while under test, thus being sure that there are no bubbles or dust on the membrane which could affect impedance measurements.

First, calibration measurements are done without any fluid inside the 3D printed chip. Impedance measurements are led using the widest frequency band available with the HIOKI Impedance Analyzer (1 kHz to 5 MHz) and shown in figure 3.36 for 3 electrode pairs. We can see that the device exhibits a capacitive behavior within the frequency range for the three electrode pairs. The impedance modulus and phase are reported in the table of figure 3.36. It is interesting to investigate the relative impedance differences in between the impedance pairs by drawing an electrical equivalent circuit presented in figure 3.36. It is composed of a capacitance, accounting for the capacitive effect visible within the measurement range. However, to fully quantify the electrical behavior of our device, two resistances are added, which each combine the access track resistance with the multiplexer's resistance. These two effects were quantified respectively in table 3.2 and section 3.3.5. Herein, for the first pair of electrodes E1, the two access tracks are L1 and L2. Therefore, R LINE is the series combination of the resistance of L1 (232 Ω) and L2 (191 Ω) and R MUX the resistance of the multiplexer (250 Ω). The second electrode pair E2 is linked through two tracks of identical length (L3), and, due to symmetry, E3 is using access tracks identical to L1 and L2. The capacitance is obtained through the following equation:

$$C = \frac{1}{2\pi f X_c} \tag{3.2}$$

where X_c denote a purely capacitive reactance.

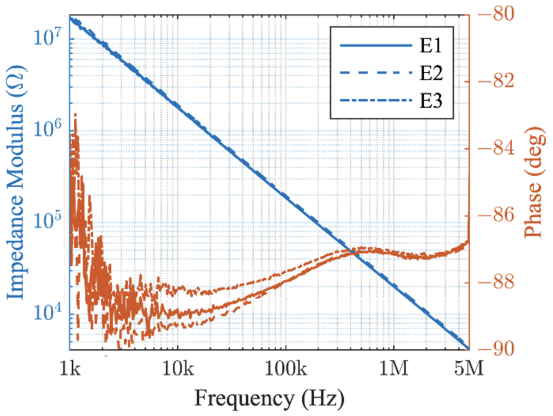

(a)

	Impedance Modulus	Phase
E1	19724 Ω	-87 deg
E2	20760 Ω	
E3	19751 Ω	

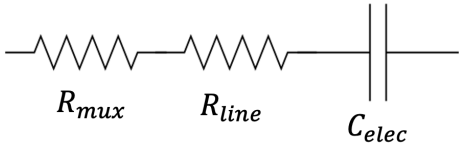

(b)

Figure 3.36: (a) Impedance spectrum of 3 electrode pairs of the same device in air (no fluid in the chip), showing the modulus in blue and the phase in red. The table (b) reports impedance modulus and phase for each electrode pair at 1 MHz. The equivalent electrical circuit model (c) composed of two resistors and a capacitor is used to describe the experimental data.

Table 3.3 reports the values of the different components for each electrode pair obtained through a fitting process with experimental data. This process allows to precisely quantify the differences in-between electrodes to better understand where variability might come from and its relation to the fabrication design. Indeed, combining the different elements of the equivalent circuit, we can calculate the impedance of our model using the following equation:

$$Z_{eq} = \frac{1}{j\omega C_{elec}} + R_{line} + R_{mux} \tag{3.3}$$

Calculating the impedance of our model using values of table 3.3 shows an offset of $604 \pm 73\ \Omega$ for the three electrode pairs when compared to experimental impedance data. This offset, which is not explained yet, is labeled R_p for parasitic resistance and will be tracked in future experiments. It is, however, interesting to observe that the two symmetrical designs, E1 and E3 show very little deviation in experimental capacitance. Moreover, the difference in capacitance of the device E2 could be explained through the electrodes design. Indeed, as shown in figure 3.8, even though, by design, the exposed gold electrodes are of the same dimensions, the insulator, on the other hand, exhibits a different shape, surrounding the capture pore. It might interfere with fringe electric fields and therefore modify the capacitance of the system. E1 and E3 follow the design shown in Figure 3.8a whereas E2 corresponds to the design in figure 3.8b.

	R LINE	R MUX	C	Z_{eq}	R_p
E1	423 Ω	250 Ω	7.9336 pF	20372 Ω	648 Ω
E2	296 Ω		7.5378 pF	21280 Ω	520 Ω
E3	423 Ω		7.9235 pF	20397 Ω	646 Ω

Table 3.3: Reported values of the equivalent electrical circuit for each measured electrode pair through a fitting process. Z_{eq} given at 1MHz.

Reference Measurements in PBS

Following the calibration measurements, PBS is injected in the fluidic system to take reference impedance measurements in an electrolytic media. Adding an electrolytic media in the equation will challenge the previously presented equivalent electrical model by inducing new physical effects such as ionic interfacial effects.

Figure 3.37a is comparing calibration impedance measurements on electrode pair E1 with impedance measurement within an electrolytic medium: PBS. The latter does not only show a capacitive behavior as the calibration does, therefore, the modeling of the inter-electrode effects cannot be reduced to a single capacitance anymore. The proposed equivalent electrical circuit of our device in an electrolytic solution is presented in figure 3.37b. Since the insulating air present during calibration is replaced by a conductive electrolyte, the dominating effect in between the electrodes will be resistive and not capacitive and, as discussed in previous chapters, even-though capacitance can arise in electrolytic media, it is not dependent on the electrode shape but only on media properties. Thus, the cut-off frequency at which the system transfers from a resistive to a capacitive regime in PBS solution is found to be of 360 MHz. Therefore, any other capacitance appearing in the measurement band can either be induced by interfacial effects in between the electrode and the electrolyte or parasitic effects.

Based on these investigations, we model the inter-electrode medium through the resistance R_M, the capacitive ionic double layer C_{dl} and the parasitic capacitance C_p. These effects are replacing the inter-electrode capacitance observed during calibration and are added to the resistance effects induced by the multiplexer and the access tracks which are combined under a single resistance R_A and the parasitic resistive effects R_P.

Using the values for R_A and R_P reported in table 3.3, C_{dl}, C_p and R_M were adjusted in order to fit the impedance measurements in PBS. Figure 3.37a shows the impedance spectra data of the first electrode pair E1 together with the fitted impedance spectra. We can see that our equivalent electrical model allows for a good fit of the band in between 100 kHz and 5 MHz. However, the rising of the phase from -90° can be seen below 100 kHz, thus indicating that a resistive regime might be hidden below 1 kHz. Indeed, interfacial effects described in the Randles cell in chapter 1 also comprises resistances, such as the charge transfer resistance, which could explain such behavior at lower frequencies. We choose not to add such

resistance in the electrical model, as the double-layer capacitance is already the limiting factor of the sensor's lower frequency.

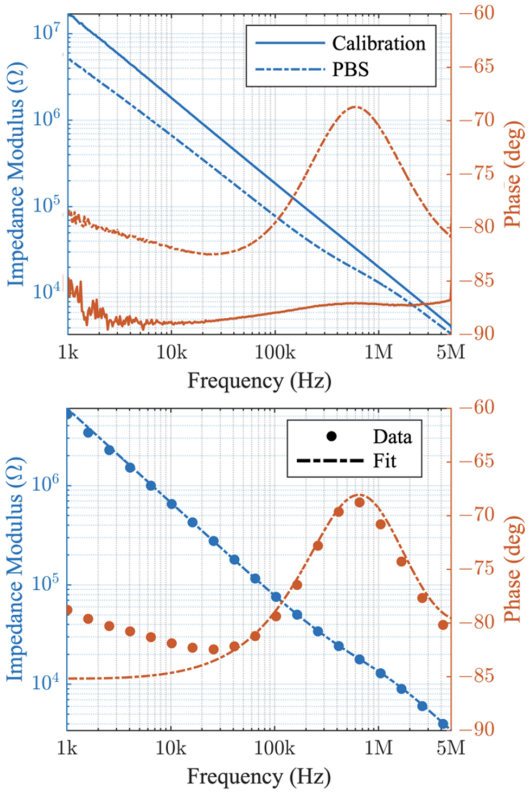

(a)

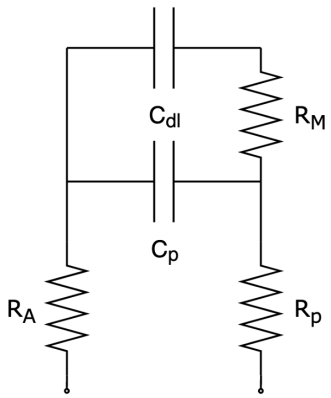

	C_{dl} [$S.s^n$]	C_p	R_M
E1	35.10^{-12}	9.2 pF	29 kΩ
E2	35.10^{-12}	7.5 pF	30 kΩ
E3	35.10^{-12}	9.2 pF	30 kΩ

(b)

Figure 3.37: (a) Impedance spectra with the modulus in blue and the phase in red of the first electrode pair (E1) in air versus in PBS. (b) shows the equivalent electrical circuit composed of three resistors and two capacitances to describe the experimental data, (a) the fitting results of the electrical model compared to the experimental impedance spectra and table (b) reports the fitting values for each electrode impedance with n=0.92 for the constant phase element.

Finally, fitting values obtained for C_{dl}, C_p and R_M are reported in figure 3.37b. We can notice that the results show a reliable measurement of the interelectrode resistance through R_M which is confirmed on figure 3.38 when looking at the superposed impedance spectra of the three electrodes in PBS.

Our previous calibration experiments showed a slight capacitive difference for the electrode E2 which was attributed to the insulator design. This result is confirmed by experiments in PBS. However, since neither C_{dl} nor R_M, which are characterizing the sensing electrodes, changes, the parasitic capacitance therefore seems to be correlated with the access track length, which E2 as the lowest.

Indeed, during the electrode calibration in air, both the capacitance of the sensor and the parasitic capacitance were combined in a single capacitance. With the addition of the electrolytic media, therefore changing from a capacitive to a resistive sensing regime, the parasitic capacitance appears on its own and can be quantified.

Moreover, the quantification of the double-layer capacitance together with the inter-electrode resistance confirms the simulated values which will be presented in the next section. However, simulations accounting for the inter-electrode parasitic capacitance did not show large capacitive effects. Thus, these effects will be studied in more detail regarding their impact on the analysis capability of the device.

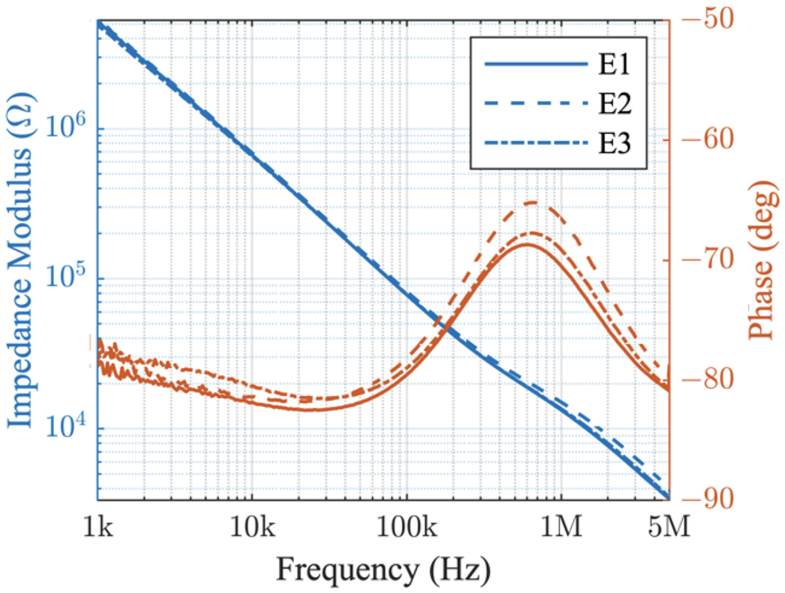

Figure 3.38: Impedance spectra reference measurements in PBS of the three sensing electrodes. Impedance modulus in blue and phase in red.

3.6 Analytical Elements and Simulations

Experimentally quantified elements of the electrical circuit model allow obtaining a good agreement with the simulation results. The electrical model is presented in figure 3.39 and includes two capacitances that account for the ionic double layer and parasitic together with a resistance representing the inter-electrode medium. We did not include in this model access track resistance, as it is significantly lower than resistance R_M.

3.6.1 Cut-off Frequency

Based on the results reported in chapter 2, double-layer capacitance per unit of surface C_0 was extracted in PBS which, combined with the equation of the resistance of a coplanar sensor given in chapter 1, allows estimating the cut-off frequency f_c at which the system switches from the double-layer capacitive regime to the inter-electrode resistive regime. This estimation is important since it allows defining the lower limit at which the sample starts to be probed. It is given by the following equation:

$$f_c = \frac{1}{2\pi}\frac{\sigma_s}{C_0}\frac{1}{W}\frac{K(\sqrt{1-k^2})}{K(k)} \tag{3.4}$$

where K(k) is the complete elliptic integral of the first kind as defined in chapter 1. σ_s and W represents respectively the conductivity of the solution and the electrode width.

Therefore, with $C_0 = 21.1$ mF/m^2, a PBS conductivity σ_s of 1.6 S/m and the dimensions of the sensing electrodes (width of 20 µm and length of 10µm), the cut-off frequency is found to be of 158 kHz. However, experimental results show a cut-off frequency of around 216 kHz. This discrepancy can be linked to fabrication margins but is probably also due to the chemistry of saline solutions. Indeed, the conductivity together with the double-layer capacitance are both driven by the ionic concentration of PBS and, although our models consider the double layer through its capacitive impact on measurement, it might also impact the inter-electrode resistance by local ionic overconcentration, for example. However, to further study electrochemical effects at the interface of electrodes would require complex and time-consuming simulations which will not be addressed here.

The double-layer capacitance is proportional to the surface of the electrodes. It might therefore be tempting, in an effort to reduce the cut-off frequency, to increase the electrode size as it will decrease the capacitance impact on the impedance. However, such a design, even though with a wide measurement band, would not be sensitive enough to detect single cells as discussed in the next section.

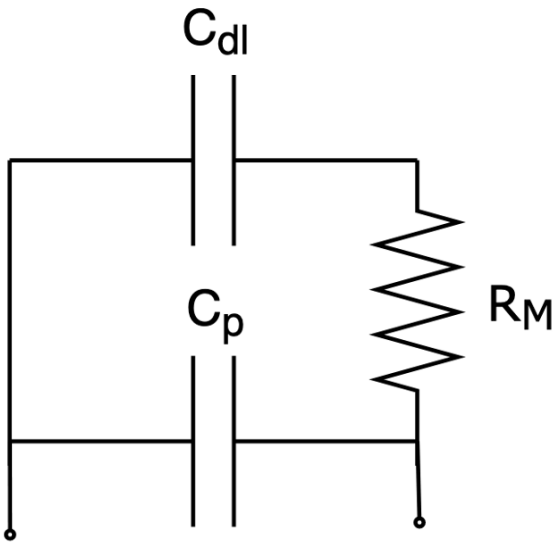

Figure 3.39: Equivalent electrical circuit model.

3.6.2 Device Sensitivity

In order to evaluate the sensitivity of the sensing electrodes, 3D models were developed (see figure 3.40) using Comsol Multiphysics (FEM Software). The model is composed of a 1.4 µm membrane with a single pore, two electrodes on each side of the pore and electrolytic medium above and below the membrane. A dielectric sphere of 10 µm diameter is added to the model to represent the capture of a cell in between the electrodes. The module Electrical Current was used to simulate the inter-electrode resistance within a medium of conductivity 1.6 S/m (PBS) while varying the electrode width and length. These simulations are therefore only representing the R_M component of the electrical model presented in figure 3.39. Following the FEM simulations, the sensitivity is then calculated using the following equation:

$$S = 100 \times \frac{R_{cell} - R_{empty}}{R_{empty}} \tag{3.5}$$

While varying both width and length at the same time, ranging from 5µm to 50µm and 10µm to 100µm respectively, it is first interesting to look at the evolution of sensitivity along the increase of electrode width with an arbitrarily fixed length as shown in figure 3.41a.

Indeed, as discussed previously and confirmed here, increasing indefinitely the width of electrodes to limit the impact of the double-layer capacitance is not doable since it will drastically deteriorate the performances of the sensor. Therefore, these simulations encourage us to find an optimum: the lowest electrode width at which both the sensitivity is the highest and the bandwidth wide enough for our sensing applications. This led to choosing a width of 20 µm at which the cut-off frequency

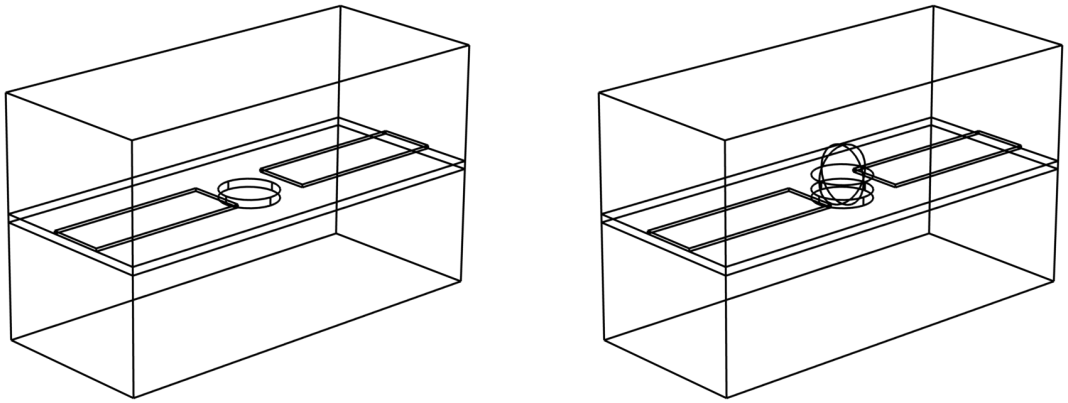

(a) **(b)**

Figure 3.40: 3D CAD model of the sensing electrodes on the filtrating membrane without (a) and with (b) the presence of a cell.

is inferior to 250 kHz (158 MHz). As a reminder, Eq. 3.4 shows that the cut-off frequency is only dependent on the width of the electrodes.

The same trend can be seen in figure 3.41b when varying the electrode length. However, since the length does not impact the cut-off frequency but only the sensitivity, we choose the smallest length possible (10 µm) while keeping a margin for the photolithography process. Thus, we expect a sensor sensitivity of 9% with the chosen dimensions.

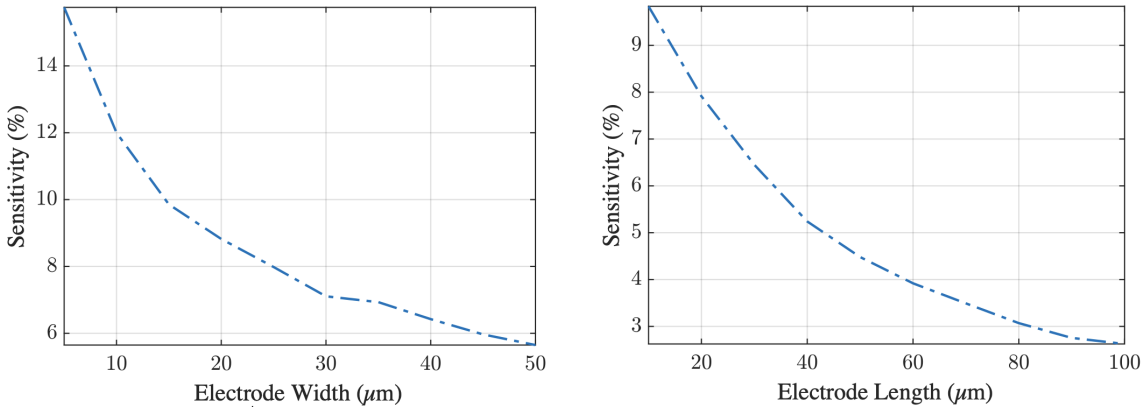

(a) **(b)**

Figure 3.41: Sensitivity of the device with (a) length of 10µm and varying width, (b) width of 20µm and varying length.

3.6.3 Parasitic Capacitance

Finally, following the discussion on cut-off frequency resulting from the double-layer capacitance and inter-electrode resistance, we herein investigate parasitic capacitances which might screen impedance measurement of the interelectrode region, inducing a second, higher frequency, cut-off limit, thus limiting the frequency bandwidth of our sensor.

Along design steps, simulations were led to evaluate the inter-electrode capacitance either through the substrate or the filtering membrane. Figure 3.42 shows the CAD model designed to simulate the potential parasitic effects using the Electrostatic module of Comsol.

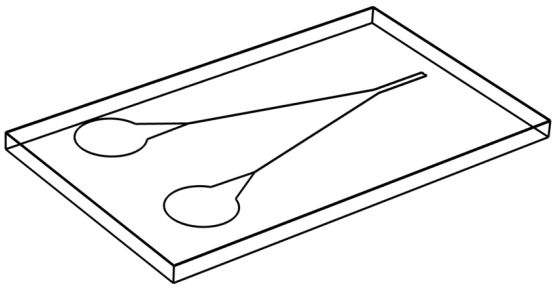

Figure 3.42: 3D CAD model of the sensing electrodes, contacts pads and access tracks.

Following these simulations, no parasitic effect seemed large enough to impact the impedance of the sensor (C_p=4 fF). However, reference experiments showed a much larger parasitic effect as shown in figure 3.37b (C_p ranging from 7 to 9 pF). This parasitic capacitance can be seen in figure 3.38 at high frequencies (above 1 MHz) and creates a second cut-off frequency, thus limiting the sensor bandwidth from 216 kHz to 1 MHz.

This effect was later investigated, and simulations showed a capacitance of 12 pF created in between electrodes and the silicon substrate acting as a terminal and the 1.4 µm bilayer dielectric membrane as an insulator. Although the silicon used as a substrate was not doped, using high resistivity silicon wafers would compensate for this parasitic effect. As discussed previously and shown in figure 3.38, the reduction in bandwidth induced by the upper cut-off frequency prevents the sensor from reaching a resistive regime: the phase angle reaches -65° at most, meaning that the measured impedance is still dominated by capacitance effects from both the double-layer capacitance and the parasitic capacitance. Further electrical experiments with cells spiked in PBS samples confirmed that the fabricated device was not sensitive to captured cells in between electrodes.

3.7 Conclusion and Perspectives

Following the fabrication of devices for in-situ single cell analysis on a filtering membrane, conclusions can be drawn regarding the fabrication process optimization, the 3D integration, the experimental platform together with the limitations of the sensor and the future developments.

3.7.1 Fabrication Process

Based on cleanroom developments and learning of the previous fabrication process discussed in chapter 2, two processes were developed.

The silicon process, although keeping the bilayer membrane, changes the supporting structure material and the electrode placement. These improvements drastically simplified the fabrication process while reducing the fabrication time. The main bottleneck of the fabrication process presented in 2 was the last step: devices release by wet etching. This step, due to the change of supporting structure material (from nickel to silicon) allowed us to transfer the device release within a plasma reactor. This last step, the silicon deep plasma etching, is still the limiting factor due to the wafer bonding needing for thermalization. However, this wafer bonding is currently done "by hand" and has a lot of margins for improvement.

Finally, the silicon process is, to date, the most advanced version of the devices using a 1.4µm thin membrane with integrated electrodes. The only addition which would be necessary for further electrical characterization is using a high resistivity silicon wafer substrate which would not need any change in the current fabrication process.

Looking at the glass process, it was developed related to the opportunity of the arrival of a new machine in the LAAS clean room. This fabrication process is, even though using identical clean-room techniques, opposite in philosophy to the silicon process. Indeed, selective laser ablation is a fast-prototyping technique which means that designs can be adapted, fabricated and tested in a very short timeframe. However, it does not allow for large batch production as the silicon process does and which would be required for acquiring significant biological experiments that usually requires a large number of experiments and therefore a large number of devices.

In the end, the glass process still requires developments but will surely offer many advantages for research purposes through fast-prototyping and the impressive capability in terms of aspect ratio of the machine.

Moreover, although many machines are available within the LAAS clean room, developing a process in a research environment also needs to consider the availability and the reliability of the equipment in order to obtain reproducible devices while having redundancy among other equipment in case of machine failure. As an example,

in the case of the silicon process, the choice was made to use previously fabricated membranes on conventional silicon wafers instead of fabricating new membrane on high resistivity silicon wafers due to furnaces issues.

3.7.2 Integration Technique

Along cleanroom developments discussed above, a Print Pause Print process at LAAS using SLA 3D printers was developed for the integration of glass coverslip and other microfabricated devices inside a 3D microfluidic chip. This led to the development of the integration chip presented in section 3.3 which, brought a live optical characterization which, as discussed in chapter 2, was needed for further capture analysis together with control for electrical measurements.

Indeed, this window allowed to characterize capture issues with cells rolling on the membrane which, following adjustments were corrected. Following this correction, image post-processing algorithm provided the precise and quantitative insight into single capture events.

Although we could not go further with electrical analysis due to parasitic effects within our devices, this window allowed to better understand capture kinetics. Moreover, in an effort to optimize capture efficiency of filtering membranes in a broad range of applications, membrane design can be tested through this fast-prototyping integration, therefore setting a baseline for further numerical model predictions.

Finally, as discussed in the previous section, the reliability of the equipment and reproducibility of the process is an important factor. In this specific application of the PPP process for device integration, the process is very robust: every integration is functional and matches the CAD design.

Moreover, it is transferable in between DWS printers and can be done on cheaper SLA printers such as FormLabs Printers. All in all, this process provides a great multipurpose qualitative and quantitative tool for filtering applications such as ours and more widely for microfluidic applications.

3.7.3 Electrical Developments and Automation

The experimental platform development was led along the device fabrication and integration. It allows a synchronous collection of optical and electrical data together with their post-processing along sample processing. The multiplexer design and fabrication were done by Fabrice Mathieu, Engineer at LAAS-CNRS.

Although biological electrical characterization could not go further in this work due to a parasitic capacitance preventing the sensor from reaching a resistive regime, the multiplexer was required for the platform automation and used for the reference measurements. It was also characterized on its own and showed great potential for future high frequency measurements.

The overall experimental platform fitted the needs for the envisioned characterization methods while being well though ergonomically and reliable.

3.7.4 Perspectives

As presented along this chapter, silicon devices together with their integration showed great potential for the study of capture kinetics and sample culture post-capture. However, parasitic effects limited the electrical characterization of biological samples. This limitation can be removed as discussed above through the selection of a more insulating silicon substrate.

On the other hand, glass-made device did not go through any characterization steps yet. Useful insights could be brought by such designs and on many levels. First, the thickness of the filtering structure while maintaining small pores makes it unique and studying the capture kinetics on these sieves will probably bring knowledge, not only on capture but maybe also on the captured cells or aggregates. Indeed, microchannels are commonly used to characterize cells and cells aggregate mechanical properties by aspiration while looking at the induced deformation. In such conditions, the fabricated glass device would bring a high density of transparent parallel microchannels which could enable simultaneous cell mechanical characterization of large populations.

Moreover, since both silicon and glass designs are electrically identical apart from the supporting structure which is causing the parasitic electrical effects on the silicon devices, these effects wouldn't be present on the glass devices, giving us good hope that this design would be able to further characterize biological samples electrically.

Finally, the Selective Laser Etching offers much more design freedom due to its 3D definition nature, hence, offering many possibilities to fabricate a platform allowing the user to retrieve biological elements of interest from a sample, cultivate and/or characterize them in multiple ways and in real time during sample processing or along long periods of cell culture.

4 General Conclusion

Filtrating a complex medium, containing a large quantity of entities in suspension is a technological challenge as soon as a specific element needs to be retained among a wide population of resembling items. In a medical context where biomarkers inside a body fluid are targeted, this problematic of the specificity of the filtration is combined with the scarcity of the biomarkers of interest. These constraints are very well exemplified in the case of the filtration of Circulating Tumor Cells in whole blood for precision diagnostics in oncology. A few CTCs per milliliter of blood needs to be retained by the sieve while millions of normal white blood cells and billions of red blood cells found in the same volume are expected to pass through. This high level of specificity and precision appeals for innovative methods and controls of the filtration process. In this research, we have combined the precision of microfabrication methods for generating such filtering devices and we have integrated electrical sensors for in-situ monitoring of the filtration process. These innovative solutions for improving and monitoring sample filtration of complex media may hold the key to many health-related and environmental issues. Hence, to further extend the usability of microfabricated filters, the integration of electrical sensing capability to the filtering membranes has been the driving focus of this research work.

Following the theoretical description of electrical sensing concepts in Chapter 1, Chapter 2 described the conceptualization and fabrication of high precision filtering membranes with integrated electrodes. These microfabricated devices targeted the filtration of whole human blood for the retention of circulating cells and the in-situ detection of cell density on the sieve. Both the cell trapping, and the electrical detection were demonstrated in a medium as complex as human whole blood. Although the usability inside whole blood and the functionalities of the fabricated devices were demonstrated, improvements are still required to obtain more interpretable information through the recording of the electrical signal changes. Even though the evolution of the cellular density can be tracked, thus giving access to the rate at which the filter gets filled by the retained cells during filtration, it was, however, not possible to enumerate individual capture events nor to identify the phenotype of the

captured cells based on their electrical signature.

Chapter 3 addressed new approaches and technologies for evaluating if these objectives of individual cell enumeration and phenotyping could be achievable. For that purpose, we have improved the fabrication process yield using new techniques and processes. In an exploratory research perspective, we also designed systems where optical characterization of filtration events could be recorded at the same time as electrical sensing was performed. It was for us, the only possibility to discover from measured electrical signals, the cues that could be used for identifying the nature of the cell. We have developed two different fabrication processes, together with the addition of 3D printing technic in the integration workflow to obtain a cross-modal information combining optical imaging and single cell electrical impedance characterization. The produced devices turned out to be functional. A full instrumentation platform was built to correlate images of single cell capture under flow together with electrical sensing. Unfortunately, up to now the useful frequency domain for getting the electrical phenotype of the captured cell was not accessible to the measurements due to an unexpected parasitic coupling appearing in the devices. Remediation solutions have been proposed for both silicon-based and glass-based devices, but the final well-designed systems could not be delivered before the end of this PhD research. As a consequence, even if single cell measurements and cell electrical phenotyping seems feasible, for the moment we have not demonstrated that electrical in-situ single cell analysis could be used for discriminating the tumoral character of captured cells at the sieve surface. This thus remains an open issue for this kind of technology.

All-in-all, this work demonstrated through multiple processes, the integration of sensing electrodes on a thin filtering membrane. The fabricated devices allowed to evaluate in real time the cell density on the filtering membrane and obtain the first insights of cell capture kinetics within whole blood through impedance spectroscopy in an optically enclosed system. Moreover, device optimization for single cell analysis led to the development of new processes using glass and silicon structuration technic over high aspect ratios with spatial resolutions within the order of magnitude of cell dimensions. However, these optimizations did not allow us to identify single cell capture events nor to analyze the phenotype of trapped cells due to electrical parasitic effects masking the researched signatures. Indeed, designing a broad frequency range sensor requires to combine multiple effects at different scales. Moreover, widening the measurement band leads to a higher sensitivity to parasitic capacitances and environmental electromagnetic perturbations at high frequencies. Hence, the ability of such a sensor to be sensitive enough to detect and analyze single cells within a crowded sample such as whole blood while using wide-band measurements will still require further optimization to be achieved.

Such optimization needs to consider multiple aspects: design, fabrication steps, experimental platform and turned out to finally require implementation through multiple iterations with new effects appearing along each step and impacting the final sensor performances. The success of this project may therefore lie on the number of iterations and resources that one is willing to put in this optimization.

My personal opinion is that such a sensor could be developed following a delicate engineering optimization. However, its costs, in terms of resources together with its environmental impact needs to be cautiously considered beforehand.

This work also brought new insights in the academic field for my research team at LAAS-CNRS through the development and optimization of technological process steps which are then shared within the LAAS cleanroom facility. Moreover, the development of a multi-modal experimental platform together with the measurement and automation setup allows for reliable and ergonomic experiments. This platform is available to LAAS lab experimenters and technicians and, through its modularity, could benefit to projects outside of the liquid biopsy scope through additional measurement tools, thus allowing addressing current microfiltration challenges.

SmartCatch may, however, not benefit from the integrated cell density detection in its current form. Indeed, the complex fabrication process together with measurement tools would drastically increase the cost per device. However, developments surrounding the cross-modal experimental platform are of great interest for the comprehension of the inner mechanisms of cell capture under the commercialized sieves of the company. They could be used by the research and development department of the company to bring capture kinetics and mechanisms from a single cell scale to a large filtering membrane, thus allowing precision studies of both local and macro capture effects. These research devices could be essential for optimizing the design of the filtration pores, their dimensions and global architecture together with the fluidics conditions for operating safe and specific cell capture, combining high capture efficiency, cell viability and low contamination levels.

Bibliography

[1] Robert C. Hale et al. “A Global Perspective on Microplastics”. en. In: *Journal of Geophysical Research: Oceans* 125.1 (2020), e2018JC014719. DOI: 10.1029/2018JC014719.

[2] Merle Schlawinsky et al. “Improved microplastic processing from complex biological samples using a customized vacuum filtration apparatus”. en. In: *Limnology and Oceanography: Methods* 20.9 (2022), pp. 553–567. DOI: 10.1002/lom3.10504.

[3] Heather A. Leslie et al. “Discovery and quantification of plastic particle pollution in human blood”. en. In: *Environment International* 163 (2022), p. 107199. DOI: 10.1016/j.envint.2022.107199.

[4] Yunxiao Yang et al. “Detection of Various Microplastics in Patients Undergoing Cardiac Surgery”. In: *Environmental Science & Technology* 57.30 (2023), pp. 10911–10918. DOI: 10.1021/acs.est.2c07179.

[5] Hayal Çobanoğlu et al. “Genotoxic and cytotoxic effects of polyethylene microplastics on human peripheral blood lymphocytes”. In: *Chemosphere* 272 (2021), p. 129805. DOI: 10.1016/j.chemosphere.2021.129805.

[6] Naixin Qian et al. “Rapid single-particle chemical imaging of nanoplastics by SRS microscopy”. en. In: *Proceedings of the National Academy of Sciences* 121.3 (2024), e2300582121. DOI: 10.1073/pnas.2300582121.

[7] Gurusamy Kutralam-Muniasamy et al. “Microplastic diagnostics in humans: “The 3Ps” Progress, problems, and prospects”. In: *Science of The Total Environment* 856 (2023), p. 159164. DOI: 10.1016/j.scitotenv.2022.159164.

[8] Tae Lee, Thomas F. Speth, and Mallikarjuna N. Nadagouda. “High-pressure membrane filtration processes for separation of Per- and polyfluoroalkyl substances (PFAS)”. In: *Chemical Engineering Journal* 431 (2022), p. 134023. DOI: 10.1016/j.cej.2021.134023.

[9] Shobha Mantripragada, Sherine O. Obare, and Lifeng Zhang. “Addressing Short-Chain PFAS Contamination in Water with Nanofibrous Adsorbent/Filter Material from Electrospinning”. In: *Accounts of Chemical Research* 56.11 (2023), pp. 1271–1278. DOI: 10.1021/acs.accounts.2c00591.

[10] Tasha Stoiber et al. “PFAS in drinking water: an emergent water quality threat”. en. In: (2020).

[11] Oskar Hansson et al. “The Alzheimer’s Association appropriate use recommendations for blood biomarkers in Alzheimer’s disease”. en. In: *Alzheimer’s & Dementia* 18.12 (2022), pp. 2669–2686. DOI: 10.1002/alz.12756.

[12] Md Shahjahan et al. “Blood biomarkers as diagnostic tools: An overview of climate-driven stress responses in fish”. In: *Science of The Total Environment* 843 (2022), p. 156910. DOI: 10.1016/j.scitotenv.2022.156910.

[13] Virginia F J Newcombe et al. “Post-acute blood biomarkers and disease progression in traumatic brain injury”. en. In: ().

[14] GwendolynL. Gilbert et al. “PREVENTION OF TRANSFUSION-ACQUIRED CYTOMEGALOVIRUS INFECTION IN INFANTS BY BLOOD FILTRATION TO REMOVE LEUCOCYTES”. In: *The Lancet*. Originally published as Volume 1, Issue 8649 333.8649 (1989), pp. 1228–1231. DOI: 10.1016/S0140-6736(89)92330-1.

[15] Vincent M. Tutino et al. “Gene expression profiles of ischemic stroke clots retrieved by mechanical thrombectomy are associated with disease etiology”. en. In: *Journal of NeuroInterventional Surgery* 15.e1 (2023), e33–e40. DOI: 10.1136/neurintsurg-2022-018898.

[16] Claudio Ronco and William R. Clark. “Haemodialysis membranes”. en. In: *Nature Reviews Nephrology* 14.6 (2018), pp. 394–410. DOI: 10.1038/s41581-018-0002-x.

[17] Ernesto Martín-Núñez et al. “Klotho expression in peripheral blood circulating cells is associated with vascular and systemic inflammation in atherosclerotic vascular disease”. en. In: *Scientific Reports* 12.1 (2022), p. 8422. DOI: 10.1038/s41598-022-12548-z.

[18] Cuiliu Liu et al. “Blood-based liquid biopsy: Insights into early detection and clinical management of lung cancer”. In: *Cancer Letters* 524 (2022), pp. 91–102. DOI: 10.1016/j.canlet.2021.10.013.

[19] P W Rand et al. “pH and blood viscosity.” en. In: *Journal of Applied Physiology* 25.5 (1968), pp. 550–559. DOI: 10.1152/jappl.1968.25.5.550.

[20] Klaus Pantel and Catherine Alix-Panabières. “Crucial roles of circulating tumor cells in the metastatic cascade and tumor immune escape: biology and clinical translation”. en. In: *Journal for ImmunoTherapy of Cancer* 10.12 (2022), e005615. DOI: 10.1136/jitc-2022-005615.

[21] Brandon M. Lehrich et al. “Battle of the Biopsies: Role of tissue and liquid biopsy in hepatocellular carcinoma”. English. In: *Journal of Hepatology* 0.0 (2023). DOI: 10.1016/j.jhep.2023.11.030.

[22] Marius Ilie et al. ““Sentinel” Circulating Tumor Cells Allow Early Diagnosis of Lung Cancer in Patients with Chronic Obstructive Pulmonary Disease”. en. In: *PLoS ONE* 9.10 (2014). Ed. by Vladimir V. Kalinichenko, e111597. DOI: 10.1371/journal.pone.0111597.

[23] Dannel Yeo et al. “Exploring the Clinical Utility of Pancreatic Cancer Circulating Tumor Cells”. en. In: *International Journal of Molecular Sciences* 23.3 (2022), p. 1671. DOI: 10.3390/ijms23031671.

[24] Klaus Pantel and Catherine Alix-Panabières. "Liquid biopsy and minimal residual disease — latest advances and implications for cure". en. In: *Nature Reviews Clinical Oncology* 16.7 (2019), pp. 409–424. DOI: 10.1038/s41571-019-0187-3.

[25] Yukiko Kiniwa et al. "Usefulness of monitoring circulating tumor cells as a therapeutic biomarker in melanoma with BRAF mutation". en. In: *BMC Cancer* 21.1 (2021), p. 287. DOI: 10.1186/s12885-021-08016-y.

[26] Gabor Jarvas et al. "Modification of Hemodialysis Membranes for Efficient Circulating Tumor Cell Capture for Cancer Therapy". en. In: *Molecules* 26.16 (2021), p. 4845. DOI: 10.3390/molecules26164845.

[27] Menno Tamminga et al. "Leukapheresis increases circulating tumour cell yield in non-small cell lung cancer, counts related to tumour response and survival". en. In: *British Journal of Cancer* 126.3 (2022), pp. 409–418. DOI: 10.1038/s41416-021-01634-0.

[28] Jonathan G. Hiller et al. "Perioperative events influence cancer recurrence risk after surgery". en. In: *Nature Reviews Clinical Oncology* 15.4 (2018), pp. 205–218. DOI: 10.1038/nrclinonc.2017.194.

[29] Francesca Chemi et al. "Pulmonary venous circulating tumor cell dissemination before tumor resection and disease relapse". en. In: *Nature Medicine* 25.10 (2019), pp. 1534–1539. DOI: 10.1038/s41591-019-0593-1.

[30] *Eukaryote | Definition, Structure, & Facts | Britannica*. en. 2023.

[31] K. R. Foster and H. P. Schwan. "Dielectric properties of tissues and biological materials: a critical review". eng. In: *Critical Reviews in Biomedical Engineering* 17.1 (1989), pp. 25–104.

[32] Hugo Fricke and Sterne Morse. "The Electric Resistance and Capacity of Bood for Frequencies Between 800 and 4½ Million Cycles". en. In: *Journal of General Physiology* 9.2 (1925), pp. 153–167. DOI: 10.1085/jgp.9.2.153.

[33] B. Rajewsky and H. Schwan. "Die Dielektrizitätskonstante und Leitfähigkeit des Blutes bei ultrahohen Frequenzen". de. In: *Naturwissenschaften* 35.10 (1948), pp. 315–316. DOI: 10.1007/BF00626639.

[34] Orjan G Martinsen and Sverre Grimnes. *Bioimpedance and Bioelectricity Basics*. English. Oxford: Elsevier Science, 2014.

[35] Peter Josef William Debye. *Polar molecules*. eng. Dover books explaining science and mathematics. New York: Dover, 1960.

[36] William D. Hurt. "Multiterm Debye Dispersion Relations for Permittivity of Muscle". In: *IEEE Transactions on Biomedical Engineering* BME-32.1 (Jan. 1985), pp. 60–64. DOI: 10.1109/TBME.1985.325629.

[37] S Gabriel, R W Lau, and C Gabriel. "The dielectric properties of biological tissues: III. Parametric models for the dielectric spectrum of tissues". en. In: *Physics in Medicine and Biology* 41.11 (1996), pp. 2271–2293. DOI: 10.1088/0031-9155/41/11/003.

[38] Ina Turcan and Marius Andrei Olariu. "Dielectrophoretic Manipulation of Cancer Cells and Their Electrical Characterization". In: *ACS Combinatorial Science* 22.11 (Nov. 2020), pp. 554–578. DOI: 10.1021/acscombsci.0c00109.

[39] Xiao-Bo Wang et al. "Changes in Friend murine erythroleukaemia cell membranes during induced differentiation determined by electrorotation". en. In: *Biochimica et Biophysica Acta (BBA) - Biomembranes* 1193.2 (1994), pp. 330–344. DOI: 10.1016/0005-2736(94)90170-8.

[40] Peter R. C. Gascoyne et al. "Correlations between the dielectric properties and exterior morphology of cells revealed by dielectrophoretic field-flow fractionation: General". en. In: *ELECTROPHORESIS* 34.7 (2013), pp. 1042–1050. DOI: 10.1002/elps.201200496.

[41] Peter Gascoyne and Sangjo Shim. "Isolation of Circulating Tumor Cells by Dielectrophoresis". en. In: *Cancers* 6.1 (2014), pp. 545–579. DOI: 10.3390/cancers6010545.

[42] *Cell Lines in the In Vitro Screen | NCI-60 Human Tumor Cell Lines Screen | Discovery & Development Services | Developmental Therapeutics Program (DTP).*

[43] Ezekiel O. Adekanmbi and Soumya K. Srivastava. "Dielectric characterization of bioparticles via electrokinetics: The past, present, and the future". en. In: *Applied Physics Reviews* 6.4 (Dec. 2019), p. 041313. DOI: 10.1063/1.5113709.

[44] Hugo Fricke. "The Complex Conductivity of a Suspension of Stratified Particles of Spherical or Cylindrical Form". en. In: *The Journal of Physical Chemistry* 59.2 (1955), pp. 168–170. DOI: 10.1021/j150524a018.

[45] Kathrin Benson, Sandra Cramer, and Hans-Joachim Galla. "Impedance-based cell monitoring: barrier properties and beyond". In: *Fluids and Barriers of the CNS* 10.1 (2013), p. 5. DOI: 10.1186/2045-8118-10-5.

[46] M. Amini, J. Hisdal, and H. Kalvøy. "Applications of bioimpedance measurement techniques in tissue engineering". en. In: *Journal of Electrical Bioimpedance* 9.1 (2018), pp. 142–158. DOI: 10.2478/joeb-2018-0019.

[47] Balaji Srinivasan et al. "TEER Measurement Techniques for In Vitro Barrier Model Systems". In: *SLAS Technology*. Special Issue: Microengineered Cell- and Tissue-Based Assays for Drug Screening and Toxicology Applications (Part 1 of 2) 20.2 (2015), pp. 107–126. DOI: 10.1177/2211068214561025.

[48] Sorel E. De León, Aleta Pupovac, and Sally L. McArthur. "Three-Dimensional (3D) cell culture monitoring: Opportunities and challenges for impedance spectroscopy". en. In: *Biotechnology and Bioengineering* 117.4 (2020), pp. 1230–1240. DOI: 10.1002/bit.27270.

[49] Julien Claudel et al. "Interdigitated Sensor Optimization for Blood Sample Analysis". en. In: *Biosensors* 10.12 (2020), p. 208. DOI: 10.3390/bios10120208.

[50] Herman P Schwan. "ELECTRICAL PROPERTIES OF TISSUE AND CELL SUSPENSIONS". en. In: ().

[51] Tao Sun and Hywel Morgan. "Single-cell microfluidic impedance cytometry: a review". en. In: *Microfluid Nanofluid* (2010).

[52] W. Olthuis, W. Streekstra, and P. Bergveld. “Theoretical and experimental determination of cell constants of planar-interdigitated electrolyte conductivity sensors”. en. In: *Sensors and Actuators B: Chemical* 24.1-3 (1995), pp. 252–256. DOI: 10.1016/0925-4005(95)85053-8.

[53] Jianzhong Wu. “Understanding the Electric Double-Layer Structure, Capacitance, and Charging Dynamics”. In: *Chemical Reviews* 122.12 (2022), pp. 10821–10859. DOI: 10.1021/acs.chemrev.2c00097.

[54] Hugo Fricke. “XXXIII. The theory of electrolytic polarization”. In: *The London, Edinburgh, and Dublin Philosophical Magazine and Journal of Science* 14.90 (1932), pp. 310–318. DOI: 10.1080/14786443209462064.

[55] K. S. Cole. “Permeability and Imperbeability of Cell Membranes for Ions”. en. In: *Cold Spring Harbor Symposia on Quantitative Biology* 8.0 (1940), pp. 110–122. DOI: 10.1101/SQB.1940.008.01.013.

[56] C.H. Hsu and F. Mansfeld. “Technical Note: Concerning the Conversion of the Constant Phase Element Parameter Y0 into a Capacitance”. In: *Corrosion* 57.09 (2001).

[57] Andrzej Lasia. “The Origin of the Constant Phase Element”. en. In: *The Journal of Physical Chemistry Letters* 13.2 (2022), pp. 580–589. DOI: 10.1021/acs.jpclett.1c03782.

[58] Guigen Zhang. “Simulating the electrical double layer capacitance”. In: *Excerpt from Proceedings of the COMSOL Conference. Boston*. 2010.

[59] Dahiana Mojena-Medina et al. “Real-Time Impedance Monitoring of Epithelial Cultures with Inkjet-Printed Interdigitated-Electrode Sensors”. en. In: *Sensors* 20.19 (2020), p. 5711. DOI: 10.3390/s20195711.

[60] Subhas Chandra Mukhopadhyay et al., eds. *Interdigital Sensors: Progress over the Last Two Decades*. en. Vol. 36. Smart Sensors, Measurement and Instrumentation. Cham: Springer International Publishing, 2021. DOI: 10.1007/978-3-030-62684-6.

[61] J. Claudel et al. “Optimization of Interdigitated Sensor Characteristics”. en. In: *Interdigital Sensors: Progress over the Last Two Decades*. Ed. by Subhas Chandra Mukhopadhyay et al. Smart Sensors, Measurement and Instrumentation. Cham: Springer International Publishing, 2021, pp. 91–122. DOI: 10.1007/978-3-030-62684-6_5.

[62] H. Samavati et al. “Fractal capacitors”. In: *IEEE Journal of Solid-State Circuits* 33.12 (1998), pp. 2035–2041. DOI: 10.1109/4.735545.

[63] Elise Bou. “Micro-dispositifs pour la biopsie liquide : vers la capture et détection intégrées de biomarqueurs cellulaires tumoraux”. fr. PhD thesis. INSA de Toulouse, 2020.

[64] Max Costa, Maria P. Abbracchio, and Jeannie Simmons-Hansen. “Factors influencing the phagocytosis, neoplastic transformation, and cytotoxicity of particulate nickel compounds in tissue culture systems”. In: *Toxicology and Applied Pharmacology* 60.2 (1981), pp. 313–323. DOI: 10.1016/0041-008X(91)90234-6.

[65] K. Zitter, H. Plenk, and H. Strassl. “Tissue and cell reactions in vivo and in vitro to different metals for dental implant”. In: *Dental implants. C. Hanser, Miinchen* 15 (1980).

[66] H. Zitter and H. Plenk. “The electrochemical behavior of metallic implant materials as an indicator of their biocompatibility”. en. In: *Journal of Biomedical Materials Research* 21.7 (1987), pp. 881–896. DOI: 10.1002/jbm.820210705.

[67] M. E. Kaighn et al. “Establishment and characterization of a human prostatic carcinoma cell line (PC-3)”. eng. In: *Investigative Urology* 17.1 (1979), pp. 16–23.

[68] Osamu Shimomura, Frank H. Johnson, and Yo Saiga. “Extraction, Purification and Properties of Aequorin, a Bioluminescent Protein from the Luminous Hydromedusan, Aequorea”. en. In: *Journal of Cellular and Comparative Physiology* 59.3 (1962), pp. 223–239. DOI: 10.1002/jcp.1030590302.

[69] Lakshmi Balasubramaniam, René-Marc Mège, and Benoit Ladoux. “Active forces modulate collective behaviour and cellular organization”. In: *Comptes Rendus. Biologies* 344.4 (2021), pp. 325–335. DOI: 10.5802/crbiol.65.

[70] Laura Dean. “Blood and the cells it contains”. en. In: *Blood Groups and Red Cell Antigens [Internet]*. National Center for Biotechnology Information (US), 2005.

[71] Volker Hartenstein. “Blood Cells and Blood Cell Development in the Animal Kingdom”. en. In: *Annual Review of Cell and Developmental Biology* 22.1 (2006), pp. 677–712. DOI: 10.1146/annurev.cellbio.22.010605.093317.

[72] M. Bessis. “Red Cell Shapes. An Illustrated Classification and its Rationale”. en. In: *Red Cell Shape*. Ed. by Marcel Bessis, Robert I. Weed, and Pierre F. Leblond. Berlin, Heidelberg: Springer, 1973, pp. 1–25. DOI: 10.1007/978-3-642-88062-9_1.

[73] H A Krebs. “Chemical Composition of Blood Plasma and Serum”. en. In: *Annual Review of Biochemistry* 19.1 (1950), pp. 409–430. DOI: 10.1146/annurev.bi.19.070150.002205.

[74] E. W. Errill. “Rheology of blood”. In: *Physiological Reviews* 49.4 (1969), pp. 863–888. DOI: 10.1152/physrev.1969.49.4.863.

[75] R. S. Rivlin and Eric Keightley Rideal. “The hydrodynamics of non-Newtonian fluids. I”. In: *Proceedings of the Royal Society of London. Series A. Mathematical and Physical Sciences* 193.1033 (1947), pp. 260–281. DOI: 10.1098/rspa.1948.0044.

[76] Katherine Courchaine and Sandra Rugonyi. “Quantifying blood flow dynamics during cardiac development: demystifying computational methods”. In: *Philosophical Transactions of the Royal Society B: Biological Sciences* 373.1759 (2018), p. 20170330. DOI: 10.1098/rstb.2017.0330.

[77] M. M. Wintrobe. “A simple and accurate hematocrit”. In: *The Journal of Laboratory and Clinical Medicine* 15.3 (1929), pp. 287–289.

[78] Joseph J. McGovern, Alan Richardson Jones, and Arthur G. Steinberg. “The Hematocrit of Capillary Blood”. In: *New England Journal of Medicine* 253.8 (1955), pp. 308–312. DOI: 10.1056/NEJM195508252530802.

[79] Thomas C Halsey and Michael Leibig. “The double layer impedance at a rough surface: Theoretical results”. In: *Annals of Physics* 219.1 (1992), pp. 109–147. DOI: 10.1016/0003-4916(92)90314-C.

[80] Thomas Jänsch, Jens Wallauer, and Bernhard Roling. “Influence of Electrode Roughness on Double Layer Formation in Ionic Liquids”. In: *The Journal of Physical Chemistry C* 119.9 (2015), pp. 4620–4626. DOI: 10.1021/jp512617j.

[81] Alexei A. Kornyshev. “Double-Layer in Ionic Liquids: Paradigm Change?” In: *The Journal of Physical Chemistry B* 111.20 (2007), pp. 5545–5557. DOI: 10.1021/jp067857o.

[82] Matthieu Sagot et al. “Bio-Impedance Spectroscopy of Retained Cells Using a Micro-Perforated Sensing Membrane Filtrating Whole Blood Samples under High Flowrate”. eng. In: *Biosensors* 13.12 (2023), p. 996. DOI: 10.3390/bios13120996.

[83] Alejandro Kayum Jimenez Zenteno. “Micro-dispositifs pour l’isolement des cellules tumorales circulantes en routine clinique”. en. These de doctorat. Université de Toulouse, Université Toulouse III - Paul Sabatier, 2018.

[84] L. V. Keldysh. “Ionization in the field of a strong electromagnetic wave”. en. In: *Selected Papers of Leonid V Keldysh*. WORLD SCIENTIFIC, 1965, pp. 56–63. DOI: 10.1142/9789811279461_0008.

[85] Chris B. Schaffer, André Brodeur, and Eric Mazur. “Laser-induced breakdown and damage in bulk transparent materials induced by tightly focused femtosecond laser pulses”. en. In: *Measurement Science and Technology* 12.11 (2001), p. 1784. DOI: 10.1088/0957-0233/12/11/305.

[86] C. Hnatovsky et al. “Fabrication of microchannels in glass using focused femtosecond laser radiation and selective chemical etching”. en. In: *Applied Physics A* 84.1-2 (2006), pp. 47–61. DOI: 10.1007/s00339-006-3590-4.

[87] Yasuhiko Shimotsuma et al. “Self-Organized Nanogratings in Glass Irradiated by Ultrashort Light Pulses”. en. In: *Physical Review Letters* 91.24 (2003), p. 247405. DOI: 10.1103/PhysRevLett.91.247405.

[88] P. Stampfli. “Electronic excitation and structural stability of solids”. In: *Nuclear Instruments and Methods in Physics Research Section B: Beam Interactions with Materials and Atoms* 107.1 (1996), pp. 138–145. DOI: 10.1016/0168-583X(96)80046-2.

Nickel-Based Devices Fabrication Process

The fabrication process is described through 10 main steps. It includes 6 masks (N1 to N6) with respectively 6 UV photolithography steps.

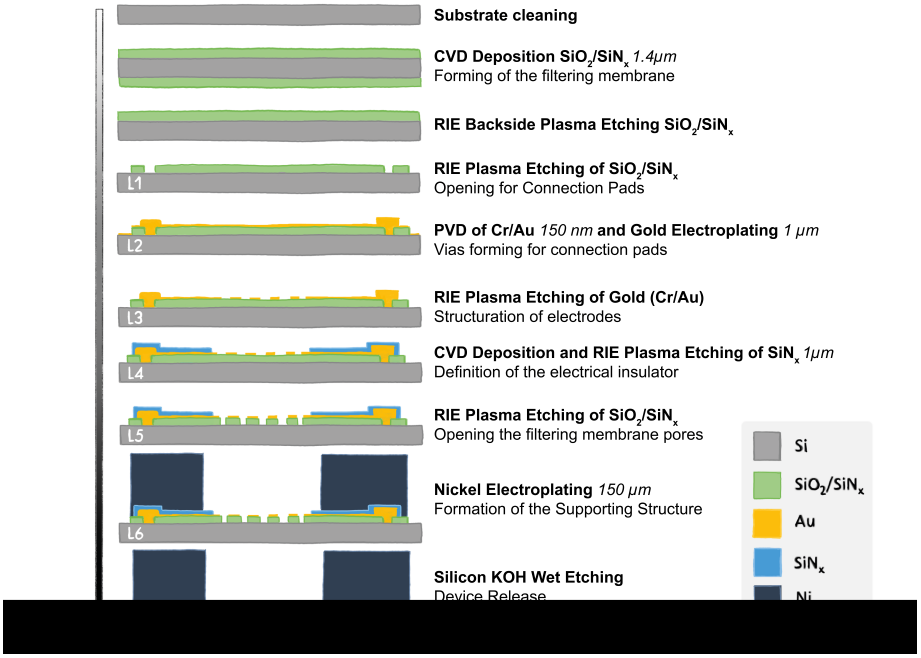

Figure 1: Schematic representation of the different steps of the microfabrication process for devices with integrated electrodes. Diagrams are not to scale. The electrolytic deposition of nickel is conformal, i.e. it follows the topography of the substrate on which it is deposited; this feature is not shown in the diagram.

1. **Substrate cleaning**. A 4-inch silicon wafer is cleaned in a piranha solution (50% H2SO4 + 50% H2O2). Deoxidation is then performed in a 5% HF solution.
2. **Chemical vapor deposition**. Thermal oxidation is performed at 1070 °C on the substrate to obtain an 800 nm SiO_2 layer. A 600 nm SiN_x film is then deposited at 750°C by LPCVD. These deposits are made on both sides of the wafer at the same time.
3. **RIE Backside etching**. The bilayer membrane (SiO_2/SiN_x) plasma etching is performed on the backside of the wafer and uses trifluoromethane (CHF_3, 60 cm^3/min) and dioxygen (O_2, 6 cm^3/min) to etch 0.6 µm silicon nitride and

0.8 µm silicon dioxide successively. The plasma etching takes 20 minutes at a sample temperature of -10°C and with a RF power of 60 W to generate the plasma and an ICP power of 1000 W with a reactor residual pressure of 7,6 mT.

4. **Opening of the connection pads (L1)**. An O_2 plasma (time: 5 minutes, power: 800 W, flow rate: 400 cm^3/min) is operated on the wafer in order to eliminate possible organic residues. A hexamethyldisilazane (HMDS) deposit is performed on the wafer to ensure the adhesion of the resist on the oxidized surface. A negative resist, AZ15NXT, is spin-coated (speed: 2000 rpm/min, acceleration: 4000 rpm/min^2, time: 30 seconds) with annealing at 110°C for 2 minutes followed by a trimming of the resist with acetone. UV exposure is performed with a dose of 250 mJ/cm^2 in hard contact, followed by 1 min of post-exposure bake at 120°C. The resulting resist thickness is 9 µm. After resist development, RIE etching is performed in an ICP reactor with the same recipe as the previous membrane etching step. Using the resist pattern as an etching mask, the removal of the resist is performed in an NF52 bath at 80°C for 5 minutes. An O_2 plasma (time: 5 minutes, power: 800 W, flow rate: 1000 cm^3/min) is performed to remove possible resist and solvent residues.

5. **Physical Vapor Deposition followed by Electroplating of contact pads (L2)**. A seed layer consisting of a bilayer of Chromium and Gold of respectively 50 nm and 100 nm is deposited by thermal evaporation on the wafer. An O_2 plasma (time: 2 minutes, power: 200 W, flow rate: 400 cm^3/min) is performed on the wafer. A negative resist, AZ15NXT is coated with a spinning machine (speed: 2000 rpm/min, acceleration: 4000 rpm/min^2, time: 30 seconds). The annealing is done at 110°C for 2 minutes. The resulting resist thickness is 9 µm. UV exposure is performed with a dose of 290 mJ/cm^2 in hard contact. Post-exposure curing was performed at 120°C for 1 minute. After the development of the resist, an O_2 plasma is performed on the wafer (time: 2 minutes, power: 200 W, flow rate: 400 cm^3/min) to remove all resist leftovers. A 1 µm gold electroplating is performed. The resist is removed with an NF52 bath at 80°C for 5 min and an O_2/CF_4 plasma (time: 2 min, power: 200 W, flow rates: 200 cm^3/min for O_2 and 40 cm^3/min for CF_4).

6. **RIE Plasma etching of seed layer for electrode definition (L3)**. As previously described, the wafer is spin-coated with an AZ15NXT negative resist, exposed to UV and developed. The Cr/Au seed layer of 150 nm is then etched with argon plasma (Ar, 30 cm^3/min) at a sample temperature of 20°C for 3 minutes with a RF power of 100 W and an ICP power of 600 W with a reactor residual pressure of 5 mT. This etching step induces gold sputtering over the resist. The resist stripping is therefore done within a NF52 solution for 5 minutes with the wafer placed upside down and in an ultrasonic bath. Finally, an O_2/CF_4 plasma is done to remove resist leftovers (time: 2 min, power: 200 W, flow rates: 200 cm^3/min for O_2 and 40 cm^3/min for CF_4).

7. **CVD Deposition and RIE Plasma etching of Si_3N_4 (L4)**. A 1 µm layer of Si_3N_4 is deposited through a PECVD technique on the wafer at 300°C in 10 minutes. The deposition is followed by the spin coating, UV exposure and development of an AZ15NXT resist as described previously. Finally, etching of the electrical insulator (Si_3N_4) uses trifluoromethane (CHF_3, 20 cm^3/min), nitrogen (N_2, 10 cm^3/min), argon (Ar, 100 cm^3/min) and dioxygen (O_2, 10 cm^3/min). The process step takes 8 min for 1 µm at a temperature of 20°C and with a RF power of 35 W and ICP power of 300 W with a reactor residual pressure of 25 mT. Using the resist pattern as an etching mask, the removal of the resist is performed in an NF52 bath heated at 80°C for 5 minutes. An O_2 plasma (time: 5 minutes, power: 800 W, flow rate: 1000 cm^3/min) is performed to remove possible resist and solvent residues.

8. **Opening the pores of the filtering membrane (L5)**. This step is identical to the one described in point 4 for the UV photolithography and the etching process.

9. **Growth of the supporting structure (L6)**. A seed layer consisting of a bilayer of titanium and copper is sputtered onto the wafer to obtain a conformal deposit on the structured surface. Two dry WBR-2100 films, 100 µm thick, are laminated to the wafer at 50°C (pressure: 2.5 bars, speed $<$ 0.5 m/s). Annealing is performed at 65°C for 10 min. UV exposure is performed with a dose of 1100 mJ/cm^2 in vacuum contact. Post-exposure baking is performed at 105°C for 2 min. The development is carried out in a sodium carbonate solution $NaCo_3$ with agitation for about 15 min. After development of the resist, a CF_4/O_2 plasma (time: 2 min, power: 200 W, flow rate: 400 cm^3/min) is performed on the wafer. Electroplating of 150 µm of nickel is then performed (time: 214 min, current density: 4 A/dm^2). The resist is removed with acetone, followed by a NF52 bath at 80°C for 30 min.

10. **Etching of the silicon substrate and release of the devices**. The silicon substrate is etched within a KOH solution. The released microdevices are then rinsed in a DI water bath. The etching of the seed layer is done piece by piece. Copper is etched with a diluted piranha solution (1% H_2SO_4 + 1% H_2O_2+98% H_2O) and titanium is etched with a 5% HF buffer. The microdevices are then rinsed individually with DI water.

Silicon-Based Devices Fabrication Process

Figure 2: Schematic representation of the steps in the microfabrication process for devices with integrated electrodes on a silicon supporting structure (diagrams are not to scale).

Photolithography. Every photolithography step mentioned in the fabrication process uses the AZ15NXT negative resist and lead to a resist thickness of 9 µm. A hexamethyldisilazane (HMDS) deposit is performed on the wafer to ensure the adhesion of the resist on oxidized surfaces. The wafer is coated with a spinning machine (speed: 2000 rpm/min, acceleration: 4000 rpm/min^2, time: 30 seconds). The annealing is done at 110°C for 2 minutes. UV exposure is performed with a dose of 300 mJ/cm^2 in vacuum contact. Post-exposure curing is performed at 120°C for 1 min and the resist is developed in MFCD26 for 15 minutes. Following the pattern transfer step, the resist is stripped from the wafer in NF52 developer heated at 80°C for 5 minutes followed by an O_2 plasma (time: 5 min, power: 400 W, O2 flow rate: 1000 mL/min) to remove potential resist leftovers.

1. **Substrate cleaning**. A 4-inch silicon wafer is first cleaned in a piranha solution (50% $H2_SO_4$ + 50% H_2O_2). Deoxidation is then performed in a 5% HF solution.

2. **Chemical vapor deposition**. Thermal oxidation is performed at 1070 °C on the substrate to obtain an 800 nm SiO_2 layer. A 600 nm SiN_x film is then deposited at 750°C by LPCVD. These deposits are made on both sides of the wafer at the same time.

3. **Physical Vapor Deposition followed by Electroplating of contact pads (L1)**. A seed layer consisting of a bilayer of Chromium and Gold of respectively 50 nm and 100 nm is deposited by thermal evaporation on the wafer. The previously described photolithography step is performed, followed by the electrolytic growth of 1 µm of gold and the removal of the resist.

4. **RIE Plasma etching of seed layer for electrode definition (L2)**. As previously described, the wafer is spin coated with an AZ15NXT negative resist, exposed to UV and developed. The Cr/Au seed layer of 150 nm is then etched with argon plasma (Ar, 30 cm^3/min) at a sample temperature of 20°C for 3 minutes with a RF power of 100 W and an ICP power of 600 W with a reactor residual pressure of 0,67 mT. This etching step induces gold sputtering over the resist. The resist stripping is therefore done within a NF52 solution for 5 minutes with the wafer placed upside down in an ultrasonic bath followed by the O_2 plasma cleaning step.

5. **CVD Deposition and RIE Plasma etching of Si_3N_4 (L3)**. A 1 µm layer of Si_3N_4 is deposited through a PECVD technique on the wafer at 300°C in 10 minutes. The deposition is followed by the photolithography process. Finally, etching of the deposited Si_3N_4 layer is done through RIE plasma etching, using trifluoromethane (CHF_3, 20 cm^3/min), nitrogen (N_2, 10 cm^3/min), argon (Ar, 100 cm^3/min) and dioxygen (O_2, 10 cm^3/min). The process step takes 8 min for etching the 1 µm layer at a temperature of 20°C and with a RF power of 35 W and ICP power of 300 W with a reactor residual pressure of 25 mT.

6. **Opening the pores of the filtering membrane (L4)**. Following the photolithography step, RIE etching of the bilayer membrane (SiO_2/SiN_x) is performed using trifluoromethane (CHF_3, 20 cm^3/min) and argon (Ar, 50 cm^3/min) to etch 0.6 µm silicon nitride and 0.8 µm silicon dioxide successively. The plasma etching takes 10 minutes at a sample temperature of 15°C and with a RF power of 90 W to generate the plasma and an ICP power of 300 W with a reactor residual pressure of 7,1 mT.

7. **Etching of the silicon substrate and release of the devices (L5)**. The etching of the silicon substrate is done in two steps. The first step consists of the wafer thinning through plasma etching using an isotropic etching recipe, trimming the wafer from 550 µm to 250 µm (SF_6 at 700 cm^3/min, 20°C, RF Power: 2800W, BIAS Power: 85W, time: 37.5 minutes). This step is followed by a light O_2 plasma to remove the SF_6 hydrophobic layer before the photolithography step which is performed on the backside of the wafer with a pattern alignment on the front side. A thermal paste is used to bind the

wafer to be etched to a second silicon wafer on which the etching will stop, thus avoiding damaging the equipment's chuck while keeping a good thermalization of the exposed resist. The silicon etching process then follows a trip-pulsated Bosch etching process for 40 minutes. A light O_2 plasma allows to remove the SF_6 hydrophobic layer and is followed by both the resist and thermal paste removal within a piranha solution (50% H_2SO_4 + 50% H_2O_2) heated at 120°C for 15 minutes. The devices are then rinsed with DI water and stored.

Gas	Flow rate	Time	RF Plasma	LF Polarization
SF_6	700 sccm	3s	2300W	85W
C_4F_8	350 sccm	3.5s		
O_2	200 sccm	2s		

Table 1: Plasma parameters for Bosch etching process.

Glass-Based Devices Fabrication Process

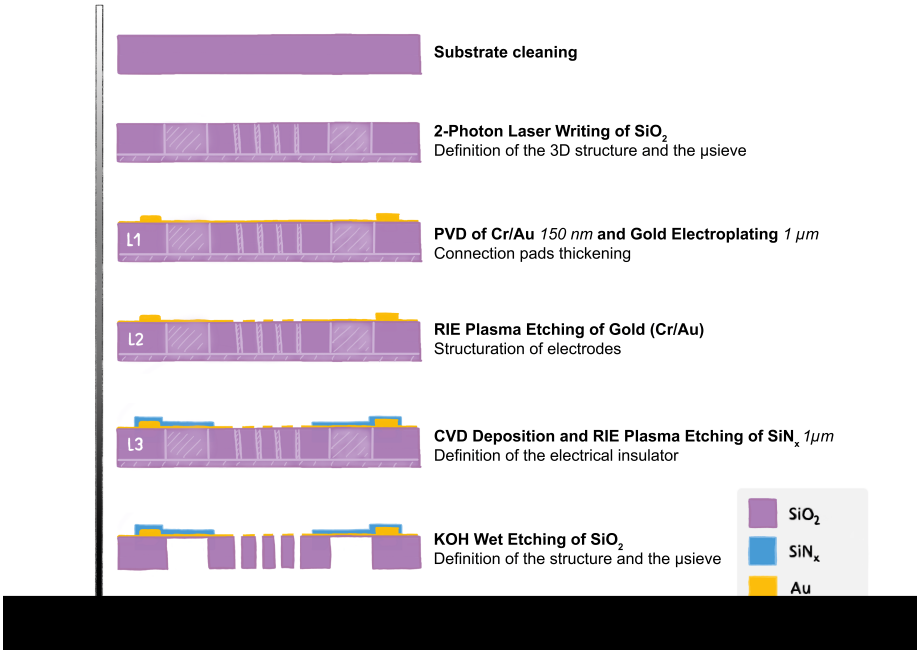

Figure 3: Schematic representation of the technological steps of the microfabrication process for devices with integrated electrodes on a glass supporting structure. Diagrams are not to scale.

Photolithography. Every photolithography step mentioned in the fabrication process uses the AZ15NXT negative resist and lead to a resist thickness of 9 µm. A hexamethyldisilazane (HMDS) deposit is performed on the wafer to ensure the adhesion of the resist on oxidized surfaces. The wafer is coated with a spinning machine (speed: 2000 rpm/min, acceleration: 4000 rpm/min^2, time: 30 seconds). The annealing is done at 110°C for 2 minutes. UV exposure is performed with a dose of 300 mJ/cm^2 in vacuum contact. Post-exposure curing is performed at 120°C for 1 min and the resist is developed in MFCD26 for 15 minutes. Following the pattern transfer step, the resist is stripped from the wafer in NF52 developer heated at 80°C for 5 minutes followed by an O_2 plasma (time: 5 min, power: 400 W, O2 flow rate: 1000 mL/min) to remove potential resist leftovers.

1. **Substrate cleaning**. A 5cm-by-5cm SiO_2 substrate is cleaned in a piranha solution (50% H_2SO_4 + 50% H_2O_2).

2. **2-Photon Laser Writing of SiO_2.** The substrate is exposed, layer by layer, to laser radiation using a Femtika machine, following a given 3D CAD design. The writing takes 2 hours, the substrate is then cleaned using DI water in an ultrasonic bath.

3. **Physical Vapor Deposition followed by Electroplating of contact pads (L1).** A seed layer consisting of a bilayer of Chromium and Gold of respectively 50 nm and 100 nm is deposited by thermal evaporation on the wafer. The previously described photolithography step is performed, followed by the electrolytic growth of 1 µm of gold and the removal of the resist.

4. **RIE Plasma etching of seed layer for electrode definition (L2).** As previously described, the wafer is spin coated with an AZ15NXT negative resist, exposed to UV and developed. The Cr/Au seed layer of 150 nm is then etched with argon plasma (Ar, 30 cm^3/min) at a sample temperature of 20°C for 3 minutes with a RF power of 100 W and an ICP power of 600 W with a reactor residual pressure of 0,67 mT. This etching step induces gold sputtering over the resist. The resist stripping is therefore done within a NF52 solution for 5 minutes with the wafer placed upside down in an ultrasonic bath followed by the O_2 plasma cleaning step.

5. **CVD Deposition and RIE Plasma etching of Si_3N_4 (L3).** A 1 µm layer of Si_3N_4 is deposited through a PECVD technique on the wafer at 300°C in 10 minutes. The deposition is followed by the photolithography process. Finally, etching of the deposited Si_3N_4 layer is done through RIE plasma etching, using trifluoromethane (CHF_3, 20 cm^3/min), nitrogen (N_2, 10 cm^3/min), argon (Ar, 100 cm^3/min) and dioxygen (O_2, 10 cm^3/min). The process step takes 8 min for etching the 1µm layer at a temperature of 20°C and with a RF power of 35 W and ICP power of 300 W with a reactor residual pressure of 25 mT.

6. **KOH wet etching of SiO_2.** The SiO_2 substrate is etched in a KOH solution heated at 80°C for 3 hours. Due to the laser writing, laser written parts of the substrate a preferentially etched, thus defining the structure and the filtering membrane while releasing the devices from the substrate. The devices a then rinsed successively in an acetic acid solution and in DI water for 5 minutes.

Silanization Process

Solutions

- MAPTMS, 3-methacryloxypropyltrimethoxysilane (Sigma-Aldrich)
- Acetone, Ethanol, DI Water
- Glacial Acetic Acid (Sigma-Aldrich)

Preparation

- Wash successively both sides of the glass slides with acetone, ethanol and water. Dry with nitrogen.
- Activation of the glass surface with an O2 plasma treatment: 5 minutes (Diener, 50W, 100%, 15 sccm)

2% MAPTMS solution for 20mL

- 19,6 mL of ethanol
- 2µL of acetic acid
- 400µL of MAPTMS

Silanization

- Cover the glass coverslip with the MAPTMS solution.
- Incubate for 1h.
- Wash glass coverslips with ethanol and dry with nitrogen.

These glass coverslips can then be stored and be integrated in 3D printed designs.

Scientific Production

.1 Publications

- Sagot, M.; Bou, E.; Bourrier, D.; Cerf, A.; Aubert, H.; Vieu, C. Bio-Impedance Spectroscopy of Retained Cells Using a Micro-Perforated Sensing Membrane Filtrating Whole Blood Samples under High Flowrate. Biosensors 2023, 13, 996.
- Sagot, M.; Derkenne, T.; Giunchi, P.; Nougayrède J.; Tregouet, C.; Raimbault, V.; Malaquin, L.; Venzac, B. Functionalities integration in stereolithography 3D printed microfluidics using a "print-pause-print" strategy. Submitted to Lab on a Chip on 14/02/2024.

.2 Conferences

- Micro and Nano Engineering (MNE), Leuven, Belgium (19-23 September 2022): Sagot, M.; Bou, E.; Bourrier, D.; Cerf, A.; Aubert, H.; Vieu, C. Micro-perforated membrane for label-free cell capture and integrated electrical detection operating in whole blood.
- Micro and Nano Engineering (MNE), Berlin, Germay (25-28 September 2023): Sagot, M.; Venzac, B.; Bourrier, D.; Lecestre, A.; Laborde, A.; Cerf, A.; Aubert, H.; Vieu, C. 3D Integration of a micro-perforated membrane for combined in-situ electrical analysis and real time imaging of living cells.
- Cancéropôle Grand Sud-Ouest (GSO), Workshop "Precision Nanomedicine", Bordeaux, France (4-5 Mars 2024): Sagot, M.; Venzac, B.; Bourrier, D.; Lecestre, A.; Laborde, A.; Cerf, A.; Aubert, H.; Vieu, C. Microtechnologies for liquid biopsy applications: 3D Integration of a sensing micro-perforated membrane for cell capture and multimodal in-situ cell analysis in whole blood.